Title
State-selective Modulation of Heterotrimeric Gαs Signaling with Macrocyclic Peptides

Author
Dai, Shizhong

Publication Date
2022

Peer reviewed|Thesis/dissertation

State-selective Modulation of Heterotrimeric Gαs Signaling with Macrocyclic Peptides

by
Shizhong Dai

DISSERTATION
Submitted in partial satisfaction of the requirements for degree of
DOCTOR OF PHILOSOPHY

in

Chemistry and Chemical Biology

in the

GRADUATE DIVISION
of the
UNIVERSITY OF CALIFORNIA, SAN FRANCISCO

Approved:

DocuSigned by:
Kevan Shokat
8FDF47C586EF40D...

Kevan Shokat
Chair

DocuSigned by:
Jason Gestwicki
DocuSigned by:
Davide Ruggero
14C3B6AD60C5446...

Jason Gestwicki

Davide Ruggero

Committee Members

Dedication

This work is dedicated to my parents and my fiancé, who have given me their unconditional love.

Acknowledgements

My journey in graduate school has been fantastic, I would not have been able to finish this dissertation without the support of my mentors, colleagues, family, and friends. I would like to thank my advisor, Kevan Shokat for your inspiration and unconditional support over the years. You have taught me how to become a resilient scientist who is willing to asking the boldest questions. I am very appreciative of the scientific help and constant advice I received from my thesis committee members, Jason Gestwicki and Davide Ruggero. Thank you also to other mentors that I had the privilege to work with at UCSF, especially Mark von Zastrow, Roshanak Irannejad, and Aashish Manglik.

I would also like to thank all my colleagues and friends in the Shokat lab for helping me move my projects forward and making me laugh all the time. A special thank you to all of my collaborators at UCSF and other institutes, I had a great time doing cool science with you. Thank you also to my CCB cohort who are a group of rising scientists growing along with me at UCSF.

I am grateful to have a group of great friends from high school, college, and grad school. Thank you for being there whenever I needed you. Finally, I would like to thank my family and my fiancé for your love. Thank you for always accepting me for who I am and for always supporting my dreams.

Contributions

Several chapters of this thesis contain material from previously published work. They do not represent the final published forms and have been edited slightly.

Chapter 2 of this dissertation is a reprint of a previous publication:

> **Dai, S. A.**, Q. Hu, R. Gao, H. Peacock, E. E. Blythe, Z. Zhang, M. von Zastrow, H. Suga, and K. M. Shokat. "State-selective Modulation of Heterotrimeric Gαs Signaling with Macrocyclic Peptides." *bioRxiv* (2020). doi: 10.1101/2020.04.25.054080.
>
> K.M.S., and H.S. conceived the project; S.A.D., Q.H., R.G., K.M.S., and H.S. designed the experiments. R.G. and H. P. performed cyclic peptide selection using the RaPID system; S.A.D., R.G., H. P. and Z.Z. carried out the chemical synthesis of cyclic peptides; S.A.D., and Q.H. performed biochemical characterization of the cyclic peptides, including protein purification, the adenylyl cyclase activation assay, the FRET assay, the BLI assay; Q.H. crystallized the GN13/Gαs and GD20/Gαs complexes and determined the structures; S.A.D. and E.E.B performed the cell-based assays; S.A.D., and K.M.S wrote the manuscript with the contribution from other authors.

“The journey itself is the reward”

State-selective Modulation of Heterotrimeric Gαs Signaling with Macrocyclic Peptides

by

Shizhong Dai

Abstract

The G protein-coupled receptor (GPCR) cascade leading to production of the second messenger cAMP is replete with pharmacologically targetable receptors and enzymes with the exception of the stimulatory G protein α subunit, Gαs. GTPases remain largely undruggable given the difficulty of displacing high affinity guanine nucleotides and the lack of other drug binding sites. We explored a chemical library of 10^{12} cyclic peptides in order to expand the chemical search for inhibitors of this enzyme class. We identified two macrocyclic peptides, GN13 and GD20, that antagonize the active and inactive state of Gαs, respectively. Both GN13 and GD20 showed high G protein specificity and nucleotide-binding-state selectivity. Co-crystal structures reveal that GN13 and GD20 distinguish the conformation difference within the switch II / α3 pocket in Gαs and directly block effector interactions. GN13 and GD20 modulate Gαs function, including Gαs steady state GTPase activity, Gαs-mediated adenylyl cyclase activation, and Gαs-Gβγ interaction, through binding to the crystallographically defined pocket. Intriguingly, the active state inhibitor GN13 potently inhibit constitutively activated oncogenic mutants of Gαs (Q227L, R201C, R201H, and R201S), which suggests a promising therapeutic approach for Gαs-driven cancer. The discovery of conformation-selective cyclic peptide inhibitors targeting Gαs provides path for the development of state-dependent GTPase inhibitors.

Table of Contents

List of Figures

List of Tables

Chapter 1

Introduction: Targeting the Ras-like superfamily GTPases in human disease

Abstract

The evolutionarily conserved Ras-like GTPases are molecular switch proteins regulating nearly all fundamental cellular processes. Based on the sequence and functional similarities and differences, Ras-like GTPases can be classified into Ras, Rho, Rab, Arf, Ran, and heterotrimeric Gα families. They shuttle between the active and inactive states by binding to two guanine nucleotides, GTP and GDP, respectively. The intrinsic and GAP-mediated GTP hydrolysis and GEF-catalyzed GTP-GDP exchange orchestrate precise GTPase activation in normal cells. Dysregulated Ras-like GTPases are strongly associated with human diseases, however, GTPases still represent one of the few remaining large families of signaling enzymes which are largely "undruggable" despite great efforts. In chapter 1, I will summarize the molecular basis of GTPases regulation, and their clinical relevance in human diseases. I will discuss the current drug discovery effort on inhibiting these challenging targets.

Introduction

GTPases are a family of nucleotide binding enzymes that preferentially bind to the guanine nucleotides. They serve as molecular switches in many fundamental cellular processes by binding to two major guanine nucleotides, including the nucleotide guanosine triphosphate, GTP, and guanosine diphosphate, GDP. The GTP-bound state of GTPases is normally considered as the active state, which transduces downstream signaling by regulating the activity of effector proteins. In normal cell signaling, the short-lived ON state of GTPases is switched off by intrinsic or enzyme-regulated hydrolysis of GTP, leading to deactivation of the active state GTPases.

Structurally, GTPases are classic P-loop nucleotide binding proteins that are composed by a β-sheet core and surrounding α-helices (Leipe et al., 2002). GTPases have a few sequence-

conserved motifs to engage the guanine nucleotides. The P-loop (also known as the Walker A motif) uses a conserved lysine residue to capture the phosphate groups of bound nucleotides. The Walker B motif contains a conserved acidic residue for binding Mg^{2+}. In comparison with other nucleotide binding proteins, GTPases have a unique [NT]KxD motif(Bourne et al., 1991), which supports the specificity for guanine nucleotides (Figure 1.1). GTPases can be divided into two major classes based on the topology of the β-sheet(Leipe et al., 2002). The TRAFAC (for translation factor-related) class GTPases have a pair of antiparallel β strands near the Walker B motif. This class of GTPases contains most of the well-known GTPases, including translation factors, Ras-like GTPases and others. By contrast, the SIMIBI (signal recognition particle, MinD and BioD related) class GTPases have a uniformly parallel β sheet. The SIMIBI class GTPases are regulatory proteins that are involved in protein localization, chromosome partitioning, and membrane transport.

Most of the eukaryotic TRAFAC class GTPases can be further divided into three GTPase superfamilies based on their sequence and functional similarity and differences: the Ras-like superfamily that is responsible for signal transduction; the translation factor superfamily that is important in translational regulation; the myosin-kinesin superfamily that is a family of motor proteins which has shifted to ATP-binding. In **chapter 1**, I will summarize the function of Ras-like GTPase superfamily members in human diseases and explore the structurally characterized Ras-like superfamily GTPases targeting molecules.

Dysregulated Ras-like superfamily GTPases in human diseases

The Ras-like superfamily of GTPases comprises more than 170 human members (Colicelli, 2004). This family was named after its prototypical member Ras, from "Rat sarcoma virus". All

of the Ras-like superfamily contain a structurally conserved GTPase domain with a molecular weight of ~20 kDa. They can be subclassified into small GTPases that function as monomers (including five different families: Ras, Rho, Rab, Arf, and Ran) (Wennerberg et al., 2005), and heterotrimeric Gα GTPases that transduce signaling with obligate Gβγ.

The Ras-like superfamily GTPases bind to GDP and GTP with high affinity. The GTP-GDP exchange orchestrated Ras-like GTPases activation. As a result, nucleotide exchange is fine-tuned by GTPases regulatory proteins and GTPase enzymatic activities (Figure 1.2). The rate-limiting step of Ras-like GTPase activation is GDP dissociation (Neal et al., 1988). In most of the GTPase activation cycles, GDP release from the nucleotide binding pocket is catalyzed by Guanine nucleotide Exchange Factors (GEFs) (Quilliam et al., 2002). GTPases are then activated by spontaneous GTP loading because of a high cellular GTP concentration ([GTP]/[GDP] ≈ 10). The transient activation of GTP-bound active GTPases are switched off by GTP hydrolysis. However, the intrinsic GTPase activity of Ras-like GTPases is relatively low. GTP hydrolysis is typically accelerated by numerous GTPase activating proteins (GAPs) (McCormick, 1998).

The precise regulation of Ras-like superfamily GTPases controls normal cell signaling transductions. Consequently, dysregulated Ras-like superfamily GTPases are often found to be crucial disease-causing factors.

Ras family GTPases in disease

The Ras family of GTPases is composed of over 36 structurally similar members. They are critical molecular switches that control cell proliferation, differentiation, survival, apoptosis, gene expression, cell–cell contacts, and many other signaling pathways. The roles of Ras family GTPases have been widely studied in human disease. The best characterized members of this

family are the human oncoproteins, K-Ras, H-Ras, and N-Ras. Mutationally activated K-Ras, H-Ras, and N-Ras proteins were discovered from cancer-causing viruses (Harvey, 1957; Malumbres and Barbacid, 2002)and their transforming activities were well-validated in *in-vitro* and *in vivo* models (Alan Hall, 1983; Geoffrey M. Cooper, 1982; Luis F. Parada, 1982; Marshall et al., 1982; Santos et al., 1982; Shimizu et al., 1983; Taparowsky et al., 1982). Oncogenic mutations in these three Ras family GTPases are highly frequency (>20% of all tumors). These activating mutations either disable GTPase function and GAP sensitivity (K-Ras^{G12D}, Hunter et al., 2015) or increase guanine nucleotide exchange (H-Ras^{N116H}, Patel et al., 1992), rendering the GTPase domains adopt a constitutively activated GTP-bound state. The activated Ras proteins then stimulate the ERK mitogen-activated protein kinase (MAPK) cascade, leading to tumorigenesis.

Some other Ras family GTPases mutants were also reported to be involved in cancer and other diseases, although with a much lower frequency compared to K-Ras, H-Ras, and N-Ras. RRAS proteins (R-Ras, R-Ras2, and M-Ras) regulate mitogenesis and the cytoskeleton, and they can transform cultured fibroblast cells (Cox et al., 1994; Ehrhardt et al.,1999; Graham et al., 1994). Cancer genomic sequencing indicates that R-Ras and R-Ras2 are both driver oncogenes and are altered in approximately 1% of cancer patients. In particular, R-Ras is mutated or amplificated in 5% lung cancer patients, and most of hotspot mutations cluster at codon Q87. R-Ras2 is mutated in 4% endometrial cancer patients with activating mutations residing at both codons G23 and Q72. Ral proteins (RalA and RalB) and Rap proteins are frequently amplified in lung cancer (~20%). Ral and Rap proteins are not oncogenic in *in vitro* models, however, overexpressed Ral and Rap proteins might enhance or interfere the oncogenic transformation downstream of Ras and EGFR (Kitayama et al., 1989; Urano et al., 1996). REM proteins (Gem, Rem1, and Rem2) are frequently amplified in lung, esophagogastric, hepatobiliary, and uterine cancer patients (15-20%) with the

exception of RRad. A rare non-synonymous R211H mutation in RRad causes a familial case of Brugada syndrome (BrS), an inherited cardiac disorder predisposing to ventricular arrhythmias (Belbachir et al., 2019). Rheb protein is a key regulator in the mTOR signaling pathway and cell cycle control. Because of the low intrinsic GTPase activity, Rheb protein is normally in the GTP-bound active state (Mazhab-Jafari et al., 2012). The Rheb protein activity is tuned down by the tumor suppressor TSC1-TSC2 complex. Rheb is frequently overexpressed in cancer and it is critical and sufficient for skin epithelial tumorigenesis (Lu et al., 2010). Rit proteins (Rit1 and Rit2 (also called Rin)) positive regulates cell survival. Somatic mutations in RIT1 are discovered in ~2% of lung adenocarcinoma cases and they cluster in a hotspot near the switch II domain of the protein (Berger et al., 2014). Mutation in Rit1 has known to be a casual factor of Noonan syndrome, a common autosomal dominant disorder clinically defined by a constellation of anomalies (Cavé et al., 2016).

Intriguingly, a number of the Ras family GTPases are putative tumor suppressors. DIRAS-1 (also known as Rig) is frequently down-regulated in primary human neural tumors. Overexpression of DIRAS-1 inhibited Ras-mediated cellular transformation and activation of downstream signaling in NIH 3T3 cells (Ellis et al., 2002). Rerg was also reported to be a potential tumor suppressor. Expression of Rerg protein in MCF-7 breast cancer cells significantly inhibited anchorage-dependent and anchorage-independent growth in *in vitro* models and inhibited tumor formation in nude mice (Finlin et al., 2001).

Rho family GTPases in disease

The Rho family of GTPases is composed of 23 structurally similar members. They function as key regulators in cytoskeletal remodeling, cell cycle progression and gene expression. A

distinctive insertion between the 5th β strand and the 4th α helix in the GTPase domain distinguish Rho family of GTPases from the other GTPases (Figure 1.3). The Rho family GTPases have also been strongly associated with cancer, although their genetic alterations are much less frequent than the Ras family GTPases.

The prototypical protein of the Rho family of GTPases is the transforming protein RhoA. RhoA is primarily associated with cytoskeleton regulation and its role in cancer has been widely recognized. RhoA is highly mutated in mature T and NK neoplasms (>40%). Most of the RhoA somatic mutations cluster at the codon G17, predominantly as a G17V mutation (78%). It is noteworthy that RhoA G17 is not the homologues residue of the Ras mutation hotspot G12. The RhoA G17 (homologues residue in Ras, G15) sits in the P-loop and directly interacts with the β,γ-phosphates of guanine nucleotides and coordinates the Mg^{2+} ion. A bulky G17V reduces GTP binding and results in a nucleotide-free state of RhoA. Biochemical and cellular experiments suggested that $RhoA^{G17V}$ serves as a dominant negative mutant and inhibits the function of WT RhoA. *In vivo* analyses in mouse models further supported that $RhoA^{G17V}$ is a cancer driver (Sakata-Yanagimoto et al., 2014; Schaefer and Der, 2022). A paralog of RhoA, RhoC also regulates cancer cell invasion and metastasis by protein overexpression (Thomas et al., 2019).

Ras-related C3 botulinum toxin substrate 1 (Rac1) is a founding member of the Rac subfamily. Rac1 has ubiquitous tissue expression and control cell motility by regulating the formation of lamellipodia (Parri and Chiarugi, 2010). Although RAC1 (the gene that encodes Rac1 protein) is a rare driver oncogene (somatic mutation frequency = 0.4%), a recurrent somatic missense mutation (P29S) was discovered in up to 9% of sun-exposed melanomas. This hotspot mutation at codon 29 maintains intrinsic Rac1 GTP hydrolysis but activates Rac1 by increasing Rac1 GDP/GTP nucleotide exchange (Davis et al., 2013). Unlike Rac1 that has ubiquitous

expression, its paralog Rac2 is only expressed in hematopoietic cells (Didsburys et al., 1989). A deactivating mutation, D57N locks Rac2 in the GDP-bound form, which lead to human neutrophil immunodeficiency syndrome (Ambruso et al., 2000).

Cell division control protein 42 homolog (Cdc42) belongs to the Cdc42-related protein subfamily. Cdc42 stimulates the formation of filopodia and regulate cell cycle and has been reported to be a putative oncoprotein. Cdc42 mutations have not been detected in human cancers, but it is overexpressed in multiple types of cancers including non-small cell lung cancer, colorectal adenocarcinoma, and breast cancer (Stengel and Zheng, 2011).

Rho family GTPases are also involved in other disease. Missense mutation of Rho-related BTB domain-containing protein 2 (RHOBTB2) causes a rare developmental and epileptic encephalopathy in human (Straub et al., 2018). The mitochondrial Rho GTPase (Miro) is the target of PINK1 and Parkin, phosphorylation degrades Miro protein level and arrests mitochondrial motility (Wang et al., 2011). In Drosophila models, downregulation of Miro rescued PINK1 mutant phenotypes in dopaminergic (DA) neurons, while Miro overexpression alone caused DA neuron loss (Liu et al., 2012).

Rab family GTPases in disease

The Rab family of GTPases is composed of over 60 members. Rab proteins are essential regulators in protein trafficking. Rab protein dysregulation has widely studied in neurodegeneration and immune deficiency. Although Rab proteins are rarely mutated in human cancer, emerging evidence has indicated that Rab proteins are also critical regulators in oncogenic signaling.

Sporadic Alzheimer's disease (AD) cases are often associated with upregulation of the endosomal Rab proteins, such as Rab4, Rab5, Rab7a, etc. These Rab proteins might influence the normal trafficking and signaling of neurotrophic factors (Guadagno and Progida, 2019). Rab7a protein is also dysregulated in other neurodegenerative disease. In Parkinson's disease (PD), Rab7a has been known to regulate endocytic membrane trafficking along with another PD-related GTPase LRRK2 (Gómez-Suaga et al., 2014). Activating mutations of Rab7a (L129F, K157N, N161I, and others) are strongly associated with the Charcot-Marie-Tooth (CMT) disease, the most common hereditary peripheral neuropathy (McCray et al., 2010).

Rab protein mutations are found in pathogenic infection and immune dysfunctions. The Rab5 endosomal signaling can be hijacked by *Mycobacterium tuberculosis* and *Legionella pneumophila*. These two bacterial species secrete effectors and regulators to interfere Rab5 phagosomal trafficking, which prevents pathogen clearance (Fratti et al., 2001; Sohn et al., 2015). Mutations of Rab proteins, including Rab27a, Rab18, and others, lead to rare recessive genetic disorders, including Griscelli syndrome, Choroideremia, or Warburg Micro syndrome (Bem et al., 2011; Ménasché et al., 2000; Seabra et al., 1995).

Rab35 has been implicated in cytokinesis and PI3K signaling. Two recently discovered somatic Rab35 mutations (A151T and F161L) found in human tumors constitutively activate the PI3K/AKT pathway in the absence of growth factors. Homologues mutations (A146T and F156L) in K-Ras have also been documented in cancer (Wheeler et al., 2015). Rab25 has been reported to act as a dual modulator in cancer: it positively regulates AKT signaling in ovarian cancer while suppressing cancer progression in colorectal cancer (Wang et al., 2017).

Arf and Ran family GTPases in disease

The ADP-ribosylation factor (Arf) family proteins are involved in regulating vesicle biogenesis in intracellular traffic. Although the Arf proteins are not oncogenic themselves, overexpression of one of the founding members, Arf1 has been implicated in regulating cell-cell adhesion in cancer cells (Schlienger et al., 2016). The Arf proteins are tightly regulated by their GEF and GAP proteins. Missense mutations in BRAG1, which encodes an Arf6 GEF, have been reported to cause nonsyndromic X-linked intellectual disability (Shoubridge et al., 2010). Mutations in another Arf subfamily GTPases, Sar1 (G37R and D137N) were predicted to influence Sar1 GTP binding. The Sar1 mutants interfere typical COPII vesicles formation and lead to Chylomicron retention disease (CMRD), which is a rare autosomal recessive disorder that affects fat absorption (Jones et al., 2003).

Ran protein is a unique Ras-like GTPase whose activation is spatially regulated by RanGAP and RanGEF. RanGEF (RCC1) binds to chromatin and therefore reside in the nucleus, whereas RanGAP is mostly cytoplasmic. Therefore, the active GTP-bound Ran protein is enriched in the nucleus. Ran is not an oncoprotein, and it is rarely mutated in cancer. However, Ran has been found to be overexpressed in multiple cancer types. High expression of Ran is also associated with local invasion and metastasis of renal cell carcinoma (Abe et al., 2008; Boudhraa et al., 2020).

Heterotrimeric Gα family GTPases in disease

The Gα family GTPases are distantly related Ras-like GTPases. They process a GTPase domain and a structurally conversed helical domain insertion after the α1 helix. In the GDP-bound inactive state, sixteen Gα proteins form tight heterotrimers with Gβγ. GPCR activation triggers Gα GTPases nucleotide exchange, which then activates both Gα and Gβγ to transduce downstream

signaling. Gα proteins are frequently altered in human diseases (O'Hayre et al., 2013). Deep sequencing studies showed that 4.2% of tumors carry activating mutations in *GNAS* (Gαs-encoding gene). Nearly ~70% of these mutations cluster around two hotspot residues, R201 (88.12%) and Q227 (10.60%). Loss-of-function mutation in Gαs, R228C, causes pseudohypoparathyroidism type 1a (PHP-Ia), an autosomal dominant disorder leads to thyroid stimulating hormone resistance (Tam et al., 2014). Activating mutations in *GNAQ* or *GNA11* (Gαq and Gα11 encoding genes) cause ~66% and ~6% of melanomas arising in the eye and skin, respectively. Interestingly, the majority of *GNAQ* or *GNA11* mutations cluster at codon Q209 (>94%). Mutations in other Gα genes have been found in cancers, although with a much lower frequency. A rare somatic mutation, R243H in Gαo accelerates the rate of Gαo nucleotide exchange and promotes oncogenic transformation (Garcia-Marcos et al., 2011).

Pharmacological targeting the Ras-like superfamily GTPases

The Ras-like GTPase family is the most frequently mutated gene family in cancers. They are also strongly associated with many other diseases, including neurodegenerative diseases, immunodeficiency, infection, and etc. Consequently, Ras-like GTPases have been considered one of the most attractive targets for drug discovery. However, the unique biochemical and structural characteristics of Ras-like GTPase present challenges for directly inhibiting these GTPases. Ras-like GTPases bind to guanine nucleotides with relatively high affinity and slow off-rate. Directly competing GTP or GDP from the nucleotide binding pocket with small molecules is unlikely to be a viable strategy for most of the GTPases. Moreover, the conserved GTPase domain of the Ras-like proteins is relatively small and compact. They engage protein-protein interaction (PPI) with

diverse effector proteins at the dynamic switch regions. These PPI pockets are usually too shallow for a traditional small molecule to bind.

The recent breakthroughs in covalent inhibitor drug discovery and the evolving drug screening strategies have provided investigators more opportunities to tackle the "undruggability" of Ras-like GTPases. Here, I will summarize the recent advances in Ras-like GTPase drug discovery.

Targeting K-Ras, H-Ras, and N-Ras proteins in the Ras family GTPases

Activating mutations of the Ras proteins (K-Ras, H-Ras, and N-Ras) occur frequently in human cancer and drive oncogenic transformation. Directly inhibiting the oncogenic Ras proteins represent a desirable strategy for treating Ras-drive cancer. Following the pioneering work done by Shokat and colleagues, there are a number of Ras binding molecules reported to inhibit Ras protein signaling. Based on their binding modes, these molecules can be classified into covalent inhibitors and non-covalent inhibitors.

The discovery of covalent K-Ras inhibitors was first achieved by Shokat and colleagues: using disulfide tethering, they first identified a novel allosteric binding pocket at the switch-II region, in the mutant K-Ras^{G12C} protein (Figure 1.5B) (Ostrem et al., 2013). Following a few rounds of compound optimization, the most potent molecule, compound 12 (Figure 1.6) covalently bound to the GDP-bound K-Ras^{G12C}, inhibiting SOS-catalyzed nucleotide exchange and blocked K-Ras^{G12C} RAF interaction. Based on the same pharmacophore, a number of companies are developing more potent covalent K-Ras^{G12C} inhibitors, one of which has been approved by FDA as the first Ras-targeting therapy (AMG510, also known as Sotorasib) for the treatment of K-Ras^{G12C} -driven non-small cell lung cancer (NSCLC) (Figure 1.5C and Figure 1.6) (Canon et al.,

2019). It is noteworthy that these K-Ras^{G12C} -targeting small molecules only bind to the GDP-bound inactive state of K-Ras. Although the majority of K-Ras^{G12C} is GTP-bound in the steady state (~75%), the moderate intrinsic GTPase activity of K-Ras^{G12C} generates the GDP-bound species, which is sensitive to covalent inhibition. The covalent targeting strategy has been applied to other oncogenic K-Ras mutants, including G12S and G12R. Using a similar K-Ras binding pharmacophore but with a β-lactone warhead, Shokat and colleagues has discovered the first covalent molecule, G12Si-5 that targets K-Ras^{G12S} mutant and suppresses its oncogenic signaling (Figure 1.5D and Figure 1.6) (Zhang et al., 2022).

A recent drug discovery campaign with an engineered cysteine (M72C) in K-Ras has led to the identification of a new small molecule binding pocket (switch-II groove) that is adjacent to the switch-II pocket (Gentile et al., 2017). Intriguingly, compound 2C07 covalently bound to both the GDP-bound and GTP-bound state of the Ras^{M72C} protein, highlighting new opportunities for directly targeting the active state Ras mutant proteins (Figure 1.5E and Figure 1.6).

Ras protein can also be targeted with non-covalent molecules. A pan-Ras inhibitor, compound 3144 was designed from a computational docking library by Stockwell and colleagues. Compound 3144 bound all three WT Ras isoforms and inhibited the growth of a Ras mutant (K-Ras^{G13D}) mouse cancer xenografts (Welsch et al., 2017). DCAI, a millimolar pan-Ras binder, weakly inhibited Ras and SOS interaction. DCAI-bound Ras structure revealed a unique pocket (the DCAI pocket) between α2 helix and the core β-sheet, which is distinct from the switch-II pocket (Figure 1.5F and Figure 1.6) (Maurer et al., 2012). This DCAI pocket was further explored by another pan-Ras inhibitor, BI-2852, which was identified from a fragment-based drug discovery campaign (Figure 1.5G and Figure 1.6) (Kessler et al., 2019). BI-2852 directly blocked GEF, GAP, and effector interactions with Ras protein and inhibited downstream Ras signaling in K-Ras^{G12C}-

driven NCI-H358 cells. These reversible pan-Ras molecules have provided generalizable strategies for targeting all the Ras isoforms and they are not limited to the GDP-bound inactive state. However, they suffer from poor mutant-specificity and toxicity issues.

Two recently discovered K-Ras^{G12D} targeting molecules provide new solutions for reversibly targeting Ras protein with mutant-selectivity. MRTX1133 reversibly bound to K-Ras^{G12D} with an estimated K_D of 0.2 pM (Figure 1.5H and Figure 1.6), and it inhibited K-Ras signaling in K-Ras^{G12D}-driven AGS cells. A MRTX1133-bound in K-Ras^{G12D} structure revealed that a [3.2.1]bicyclic diamino bridge the interaction between G60 and D12 in K-Ras (Figure 1.7A), providing more than 500-fold selectivity against K-Ras^{WT} (Wang et al., 2022). KD2 is another selective K-Ras^{G12D} targeting molecule (Figure 1.5I and Figure 1.6). Being a macrocyclic peptide, KD2 extensively explored the ligand space in the K-Ras^{G12D} switch II region and used a T10 residue and a water molecule to directly engage Q61 and D12 in K-Ras. Moreover, the co-crystal structure of KD2 bound to K-Ras^{G12D}/GppNHp showed that KD2 occupies both switch II and switch grove, which provides KD great nucleotide-binding state selectivity over the GDP-bound K-Ras^{G12D} (Figure 1.7B) (Zhang et al., 2020).

Targeting other Ras family GTPases

Besides the well-studied K-Ras, H-Ras, and H-Ras proteins, other members in the Ras family GTPases are also attractive therapeutic targets for human diseases. The RalA and RalB GTPases transduce upstream Ras signaling and drive tumor growth by regulating cell adhesion, membrane trafficking, and etc. A structure-based in silico library screening and cell-based secondary screening identified a few lead compounds (RBC8, BQU57, and others, Figure 1.8) for Ral inhibition. The Ral residues showing significant chemical shift changes upon BQU57 binding

were mapped in the switch II region (Figure 1.8A-C). RBC8 and BQU57 showed selectivity for Ral relative to the GTPases Ras and RhoA and inhibited Ral-dependent tumor xenograft growth (Yan et al., 2014). Later, an aryl-sulfonyl-fluoride-containing covalent molecule, compound 1 was reported to irreversibly target the Y82 residue of Ral protein at a pocket that is close to the DCAI pocket. Compound 1 inhibited GEF Rgl2-mediated nucleotide exchange of Ral GTPase, with an IC_{50} value of 49.5 ± 2.3 μM (Bum-Erdene et al.).

The mTORC1 activating GTPase Rheb is highly expressed in some human lymphomas, and it can produce rapid development of aggressive and drug-resistant lymphomas. Saiah and colleagues discovered a series of Rheb inhibitors from fragment-based drug screening using NMR (Mahoney et al., 2018). Extensive medicinal chemistry efforts led to the identification of a potent molecule NR1 (Figure 1.9A), with an IC_{50} of 2.1 μM in the Rheb-dependent *in vitro* mTOR kinase assay. Structurally characterization revealed that NR1 bound Rheb between the switch I and switch II motifs. This binding pocket is unique compared to the above-mentioned drug binding GTPase pockets, highlighting a potential new opportunity for GTPase drug discovery (Figure 1.9B-D). Interestingly, NR1 selectively inhibits mTORC1 in cells. Structural analysis has indicted that some of the NR1 binding residues on Rheb protein surface are also responsible for Rheb-dependent mTORC1 activation. Therefore, NR1 mediated Rheb-mTOR1 inhibition might come from the direct competition with the mTOC1 complex proteins.

Targeting the Rho family GTPases

RhoA is the founding member of the Rho family GTPase, and its role in cancer cells metastasis has been widely appreciated. Using a molecular dynamics simulation of the RhoA protein, Cheng and colleagues discovered a targetable cysteine residue Cys107 that was later

targeted by a covalent molecule, DC-Rhoin (Figure 1.10A) (Sun et al., 2020). DC-Rhoin inhibited RhoA/GEF interaction and diminished GDP/GTP exchange rate of RhoA, with an IC_{50} value of 2.94 ± 0.34 μM. A DC-Rhoin-bound $RhoA^{Cyslight}$ has indicated the DC-Rhoin binding site (CLocK) (Figure 1.10D). This interaction is further confirmed by the C107A mutant in the labeling and rescue experiments. However, it is worth noting that the apo $RhoA^{Cyslight}$ induced a drastic conformation rearrangement comparted to $RhoA^{WT}$ (Figure 1.10B and 1.10C). The mechanism of action of DC-Rhoin requires further investigation.

A structure-based virtual screening has led to the identification of a micromolar Rac1 targeting molecule, NSC23766, which specifically inhibits Rac1 activation by blocking the Rac-specific GEFs Trio or Tiam1 (Gao et al., 2004). Intriguingly, NSC23766 showed no inhibition on other Rho family proteins, including RhoA and Cdc42. Although a NSC23766-bound Rac1 structure is not available, computational docking suggested that NSC23766 might bind Rac1 at the Trp58-containing GEF interface between the switch I and switch II motifs. Selective Cdc42 targeting small molecules (CASIN and ML141) were reported to inhibit Cdc42 nucleotide change (Florian et al., 2012; Hong et al., 2013). Both molecules are micromolar Cdc42 inhibitors, and they exhibited good selectivity over other Rho family proteins, including RhoA and Rac1. Mutation studies along with computational docking suggested that CASIN bind to the GEF binding interface between α5 and β2.

All of the existing Rho GTPase targeting small molecules do not exhibit mutant selectivity, hampering their potential usages as cancer therapeutics.

Targeting the Rab family GTPases

Rab family GTPases represent the largest branch of the Ras-like superfamily, however, there is scarce drug-like molecules that bind to Rab proteins. The only a few examples include CID 1067700 that inhibited Rab7a GTP loading (Agola et al., 2012), and CID 7721337 and CID 1508555 that increased Rab7 GTP loading (Palsuledesai et al., 2018b). However, these lead molecules had poor GTPase-selectivity and their mechanism of actins remain to be determined.

Targeting the Arf and Ran family GTPases

Pharmacological interrogation of the Ras-like superfamily GTPases are mostly limited to targeting the monomeric GTPase domains. One natural inhibitor brefeldin A (BFA) has been reported to directly inhibit ADP-ribosylation factor 1 (ARF1) with help from BFA-sensitive ARF GEFs that contain the Sec7 domain. BFA forms a stable complex with ARF1/GDP and the Sec7 domain in ARF GEF, and inhibited Golgi-associated guanine nucleotide exchange of ARF1. As a BFA-bound complex structure clearly illustrated, BFA sits in a cavity between ARF1 and $ARNO^{E156K}$ ($ARNO^{WT}$ is a BFA-resistant ARF GEF, however, an E156K mutation sensitized ARNO to BFA inhibition), stabilizing this special guanine nucleotide exchange reaction intermediate (Figure 1.12A-C) (Renault et al., 2003). This unique drug mechanism of action has inspired the search of other small molecule based ARF dual inhibitors. LM11 (Figure 1.12D) was discovered using *in silico* screening of a flexible pocket near the Arf1/GEF interface (Viaud et al., 2007). LM11 targets both Arf1-GDP and the Arf1/GDP ARNO complex and inhibited Arf1-dependent trafficking structures at the Golgi. NMR spectroscopy and mutagenesis studies suggested that LM11 exhibited similar mechanism of inhibition as BFA. Remarkably, LM11

inhibited the BFA-resistant ARF GEF, ARNO, indicating the turnability of the strategy. Both LM11 and BFA have class selectivity over a homologues Arf6.

Targeting the heterotrimeric Gα family GTPases

The heterotrimeric Gα family GTPases are largely undruggable with the exception of the Gαq/11, whose activation is potently inhibited by a bacterial natural product, YM-254890. YM-254890 is a macrocyclic depsipeptide that specifically inhibits the GDP/GTP exchange reaction of Gαq/11 by inhibiting GDP dissociation. YM-254890 inhibition also interferes intercellular calcium ion mobilization and serum response element-mediated transcription downstream of Gαq-coupled receptors. YM-254890 and its analog, FR900359 specificity recognize the GDP-bound inactive conformation of Gαq/11. However, they have been shown to direct target the activating mutant forms of Gαq and Gα11 in uveal melanoma (UM) by leveraging the low intrinsic GTPase activity of the Gαq/11 oncogenic mutants (Lapadula et al., 2019). Structurally characterization and extensive mutagenesis studies have elucidated the unique mechanism of action for YM-254890. YM-254890 binds the hydrophobic cleft between Gαq GTPase and helical domains, stabilizing the Gβγ binding GDP-bound conformation (Figure 1.13) (Nishimura et al.).

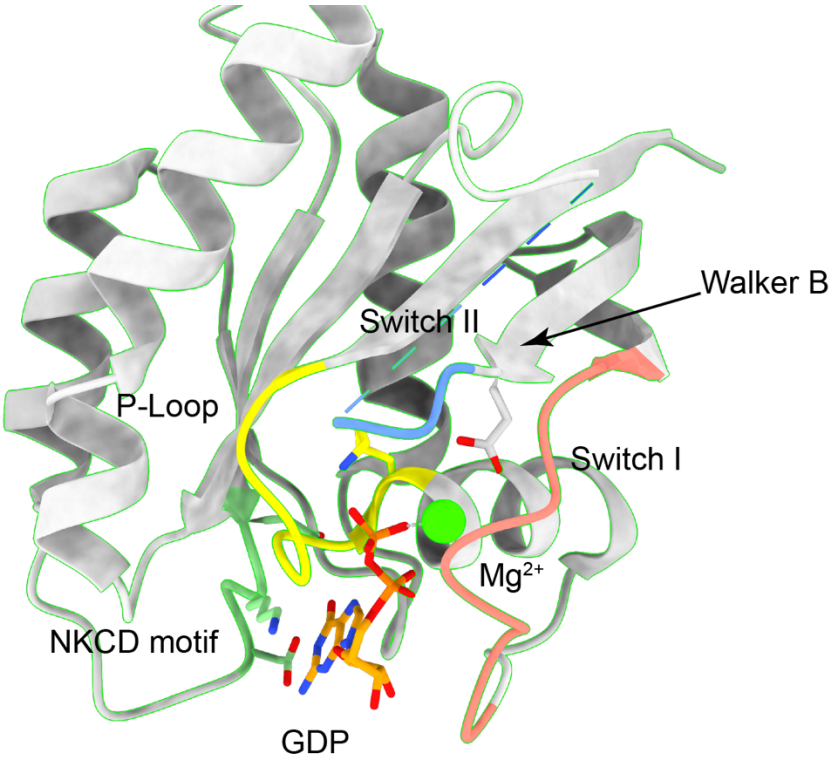

Figure 1.1 | Structure of WT GDP-bound K-Ras. Crystal structure of wild-type (WT) K-Ras with GDP-bound (PDB ID: 4LPK). P-loop, yellow; switch-I, salmon; switch-II, blue; NKCD motif, green; GDP is shown as stick models.

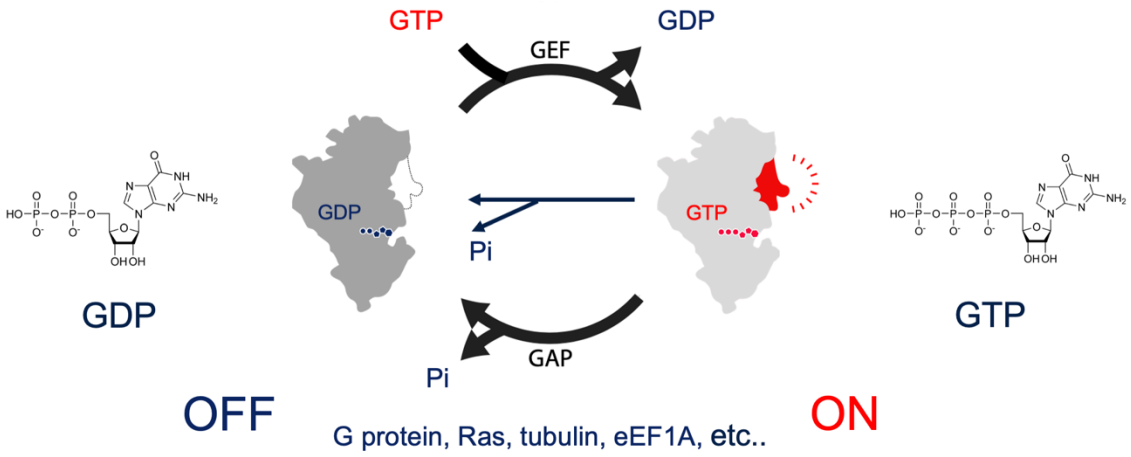

Figure 1.2 | Illustration of the GTPase activation cycle. GTPase activity is regulated by intrinsic or GAP-mediated GTP hydrolysis and GEF catalyzed GTP-GDP exchange.

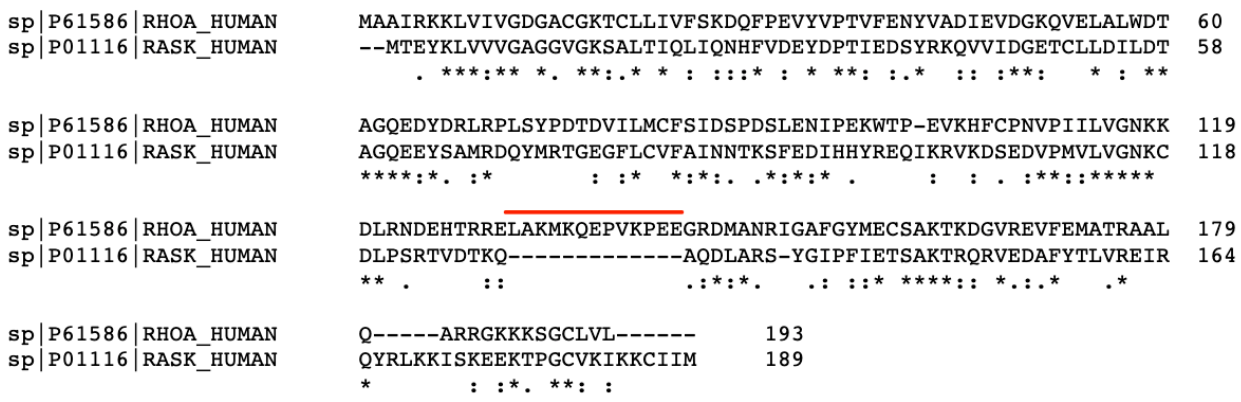

Figure 1.3 | Sequence alignment between K-Ras and RhoA. A distinctive insertion (red) between the 5th β strand and the 4th α helix in the GTPase domain distinguish Rho family of GTPases from the other GTPases.

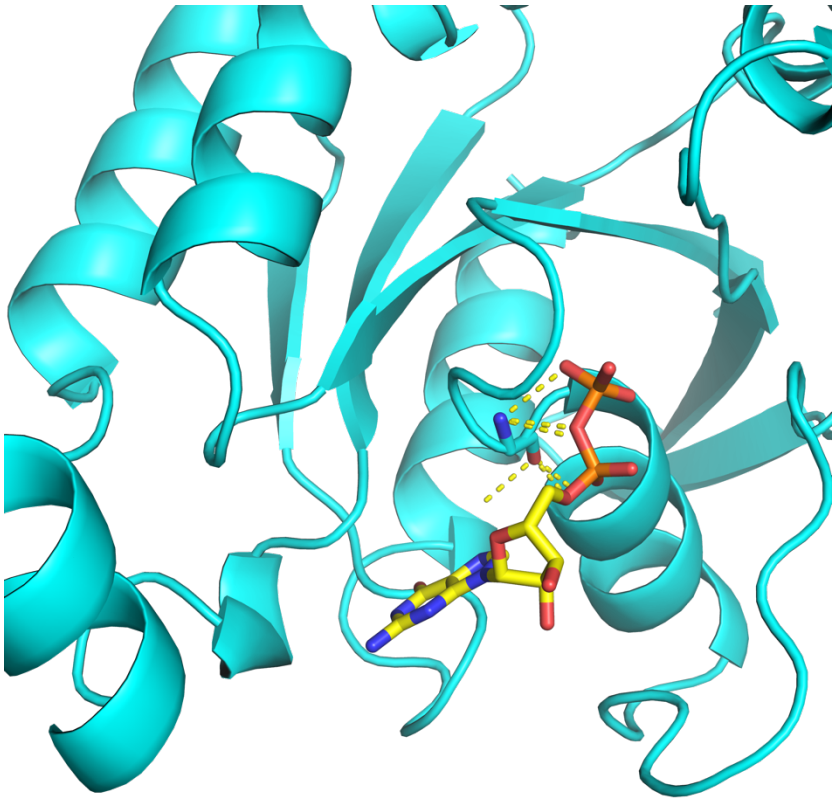

Figure 1.4 | The location of the mutation hotspot G17 in RhoA. Crystal structure of wild-type (WT) RhoA with GDP-bound (PDB ID: 1FTN). The hotspot G17 is shown as sticks. Hydrogen interactions between G17 and GDP are shown as yellow dashes.

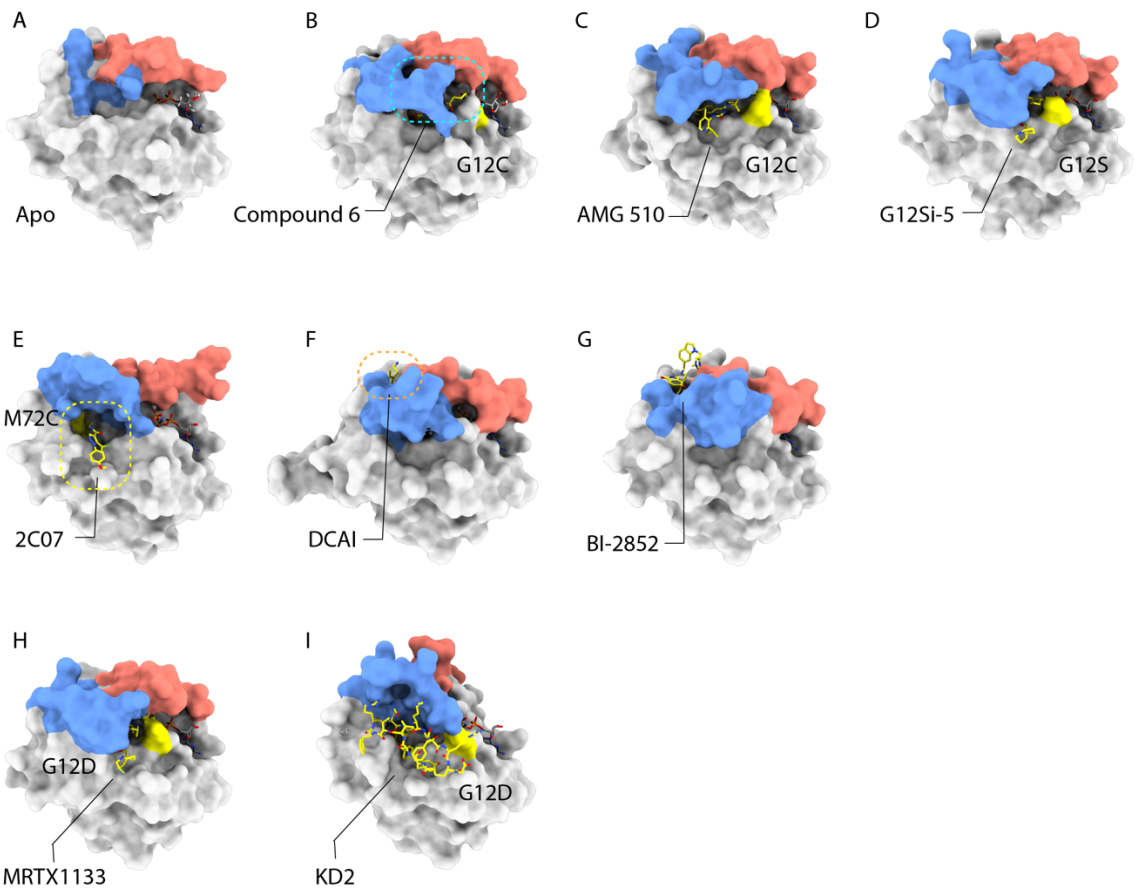

Figure 1.5 | Structures of RAS surfaces targeted by covalent or non-covalent molecules. (A) Crystal structure of GDP-bound WT K-Ras (PDB ID: 4LPK). **(B)** Crystal structure of compound6-bound K-Ras^{G12C}/GDP (PDB ID: 4LUC). **(C)** Crystal structure of AMG510-bound K-Ras^{G12C}/GDP (PDB ID: 6OIM). **(D)** Crystal structure of G12Si-5-bound K-Ras^{G12s}/GDP (PDB ID: 7TLG). **(E)** Crystal structure of 2C07-bound K-Ras^{M72C}/GDP (PDB ID: 5VBZ). **(F)** Crystal structure of DCAI-bound WT K-Ras/GCP (PDB ID: 4DST). **(G)** Crystal structure of BI-2852-bound K-Ras^{G12D}/GCP (PDB ID: 6GJ8). **(H)** Crystal structure of MRTX1133-bound K-Ras^{G12D}/GDP (PDB ID: 7RPZ). **(I)** Crystal structure of KD2-bound K-Ras^{G12D}/GNP (PDB ID: 6WGN). Switch I was highlighted with salmon, Switch II was highlighted with cornflower blue, Ras-targeting molecules were highlighted with yellow sticks. The switch II pocket was highlighted with a cyan box, the switch II groove was highlighted with a yellow box, the DCAI pocket was highlighted with an orange box.

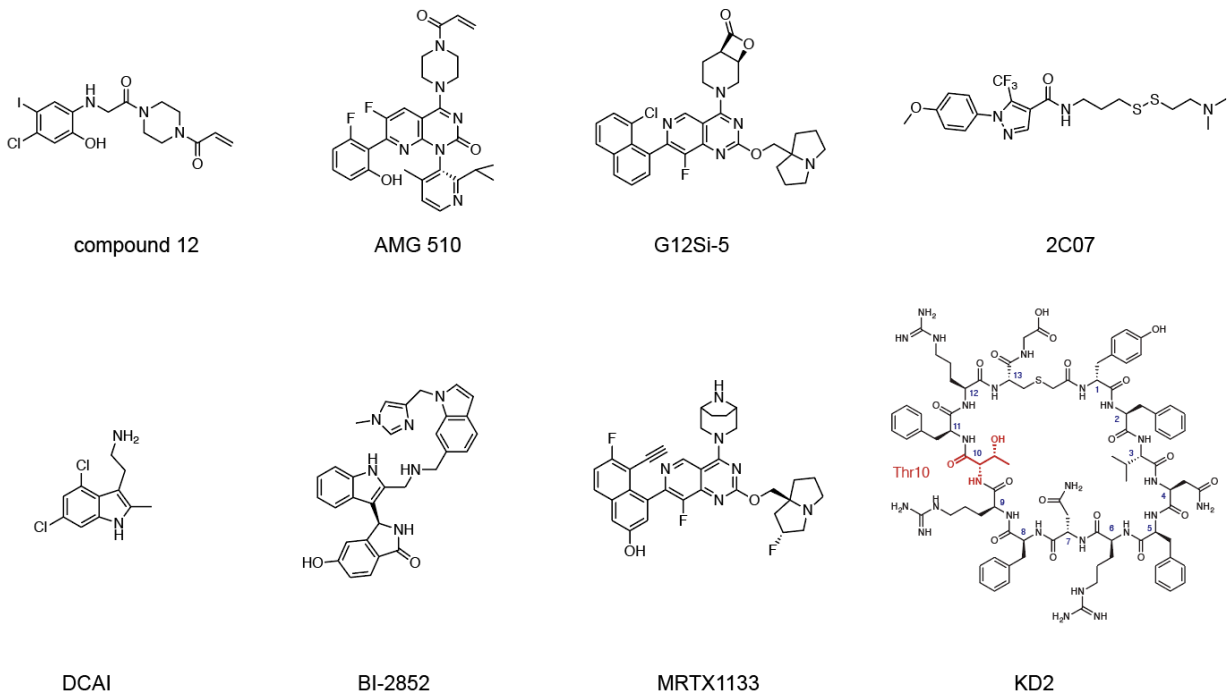

Figure 1.6 | Chemical structure of the Ras-targeting molecules.

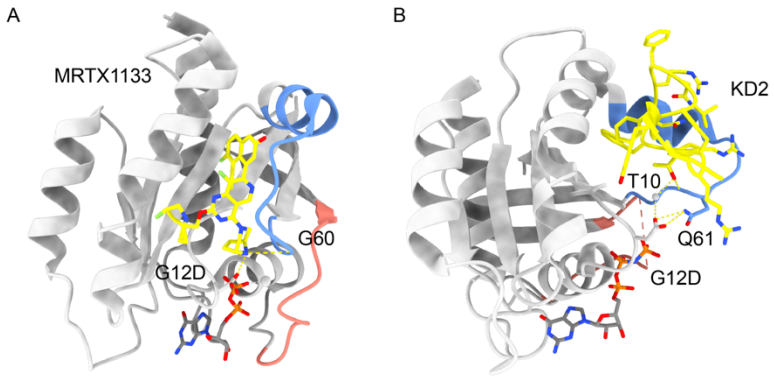

Figure 1.7 | The mutant selectivity of MRTX1133 and KD2. (A) Crystal structure of MRTX1133-bound K-Ras^{G12D}/GDP (PDB ID: 7RPZ). **(B)** Crystal structure of KD2-bound K-Ras^{G12D}/GNP (PDB ID: 6WGN). Switch I was highlighted with salmon, Switch II was highlighted with cornflower blue, Ras-targeting molecules were highlighted with yellow sticks. Key interactions were highlighted with yellow dashed lines.

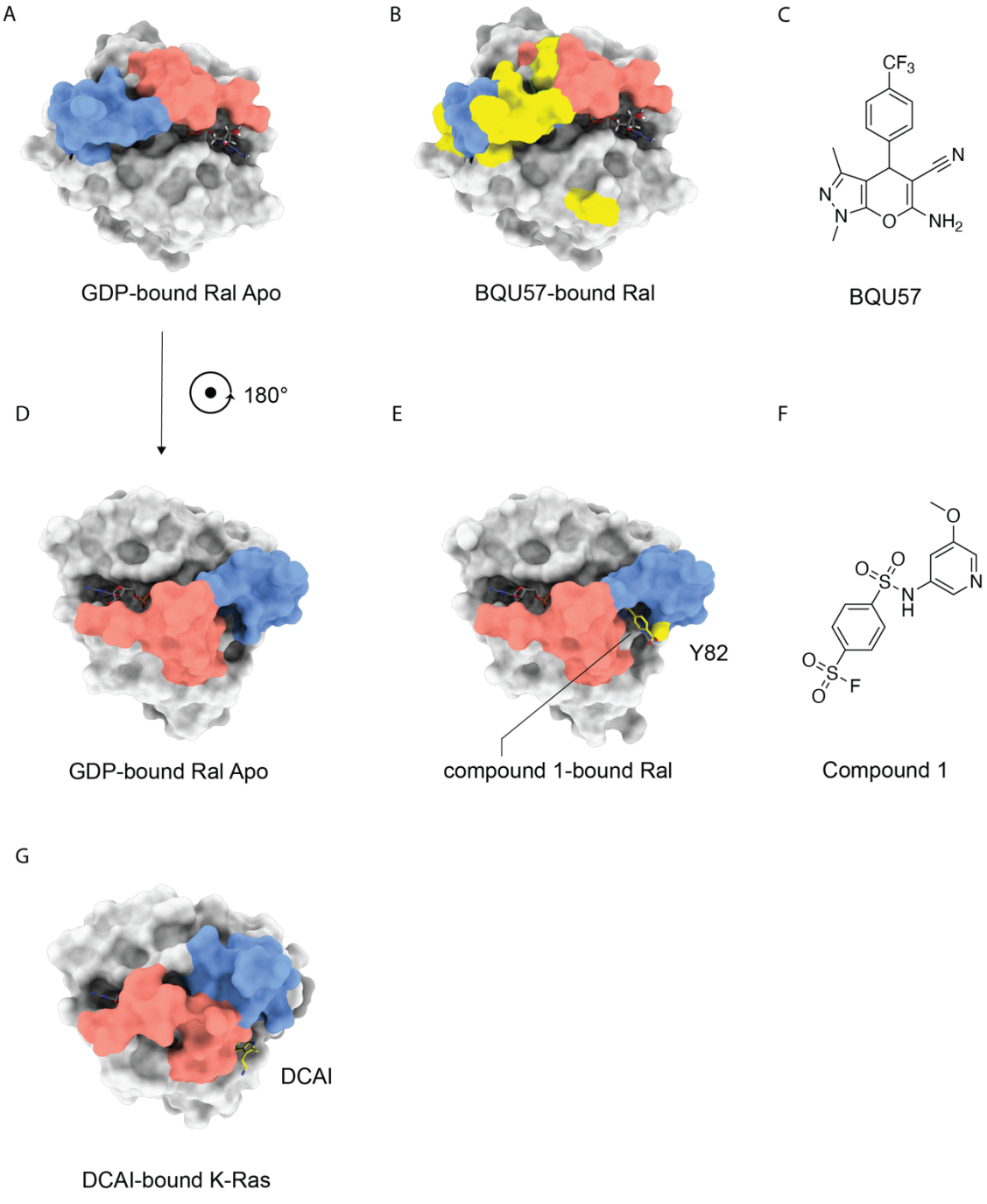
A
B
C
GDP-bound Ral Apo
BQU57-bound Ral
BQU57
180°
D
E
F
GDP-bound Ral Apo
Y82
compound 1-bound Ral
Compound 1
G
DCAI
DCAI-bound K-Ras

Figure 1.8 | Structures of Ral surfaces targeted by covalent or non-covalent molecules. (A, D) Crystal structure of GDP-bound WT RalA (PDB ID: 6P0O). **(B)** ^{15}N-TROSY experiment of 100 μM RalB–GDP in the presence of 100 μM BQU57 was performed. RalB residues showing significant chemical shift changes (yellow) were mapped to their locations on a homologous structure of GDP-bound WT RalA (PDB ID, 6P0O). **(C)** Chemical structure of BQU57. **(E)** Crystal structure of compound 1-bound RalA^{WT}/GDP (PDB ID: 6P0I). **(F)** Chemical structure of compound 1. **(G)** Crystal structure of DCAI-bound WT K-Ras/GCP (PDB ID: 4DST). Switch I was highlighted with salmon, Switch II was highlighted with cornflower blue, Ral-targeting molecules were highlighted with yellow sticks.

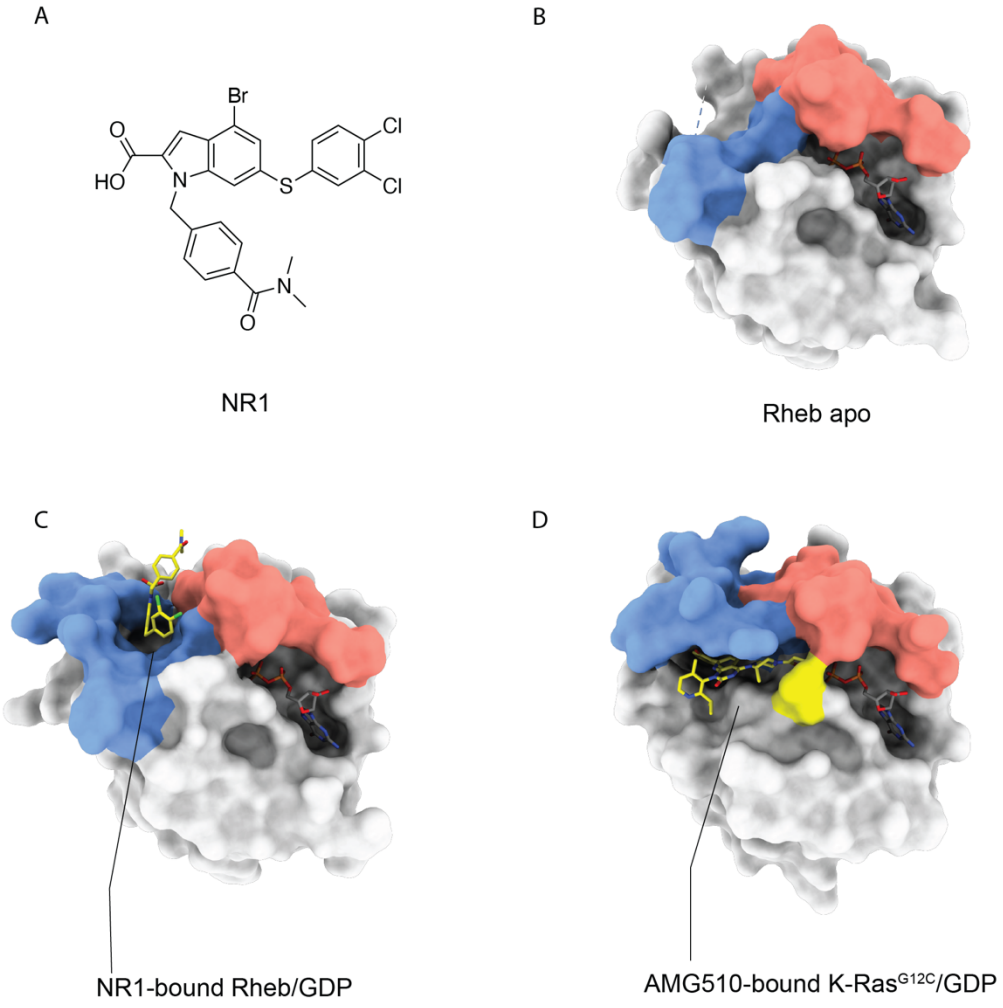

Figure 1.9 | Structures of Rheb surfaces targeted by NR1. (A) Chemical structure of NR1. **(B)** Crystal structure of GDP-bound WT Rheb (PDB ID: 5YXH). **(C)** Crystal structure of NR1-bound Rheb^{WT}/GDP (PDB ID: 6BT0). **(D)** Crystal structure of AMG510-bound K-Ras^{G12C}/GDP (PDB ID: 6OIM). Switch I was highlighted with salmon, Switch II was highlighted with cornflower blue, NR1 was highlighted with yellow sticks.

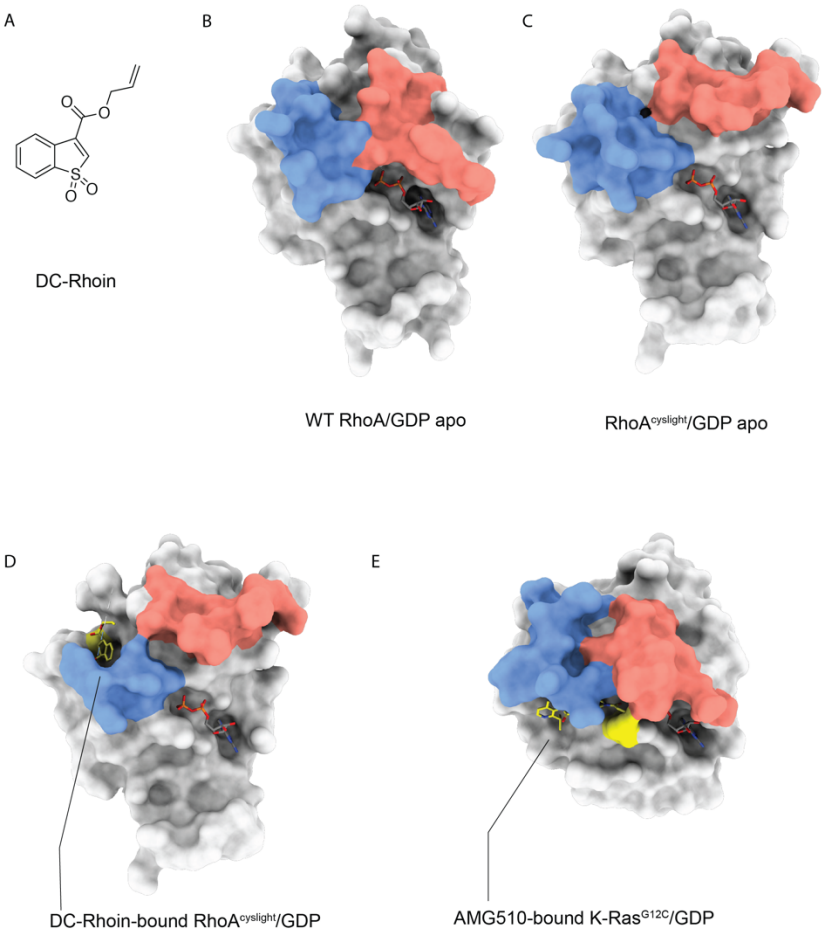

Figure 1.10 | Structures of RhoA surfaces targeted by DC-Rhoin. (A) Chemical structure of DC-Rhoin. **(B)** Crystal structure of GDP-bound WT RhoA (PDB ID: 1FTN). **(C)** Crystal structure of GDP-bound RhoA^{cyslight} (PDB ID: 6KX2). **(D)** Crystal structure of DC-Rhoin-bound RhoA^{cyslight}/GDP (PDB ID: 6KX3). **(E)** Crystal structure of AMG510-bound K-Ras^{G12C}/GDP (PDB ID: 6OIM). Switch I was highlighted with salmon, Switch II was highlighted with cornflower blue, DC-Rhoin was highlighted with yellow sticks.

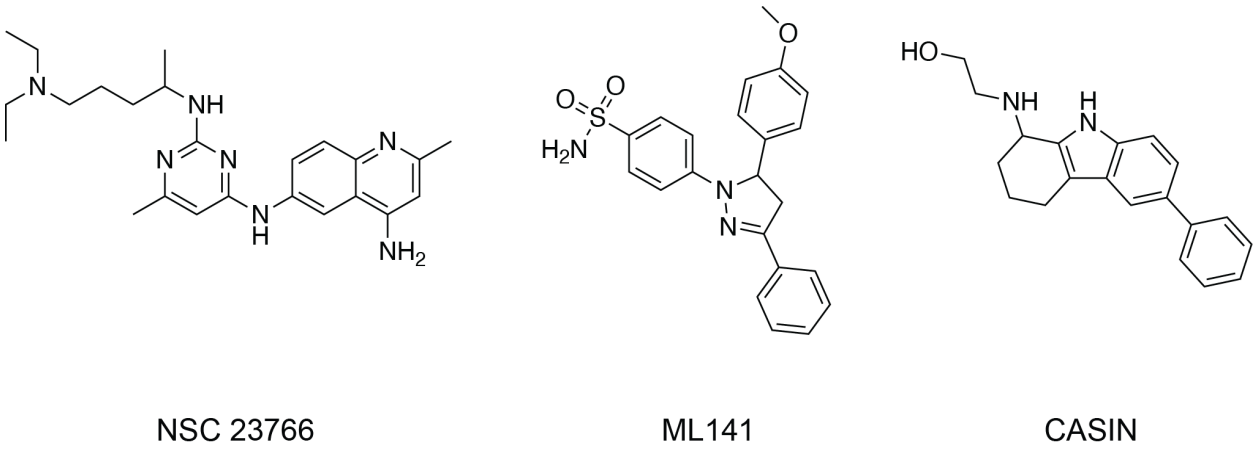

Figure 1.11 | Chemical structures of Rho family GTPase targeting molecules. (A) Chemical structure of NSC 23766, a selective Rac1 inhibitor. **(B)** Chemical structure of ML141, a selective Cdc42 inhibitor. **(C)** Chemical structure of CASIN, a selective Rac1 inhibitor.

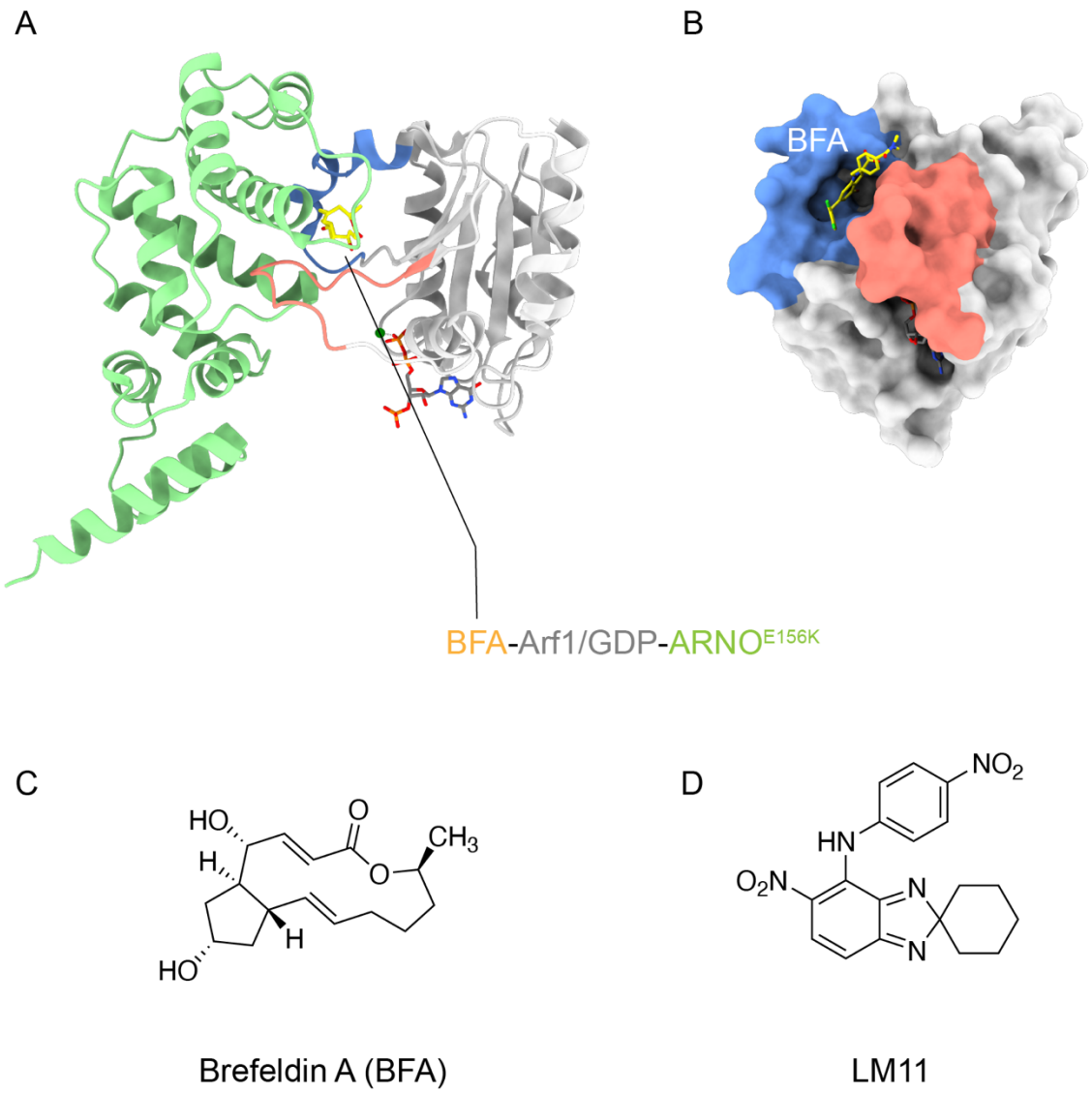

Figure 1.12 | The natural product Brefeldin A (BFA) inhibited the Arf1-GEF complex. (A and B) Crystal structure of BFA-bound Arf1/GDP/ARNO^{E156K} complex (A) (PDB ID: 1R8Q). ARNO^{E156K} was hiddgen in (B). **(C)** Chemical structure of Brefeldin A. **(D)** Chemical structure of LM11. Switch I was highlighted with salmon, Switch II was highlighted with cornflower blue, BFA was highlighted with yellow sticks.

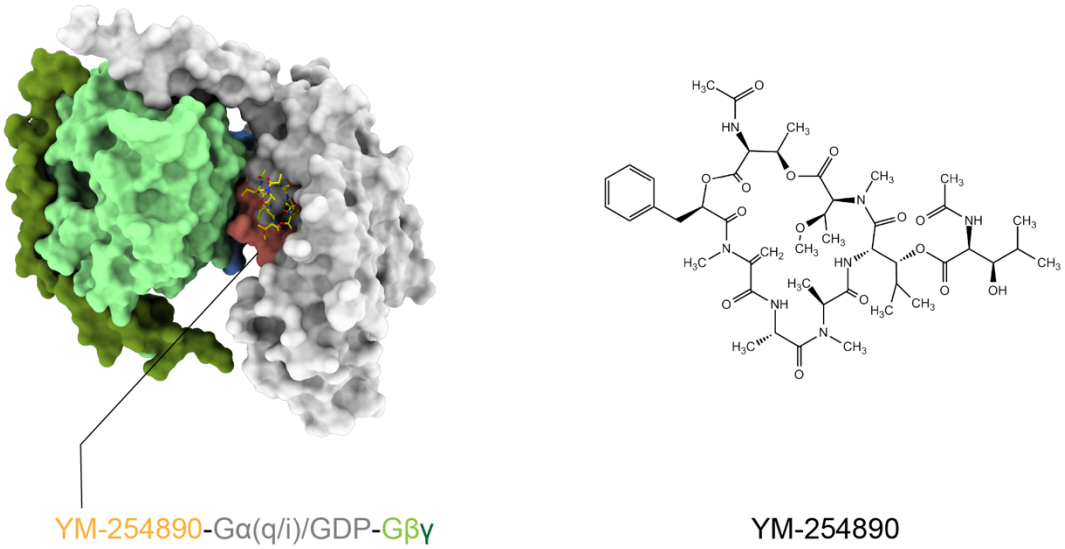

Figure 1.13 | The natural product YM-254890 inhibited the Gα(q/i)/GDP-Gβγ complex. (A) Crystal structure of YM-254890-bound Gα(q/i)/GDP-Gβγ complex (PDB ID: 3AH8). **(C)** Chemical structure of Brefeldin A. **(D)** Chemical structure of YM-254890. Switch I was highlighted with salmon, Switch II was highlighted with cornflower blue, YM-254890 was highlighted with yellow sticks.

References

Abe, H., Kamai, T., Shirataki, H., Oyama, T., Arai, K., and Yoshida, K.I. (2008). High expression of Ran GTPase is associated with local invasion and metastasis of human clear cell renal cell carcinoma. Int. J. Cancer. *122*, 2391–2397.

Agola, J.O., Hong, L., Surviladze, Z., Ursu, O., Waller, A., Strouse, J.J., Simpson, D.S., Schroeder, C.E., Oprea, T.I., Golden, J.E., et al. (2012). A competitive nucleotide binding inhibitor: In vitro characterization of Rab7 GTPase inhibition. ACS Chem. Biol. *7*, 1095–1108.

Alan Hall, C.J.M.N.K.S.& R.A.W. (1983). Identification of transforming gene in two human sarcoma cell lines as a new member of the ras gene family located on chromosome 1. Nature *303*, 396–400.

Ambruso, D.R., Knall, C., Abell, A.N., Panepinto, J., Kurkchubasche, A., Thurman, G., Gonzalez-Aller, C., Hiester, A., deBoer, M., Harbeck, R.J., et al. (2000). Human neutrophil immunodeficiency syndrome is associated with an inhibitory Rac2 mutation. Proc. Natl. Acad. Sci. U.S.A. *97*, 4654-4659.

Belbachir, Nadjet., Portero, V., and Sayed, Z. (2019). RRADmutation causes electrical andcytoskeletal defects in cardiomyocytes derivedfrom a familial case of Brugada syndrome. Eur. Heart J. *40*, 3094–3096.

Bem, D., Yoshimura, S.I., Nunes-Bastos, R., Bond, F.C., Kurian, M.A., Rahman, F., Handley, M.T.W., Hadzhiev, Y., Masood, I., Straatman-Iwanowska, A.A., et al. (2011). Erratum: Loss-of-function mutations in RAB18 cause warburg micro syndrome. Am. J. Hum. Genet. *88*, 499-507.

Berger, A.H., Imielinski, M., Duke, F., Wala, J., Kaplan, N., Shi, G.X., Andres, D.A., and Meyerson, M. (2014). Oncogenic RIT1 mutations in lung adenocarcinoma. Oncogene *33*, 4418–4423.

Boudhraa, Z., Carmona, E., Provencher, D., and Mes-Masson, A.M. (2020). Ran GTPase: A Key Player in Tumor Progression and Metastasis. Front. Cell Dev. Biol. *8*, 345.

Bourne, H.R., Sanders, D.A., and Mccormick, F. (1991). The GTPase superfamily: conserved structure and molecular mechanism. Nature *349*, 117-127.

Bum-Erdene, K., Liu, D., Gonzalez-Gutierrez, G., Ghozayel, M.K., Xu, D., and Meroueh, S.O. (2020). Small-molecule covalent bond formation at tyrosine creates a binding site and inhibits activation of Ral GTPases. Proc. Natl. Acad. Sci. U.S.A. *117*, 7131-7139.

Canon, J., Rex, K., Saiki, A.Y., Mohr, C., Cooke, K., Bagal, D., Gaida, K., Holt, T., Knutson, C.G., Koppada, N., et al. (2019). The clinical KRAS(G12C) inhibitor AMG 510 drives anti-tumour immunity. Nature *575*, 217–223.

Cavé, H., Caye, A., Ghedira, N., Capri, Y., Pouvreau, N., Fillot, N., Trimouille, A., Vignal, C., Fenneteau, O., Alembik, Y., et al. (2016). Mutations in RIT1 cause Noonan syndrome with possible juvenile myelomonocytic leukemia but are not involved in acute lymphoblastic leukemia. Eur. J. Hum. Genet. *24*, 1124–1131.

Colicelli, J. (2004). Human RAS superfamily proteins and related GTPases. Sci STKE *2004*, re13-re13.

Davis, M.J., Ha, B.H., Holman, E.C., Halaban, R., Schlessinger, J., and Boggon, T.J. (2013). RAC1P29S is a spontaneously activating cancer-associated GTPase. Proc. Natl. Acad. Sci. U.S.A. *110*, 912–917.

Didsburys, J., Weber, R.F., Bokochqt, G.M., Evans, T., and Snyderman, R. (1989). Rac, a Novel ras-related Family of Proteins That Are Botulinum Toxin Substrates. J. Biol. Chem. *264*, 16378-16382.

Ehrhardt, G.R.A., Leslie, K.B., Lee, F., Wieler, J.S., and Schrader, J.W. (1999). M-Ras, a Widely Expressed 29-kD Homologue of p21 Ras: Expression of a Constitutively Active Mutant Results in Factor-Independent Growth of an Interleukin-3-Dependent Cell Line. Blood, Am. J. Hematol. 94(7), 2433-2444.

Ellis, C.A., Vos, M.D., Howell, H., Vallecorsa, T., Fults, D.W., and Clark, G.J. (2002). Rig is a novel Ras-related protein and potential neural tumor suppressor. Proc. Natl. Acad. Sci. U.S.A. *99*, 9876-9881.

Finlin, B.S., Gau, C.L., Murphy, G.A., Shao, H., Kimel, T., Seitz, R.S., Chiu, Y.F., Botstein, D., Brown, P.O., Der, C.J., et al. (2001). RERG Is a Novel ras-related, Estrogen-regulated and Growth-inhibitory Gene in Breast Cancer. J. Biol. Chem. *276*, 42259–42267.

Florian, M.C., Dörr, K., Niebel, A., Daria, D., Schrezenmeier, H., Rojewski, M., Filippi, M.D., Hasenberg, A., Gunzer, M., Scharffetter-Kochanek, K., et al. (2012). Cdc42 activity regulates hematopoietic stem cell aging and rejuvenation. Cell Stem Cell *10*, 520–530.

Fratti, R.A., Backer, J.M., Gruenberg, J., Corvera, S., and Deretic, V. (2001). Role of phosphatidylinositol 3-kinase and Rab5 effectors in phagosomal biogenesis and mycobacterial phagosome maturation arrest. J. Cell Biol. *154*, 631–644.

Gao, Y., Dickerson, J.B., Guo, F., Zheng, J., and Zheng, Y. (2004). Rational design and characterization of a Rac GTPase-specific small molecule inhibitor. Proc. Natl. Acad. Sci. U.S.A. *101*, 7618-7623.

Garcia-Marcos, M., Ghosh, P., and Farquhar, M.G. (2011). Molecular basis of a novel oncogenic mutation in GNAO1. Oncogene *30*, 2691–2696.

Gentile, D.R., Rathinaswamy, M.K., Jenkins, M.L., Moss, S.M., Siempelkamp, B.D., Renslo, A.R., Burke, J.E., and Shokat, K.M. (2017). Ras Binder Induces a Modified Switch-II Pocket in GTP and GDP States. Cell Chem. Biol. *24*, 1455-1466.e14.

Geoffrey M. Cooper (1982). Cellular Transforming Genes. Science (1979) *218*, 801–806.

Gómez-Suaga, P., Rivero-Ríos, P., Fdez, E., Ramírez, M.B., Ferrer, I., Aiastui, A., de Munain, A.L., and Hilfiker, S. (2014). LRRK2 delays degradative receptor trafficking by impeding late endosomal budding through decreasing Rab7 activity. Hum. Mol. Genet. *23*, 6779–6796.

Graham, S.M., Cox, A.D., Drivas, G., Rush, M.G., D'eustachio, P., Channing, A., and Der, C.J. (1994). Aberrant Function of the Ras-Related Protein TC21/R-Ras2 Triggers Malignant Transformation. Mol. Cell. Biol. *14*, 4108-4115.

Guadagno, N.A., and Progida, C. (2019). Rab GTPases: Switching to human diseases. Cells *8*, 909.

Harvey, J.J. (1957). An Unidentified Virus which causes the Rapid Production of Tumours in Mice. Nature *204*, 1104-1105.

Hong, L., Kenney, S.R., Phillips, G.K., Simpson, D., Schroeder, C.E., Nöth, J., Romero, E., Swanson, S., Waller, A., Strouse, J.J., et al. (2013). Characterization of a Cdc42 protein inhibitor and its use as a molecular probe. J. Biol. Chem. *288*, 8531–8543.

Hunter, J.C., Manandhar, A., Carrasco, M.A., Gurbani, D., Gondi, S., and Westover, K.D. (2015). Biochemical and structural analysis of common cancer-associated KRAS mutations. Mol. Cancer Res. *13*, 1325–1335.

Jones, B., Jones, E.L., Bonney, S.A., Patel, H.N., Mensenkamp, A.R., Eichenbaum-Voline, S., Rudling, M., Myrdal, U., Annesi, G., Naik, S., et al. (2003). Mutations in a Sar1 GTPase of COPII vesicles are associated with lipid absorption disorders. Nat. Genet. *34*, 29–31.

Kessler, D., Gmachl, M., Mantoulidis, A., Martin, L.J., Zoephel, A., Mayer, M., Gollner, A., Covini, D., Fischer, S., Gerstberger, T., et al. (2019). Drugging an undruggable pocket on KRAS. Proc. Natl. Acad. Sci. U.S.A. *116*, 15823–15829.

Kitayama, H., Sugimoto, Y., Matsuzaki, T., Ikawa, Y., and Noda, M. (1989). A ras-Related Gene with Transformation Suppressor Activity. Cell *56*, 77-84.

Lapadula, D., Farias, E., Randolph, C.E., Purwin, T.J., McGrath, D., Charpentier, T.H., Zhang, L., Wu, S., Terai, M., Sato, T., et al. (2019). Effects of oncogenic Gαq and Gα11 inhibition by FR900359 in uveal melanoma. Mol. Cancer Res. *17*, 963–973.

Leipe, D.D., Wolf, Y.I., Koonin, E. v., and Aravind, L. (2002). Classification and evolution of P-loop GTPases and related ATPases. J. Mol. Biol. *317*, 41–72.

Liu, S., Sawada, T., Lee, S., Yu, W., Silverio, G., Alapatt, P., Millan, I., Shen, A., Saxton, W., Kanao, T., et al. (2012). Parkinson's disease-associated kinase PINK1 regulates miro protein level and axonal transport of mitochondria. PLoS Genet. *8*, e1002537.

Lu, Z.H., Shvartsman, M.B., Lee, A.Y., Shao, J.M., Murray, M.M., Kladney, R.D., Fan, D., Krajewski, S., Chiang, G.G., Mills, G.B., et al. (2010). Mammalian target of rapamycin activator RHEB is frequently overexpressed in human carcinomas and is critical and sufficient for skin epithelial carcinogenesis. Cancer Res. *70*, 3287–3298.

Parada, L. F., Tabin, C. J., Shih, C., & Weinberg, R. A. (1982). Human EJ bladder carcinoma oncogene is homologue of Harvey sarcoma virus ras gene. Nature *297*, 474–478.

Mahoney, S.J., Narayan, S., Molz, L., Berstler, L.A., Kang, S.A., Vlasuk, G.P., and Saiah, E. (2018). A small molecule inhibitor of Rheb selectively targets mTORC1 signaling. Nat. Commun. *9*, 1-12.

Malumbres, M., and Barbacid, M. (2002). RASoncogenes: the first 30 years. Nat. Rev. Cancer *3*, 7–13.

Marshall, C.J., Hall, A., and Weiss, R.A. (1982). A transforming gene present in human sarcoma cell lines. Nature *299*, 171-173.

Maurer, T., Garrenton, L., and Fang, G. (2012). Small-molecule ligands bind to a distinctpocket in Ras and inhibit SOS-mediatednucleotide exchange activity. Proc. Natl. Acad. Sci. U.S.A. *109*, 5299–5304.

Mazhab-Jafari, M.T., Marshall, C.B., Ishiyama, N., Ho, J., di Palma, V., Stambolic, V., and Ikura, M. (2012). An autoinhibited noncanonical mechanism of GTP hydrolysis by Rheb maintains mTORC1 homeostasis. Structure *20*, 1528–1539.

McCormick, F. (1998). Going for the GAP. Curr. Biol. *8*, R673-R675.

McCray, B.A., Skordalakes, E., and Taylor, J.P. (2010). Disease mutations in Rab7 result in unregulated nucleotide exchange and inappropriate activation. Hum. Mol. Genet. *19*, 1033–1047.

Ménasché, G., Pastural, E., Feldmann, J., Certain, S., Ersoy, F., Dupuis, S., Wulffraat, N., Bianchi, D., Fischer, A., le Deist, F., et al. (2000). Mutations in RAB27A cause Griscelli syndrome associated with haemophagocytic syndrome. Nat. Genet. *25*, 173-176.

Neal, S. E., Eccleston, J. F., Hall, A., and Webb, M. R. (1988). Kinetic analysis of the hydrolysis of GTP by p21N-ras. The basal GTPase mechanism J. Biol. Chem. *263*, 19718-19722.

Nishimura, A., Kitano, K., Takasaki, J., Taniguchi, M., Mizuno, N., Tago, K., Hakoshima, T. and Itoh, H. (2010). Structural basis for the specific inhibition of heterotrimeric Gq protein by a small molecule. Proc. Natl. Acad. Sci. U.S.A. *107*, 13666-13671.

O'Hayre, M., Vázquez-Prado, J., Kufareva, I., Stawiski, E.W., Handel, T.M., Seshagiri, S., and Gutkind, J.S. (2013). The emerging mutational landscape of G proteins and G-protein-coupled receptors in cancer. Nat. Rev. Cancer *13*, 412–424.

Ostrem, J.M., Peters, U., Sos, M.L., Wells, J.A., and Shokat, K.M. (2013). K-Ras(G12C) inhibitors allosterically control GTP affinity and effector interactions. Nature *503*, 548–551.

Palsuledesai, C.C., Surviladze, Z., Waller, A., Miscioscia, T.F., Guo, Y., Wu, Y., Strouse, J., Romero, E., Salas, V.M., Curpan, R., et al. (2018a). Activation of Rho Family GTPases by Small Molecules. ACS Chem. Biol. *13*, 1514–1524.

Parri, M., and Chiarugi, P. (2010). Rac and Rho GTPases in cancer cell motility control. Cell Commun. Signal. *8*, 1-14.

Quilliam, L.A., Rebhun, J.F., and Castro, A.F. (2002). A growing family of guanine nucleotide exchange factors is responsible for activation of ras-family GTPases. Prog. Nucleic Acid Res. Mol. Biol. *71*, 391–444.

Renault, L., Guibert, B., and Cherfils, J. (2003). Structural snapshots of the mechanism and inhibition of a guanine nucleotide exchange factor. Nature *426*, 525-530.

Sakata-Yanagimoto, M., Enami, T., Yoshida, K., Shiraishi, Y., Ishii, R., Miyake, Y., Muto, H., Tsuyama, N., Sato-Otsubo, A., Okuno, Y., et al. (2014). Somatic RHOA mutation in angioimmunoblastic T cell lymphoma. Nat. Genet. *46*, 171–175.

Santos, E., Tronick, S.R., Aaronson, S.A., Pulciani, S., and Barbacid, M. (1982). T24 human bladder carcinoma oncogene is an activated form of the normal human homologue of BALB-and Harvey-MSV transforming genes. Nature *298*, 343-347.

Schaefer, A., and Der, C.J. (2022). RHOA takes the RHOad less traveled to cancer. Trends in Cancer.

Schlienger, S., Campbell, S., Pasquin, S., Gaboury, L., and Claing, A. (2016). ADP-ribosylation factor 1 expression regulates epithelial-mesenchymal transition and predicts poor clinical outcome in triple-negative breast cancer. Oncotarget *7*, 15811.

Seabra, M.C., Ho, Y.K., and Anant, J.S. (1995). Deficient Geranylgeranylation of Ram/Rab27 in Choroideremia. J. Biol. Chem. *270*, 24420-24427.

Shimizu, K., Goldfarb, M., Perucho, M., and Wiglert, M. (1983). Isolation and preliminary characterization of the transforming gene of a human neuroblastoma cell line (DNA-mediated gene transfer/human oncogene/tiINA suppressor). Proc. Natl. Acad. Sci. U.S.A. *80*, 383-387.

Shoubridge, C., Tarpey, P.S., Abidi, F., Ramsden, S.L., Rujirabanjerd, S., Murphy, J.A., Boyle, J., Shaw, M., Gardner, A., Proos, A., et al. (2010). Mutations in the guanine nucleotide exchange factor gene IQSEC2 cause nonsyndromic intellectual disability. Nat. Genet. *42*, 486–488.

Sohn, Y.S., Shin, H.C., Park, W.S., Ge, J., Kim, C.H., Lee, B.L., Do, W.H., Jung, J.U., Rigden, D.J., and Oh, B.H. (2015). Lpg0393 of Legionella pneumophila is a guanine-nucleotide exchange factor for Rab5, Rab21 and Rab22. PLoS One *10*, e0118683.

Stengel, K., and Zheng, Y. (2011). Cdc42 in oncogenic transformation, invasion, and tumorigenesis. Cell. Signal *23*, 1415–1423.

Straub, J., Konrad, E.D.H., Grüner, J., Toutain, A., Bok, L.A., Cho, M.T., Crawford, H.P., Dubbs, H., Douglas, G., Jobling, R., et al. (2018). Missense Variants in RHOBTB2 Cause a Developmental and Epileptic Encephalopathy in Humans, and Altered Levels Cause Neurological Defects in Drosophila. Am. J. Hum. Genet. *102*, 44–57.

Sun, Z., Zhang, H., Zhang, Y., Liao, L., Zhou, W., Zhang, F., Lian, F., Huang, J., Xu, P., Zhang, R., et al. (2020). Covalent Inhibitors Allosterically Block the Activation of Rho Family Proteins and Suppress Cancer Cell Invasion. Adv. Sci. *7*, 2000098.

Tam, V.H.K., Chen, S.P.L., Mak, C.M., Fung, L.M., Lee, C.Y., and Chan, A.Y.W. (2014). A novel mutation in pseudohypoparathyroidism type 1a in a Chinese woman and her son with hypocalcaemia. Hong Kong Med. J. *20*, 258–260.

Taparowsky, E., Suard, Y., Fasano, O., Shimizu, K., Goldfarb, M., and Wigler, M. (1982). Activation of the T24 bladder carcinoma transforming gene is linked to a single amino acid change. Nature *300*, 762-765.

Thomas, P., Pranatharthi, A., Ross, C., and Srivastava, S. (2019). RhoC: a fascinating journey from a cytoskeletal organizer to a Cancer stem cell therapeutic target. J Exp Clin Cancer Res. *38*, 328.

Urano, T., Emkey, R., and Feig, L.A. (1996). Ral-GTPases mediate a distinct downstream signaling pathway from Ras that facilitates cellular transformation. EMBO J. *15*, 810–816.

Viaud, J., Zeghouf, M., Lè Ne Barelli, H., Zeeh, J.-C., Padilla, A., Guibert, B., Chardin, P., Royer, C.A., Cherfils, J., and Chavanieu, A. (2007). Structure-based discovery of an inhibitor of Arf activation by Sec7 domains through targeting of protein-protein complexes. Proc. Natl. Acad. Sci. U.S.A. *104*, 10370-10375.

Wang, S., Hu, C., Wu, F., and He, S. (2017). Rab25 GTPase: Functional roles in cancer. Oncotarget *8*, 64591.

Wang, X., Winter, D., Ashrafi, G., Schlehe, J., Wong, Y.L., Selkoe, D., Rice, S., Steen, J., Lavoie, M.J., and Schwarz, T.L. (2011). PINK1 and Parkin target miro for phosphorylation and degradation to arrest mitochondrial motility. Cell *147*, 893–906.

Wang, X., Allen, S., Blake, J.F., Bowcut, V., Briere, D.M., Calinisan, A., Dahlke, J.R., Fell, J.B., Fischer, J.P., Gunn, R.J., et al. (2022). Identification of MRTX1133, a Noncovalent, Potent, and Selective KRASG12DInhibitor. J. Med. Chem. *65*, 3123–3133.

Welsch, M.E., Kaplan, A., Chambers, J.M., Stokes, M.E., Bos, P.H., Zask, A., Zhang, Y., Sanchez-Martin, M., Badgley, M.A., Huang, C.S., et al. (2017). Multivalent Small-Molecule Pan-RAS Inhibitors. Cell *168*, 878-889.e29.

Wennerberg, K., Rossman, K.L., and Der, C.J. (2005). The Ras superfamily at a glance. J. Cell Sci. *118*, 843–846.

Wheeler, D.B., Zoncu, R., Root, D.E., Sabatini, D.M., and Sawyers, C.L. (2015). Identification of an oncogenic RAB protein. Science *350*, 211–217.

Yan, C., Liu, D., Li, L., Wempe, M.F., Guin, S., Khanna, M., Meier, J., Hoffman, B., Owens, C., Wysoczynski, C.L., et al. (2014). Discovery and characterization of small molecules that target the GTPase Ral. Nature *515*, 443–447.

Zhang, Z., Gao, R., Hu, Q., Peacock, H., Matthew Peacock, D., Dai, S., Shokat, K.M., and Suga, H. (2020). GTP-state-selective cyclic peptide ligands of K-ras(G12D) block its interaction with Raf. ACS Cent. Sci. *6*, 1753–1761.

Zhang, Z., Guiley, K.Z., and Shokat, K.M. (2022). Chemical acylation of an acquired serine suppresses oncogenic signaling of K-Ras(G12S). Nat. Chem. Biol. 1-7.

Chapter 2
Discovery of conformation-selective cyclic peptide inhibitors targeting Gαs

Abstract

The G protein-coupled receptor cascade leading to production of the second messenger cAMP is replete with pharmacologically targetable proteins with the exception of the Gα subunit, Gαs. GTPases remain largely undruggable given the difficulty of displacing high-affinity guanine nucleotides and the lack of other drug binding sites. We explored a chemical library of 10^{12} cyclic peptides to expand the chemical search for inhibitors of this enzyme class. We identified two macrocyclic peptides, GN13 and GD20, that antagonize the active and inactive states of Gαs, respectively. Both macrocyclic peptides fine-tune Gαs activity with high nucleotide-binding-state selectivity and G protein class-specificity. Co-crystal structures reveal that GN13 and GD20 distinguish the conformational differences within the switch II/α3 pocket. Cell-permeable analogs of GN13 and GD20 modulate Gαs/Gβγ signaling in cells through binding to crystallographically defined pockets. The discovery of cyclic peptide inhibitors targeting Gαs provides path for further development of state-dependent GTPase inhibitors.

Introduction

The family of human GTPases represents a vast but largely untapped source of pharmacological targets. They serve as key molecular switches that control cell growth and proliferation through cycling between tightly regulated ON/OFF states. The role of specific GTPase family members across diverse human diseases have been widely established by cancer genome sequencing (e.g., KRAS, GNAS and others) and by familial studies in neurodegenerative disease (e.g. LRRK2, RAB39B) (Prior et al., 2012; O'Hayre et al., 2013; Alessi and Sammler, 2018; Wilson et al., 2014). Despite the widespread recognition of these disease target relationships, only very recently has the first drug targeting a GTPase K-Ras (G12C) achieved clinical proof of

principle (Canon et al., 2019; Hallin et al., 2020). The covalent somatic cysteine mutant-specific nature of the K-Ras (G12C) drugs has opened the potential for targeting a GTPase for the first time.

Several peptide-based probes that non-covalently target GTPases have been reported, but they either lack proper drug-like properties or have limited target scope (Takasaki, et al., 2004; Ja and Roberts, 2004; Johnston et al., 2005; Johnston et al., 2005; Johnston et al., 2006; Ja et al., 2006; Austin et al., 2008). Short linear peptides have demonstrated the ability to target the switch II/α3 helix region in the heterotrimeric G protein α-subunit (Gα) with high nucleotide binding state selectivity. However, linear peptides are not the ideal molecules for drug discovery because of their poor cell permeability and inherent instability in cells. Cyclic peptides are promising candidates for GTPase drug development. Like linear peptides, cyclic peptides are also capable of targeting protein-protein interfaces (Sohrabi et al., 2020). Peptide cyclization stabilizes the peptide sequence and constrains the flexible peptide conformations for better cell penetration (Dougherty et al., 2019).

Cyclic peptide inhibitors of Gα proteins have been reported: for instance, the macrocyclic depsipeptide natural product YM-254890 targets GDP-bound Gαq with high specificity and potency in cells (Nishimura et al., 2010). Despite the highly conserved structure of G proteins and the recent chemical tractability of fully synthetic YM-254890, efforts to use this natural macrocycle as a scaffold from which to discover inhibitors of other G proteins (Gαs, Gαi) have not been successful (Kaur et al., 2015; Xiong et al., 2016; Zhang et al., 2017), likely because of the limited chemical diversity of available YM-254890 analogs. We therefore reasoned that screening an ultra-large chemical library of cyclic peptides against a given nucleotide binding state of Gαs might allow us to discover Gαs nucleotide-binding-state-selective inhibitors that

discriminate between the active and inactive states of Gαs and potentially open the remainder of the GTPase family to pharmacological studies.

The Random nonstandard Peptide Integrated Discovery (RaPID) system (Yamagishi et al., 2011) is an in vitro display system which merges the flexibility of an in vitro translation system (FIT) (Murakami et al., 2006; Murakami et al., 2003., Ramaswamy et al., 2004; Xiao et al., 2008) with mRNA display, enabling the screening of exceptionally large macrocyclic peptide libraries (> 1012 molecules) against challenging targets (Passioura and Suga, 2017). Here we report the discovery by the RaPID system of GN13 and GD20, two macrocyclic peptides that are the first known cell-permeable, nucleotide-state-selective inhibitors of Gαs, with high selectivity over other G protein subfamilies and nucleotide binding states.

Results

Selection of state-selective cyclic peptides that bind to the active or inactive state of Gαs

Affinity screening hits emerging from the RaPID cyclic peptide selection process against Gαs could theoretically bind anywhere on the surface of the protein and so might or might not perturb its function. To increase the probability of selecting a function-perturbing hit, we took advantage of the fact that when Gαs switches from GDP-bound inactive state to GTP-bound active state significant conformational changes occur on one face of Gαs, comprising the so-called switch I, II and III regions (Lambright et al., 1994), which are known to bind inhibitor or effector protein partners such as Gβγ or adenylyl cyclases (Tesmer et al., 1997; Liu et al., 2019) (Figure 2.1A). We reasoned that performing both a positive selection against one state of Gαs and a negative selection against the other state would enrich for binders to the switch regions, and that these binders would be likely to state-selectively disrupt Gαs function.

In order to select a Gαs active state binding peptide, we performed the positive selection with wild-type Gαs (WT Gαs) bound to the non-hydrolyzable GTP analogue GppNHp (GNP, 5′-guanylyl imidodiphosphate) and the negative selection against GDP-bound WT Gαs. A parallel Gαs inactive state binder selection was performed using GDP-bound WT Gαs as the positive selection and GNP-bound WT Gαs as the negative selection (Figure 2.1B). Starting from a cDNA library, each round of selection included PCR amplification of the cDNA library, in vitro transcription into an mRNA library, ligation with a puromycin linker, and translation to generate a peptide library covalently conjugated with its encoding mRNA library (Figure 2.1C). The library encoded peptides contain an N-chloroacetyl-D-tyrosine at the N-terminus, followed by 8-12 random proteinogenic amino acids encoded by NNK codons, a cysteine residue and a GSGSGS linker (Figure 2.1D and 2.1E). Cyclization occurs spontaneously between the chloroacetyl group and the thiol group of the downstream cysteine residue (or possibly those appeared in the random region). The peptide-ligated mRNA library was further reverse-transcribed into a cDNA-mRNA-peptide library, subjected to a negative selection against one state of Gαs, then followed by a positive selection against the other state of Gαs (Figure 2.1C).

After four rounds of selection (R1-R4), cyclic peptide binders for GNP-bound or GDP-bound Gαs were enriched (Figure 2.2A and 2.2B) and identified by next generation sequencing (NGS). The sequences of the top 20 hits were aligned and shown in Figure 2.1D and 1E. Selective cyclic peptides from the R4 pool were identified and characterized by comparison selection against the respective positive and negative protein baits (Figure 2.1F and 2.1G, see also Figure 2.2C). Nine of the top twenty hits from the active state binder selection (with more than 100-fold selectivity for GNP-bound over GDP-bound Gαs, indicated by red triangles in Figure 2.1D) and eight of the top twenty hits from the inactive state binder selection (with more than 40-fold

selectivity for GDP-bound over GNP-bound Gαs, indicated by blue triangles in Figure 2.1E) were chosen for further analysis. To evaluate the cyclic peptide hits without the appended DNA/mRNA duplex, residues from the N-chloroacetyl-D-tyrosine to the glycine (after the anchor cysteine residue) of the selected peptides were synthesized using solid phase peptide synthesis followed by in situ cyclization.

Active state binding cyclic peptide GN13 blocks Gαs-mediated adenylyl cyclase activation

In order to determine whether Gαs/GNP specific binders inhibit Gαs activity, we assayed the ability of Gαs to activate its downstream effector AC (Figure 2.3A). We refer to resynthesized active state binding cyclic peptides with a "GN" (Gαs/GNP) preceding their ranking number. We first tested the physical interaction between GNP-bound Gαs and AC in the presence of the active sate binders using a fluorescence resonance energy transfer (FRET) assay (Figure 2.4A). Eight out of nine GN peptides showed strong, dose-dependent inhibition of the interaction between Gαs and AC (Figure 2.3B). We then evaluated the inhibitory effect of the top hits on Gαs-mediated AC activation by measuring production of cAMP in a reconstituted Gαs/AC activation assay (Figure 2.3A). Among these nine active state binders, GN13 showed the greatest inhibition, with an IC_{50} of 4.15 ± 1.13 μM (Figure 2.3C and 2.3D). GN13 did not inhibit forskolin-mediated, Gαs-independent AC activation (Figure 2.4B), suggesting a Gαs-dependent mechanism of inhibition. We measured the binding kinetics of GN13 to immobilized GNP-bound Gαs using biolayer interferometry (BLI). GN13 binds to GNP-bound Gαs with a K_D value of 0.19 ± 0.02 μM (Figure 2.4C). By contrast, GN13 showed little to no detectable binding to GDP-bound Gαs (Figure 2.4D).

We sought to test the efficacy of GN13 in β2-adrenergic receptor (β2AR) mediated second messenger stimulation. Membrane anchored GDP-bound Gαs forms a heterotrimer with Gβγ in

the resting state. It can undergo GPCR mediated GDP to GTP exchange upon agonist stimulation (Weis and Kobilka, 2018). The presence of GN13 could potentially capture the newly generated GTP-bound Gαs and inhibit its effector binding (Figure 2.3E). To test this idea, we incubated live HEK293 cells or cell membranes prepared from HEK293 cells with GN13 and examined cAMP accumulation with or without β2AR stimulation by isoproterenol (ISO). Although GN13 showed little inhibition in live HEK293 cells, it inhibited ISO-stimulated Gαs activity in cell membranes to a background level, with an IC_{50} of 12.21 ± 2.51 μM (Figure 2.4E and 2.3F).

The lack of cell activity of GN13 is presumably limited by its poor cell permeability. We sought to improve cell penetration of GN13 by substituting the negatively charged glutamate residue with a glutamine residue at the third position. We quantitatively evaluated the cell permeability of GN13-E3Q with a recently developed HaloTag-based assay known as a chloroalkane penetration assay (CAPA) (Peraro et al., 2018) (Figure 2.4F). HeLa cells stably expressing HaloTag localized to the mitochondrial outer membrane were pulsed with chloroalkane-tagged molecules (ct-molecule), washed, chased with chloroalkane-tagged TAMRA fluorophore (ct-TAMRA), and finally analyzed by flow cytometry. A lower ct-TAMRA fluorescent signal indicates competition from a higher cytosolic concentration of ct-molecule. We conjugated a chloroalkane tag at the carboxyl terminus (C-term) of GN13 (G14) to make ct-GN13-E3Q (Fig. 2.4G). ct-GN13-E3Q exhibited similar biochemical activity to unmodified GN13 (Figure 2.4H), and showed measurable cell penetration and mild Gαs inhibition in live cells (Figure 2.4I and 2.4J). These results indicated that C-term modification and E3Q mutation of GN13 improved its cell permeability while maintaining a proper ligand-protein interaction with Gαs. We further augmented the cellular concentration of GN13-E3Q by adding a polyarginine motif (R8), one of the widely used cell-penetrating peptides (CPPs), at the C-term of GN13 (Figure 2.3G)

(Bechara and Sagan, 2013). cpGN13 significantly inhibited ISO-mediated cAMP production in live HEK293 cells (Figure 2.3H). Our results demonstrated that GN13 and its cell permeable analogs can modulate β2AR agonist stimulated Gαs activity.

The crystal structure of GNP-bound Gαs in complex with GN13

GN13 potently inhibited both short and long isoforms of Gαs, which are splice variants that differ from each other in the hinge region between the Ras domain and the helical domain (Figure 2.6A) (Seifert et al., 1998). We therefore hypothesized that GN13 binds to the conserved effector-binding switch II region of Gαs. To elucidate how the cyclic peptide GN13 binds to Gαs and inhibits Gαs-mediated AC activation, we solved a co-crystal structure of the Gαs/GNP/GN13 complex. The structure was determined by molecular replacement and refined to 1.57 Å (Table 2.2). The overall structure is shown in Figure 3A. GN13 assumes a highly ordered structure through extensive intramolecular and intermolecular hydrogen bonding networks with three well-defined water molecules (Figure 2.6B-D). One molecule of GN13 binds to a pocket between switch II and the α3 helix of GNP-bound Gαs through hydrogen bonding and hydrophobic interactions (Figure 2.5B and 2.5C). Specifically, the side chain of residue E3 in GN13 accepts a hydrogen bond from the ε-amino group of K274 in Gαs; the indole ring of residue W9 in GN13 donates a hydrogen bond to the side chain of E268 in Gαs; the main chain carbonyl oxygens of residues V5, W9 and T11, and the main chain amide of W9 in GN13 form five hydrogen bonds with residues N279, R280, R231, R232, and S275 on switch II and the α3 helix in Gαs (Figure 2.5B). The side chains of residues I8 and W9 (IW motif) in GN13 dock into two hydrophobic pockets on Gαs (Figure 2.5C), giving rise to high Gαs binding affinity.

To validate the contribution of these resides to Gαs/GN13 interaction, we generated Gαs and GN13 alanine mutants and measured their binding using BLI (Figure 2.6F and 2.6G). Although GN13 E3Q mutation retained activity (Figure S2G and S2H), disruption of the hydrogen bond between E3 (GN13) and K274 (Gαs) with alanine mutations reduced binding by nearly 50% (Figure 2.6F and 2.6G). The requirement of a precise Gαs/GN13 hydrogen bond network was also confirmed by a series of Gαs alanine mutants (R231A, R232A, E268A, K274A, and N279A) (Figure 2.6G). Finally, the I8A and W8A mutants of GN13 completely abolished GN13 binding, reassuring the importance of the hydrophobic IW motif (Figure 2.6F).

Structural analysis reveals that residue W9 in GN13 is centrally located within the interface between GN13 and Gαs, contributing three hydrogen bonds as well as hydrophobic interactions with the switch II/α3 pocket (Figure 2.5B and 2.5C). Analogous to this key tryptophan in GN13, AC II (effector of Gαs) residue F991 (Tesmer et al., 1997), PDEγ (effector of G protein transducin, Gt) residue W70 (Slep et al., 2001), and Nb35 (a Gαs binding nanobody) residue F108 (Rasmussen et al., 2011) are inserted into the same switch II/α3 clefts of Gt and Gαs (Figure 2.5E, see also Figure 2.6H and 2.6I). Comparison between the Gαs/GNP/GN13 complex structure and a Gαs/GTPγS/AC complex structure (PDB: 1AZS) suggested that GN13 directly occludes the hydrophobic interaction between Gαs and AC (Tesmer et al., 1997), which accounts for the inhibitory effect of GN13 (Figure 2.5E).

Structural basis for the nucleotide state-selectivity of GN13

The Gαs/GNP/GN13 complex strongly resembles the Gαs/GTPγS structure (PDB: 1AZT) (Sunahara et al., 1997), suggesting that GN13 recognizes the active state conformation and does not induce significant conformational change upon binding (Figure 2.5D). GN13 also inhibited

oncogenic Gαs mutants (R201C, R201H, R201S, and Q227L) (Figure 2.6J), which are locked in the active state conformation with activating mutations in the catalytic site (Hu and Shokat, 2018). We superimposed our structure to the structure of inactive GDP-bound Gαs (chain I in PDB 6EG8) (Liu et al., 2019). In comparison with our structure, the N-terminus of switch II in GDP-bound Gαs is unstructured and adjacent to the α3 helix, with nearly half of the GN13/Gαs interface disrupted (Figure 2.6K). In particular, R232 of switch II (shown in space filling) is predicted to create a steric clash with I8 of GN13. Therefore, the GN13-bound complex structure explains the state-selectivity of GN13 for the active state of Gαs.

To further assess the cellular specificity of GN13, we designed a GN13-resistant Gαs mutant based on structural analysis. We examined the structures of Gαs/GN13 complex and Gαs/AC complex and noticed that serine 275 in Gαs makes close contact with GN13, but does not contact AC (Figure 2.5F and 2.5G). We reasoned that mutating this serine residue to a bulky residue should create a drug-resistant Gαs mutant that blocks GN13/Gαs interaction but would have little effect on AC activation. Indeed, Gαs S275L mutant maintained a similar level of biochemical activity but was resistant to GN13 inhibition (Figure 2.5H, see also Figure 2.6L). We tested GN13 in the membranes of *GNAS*-knockout (*GNAS*-KO) HEK293 cells that did not express endogenous Gαs protein (Stallaert et al., 2017). GN13 was able to inhibit ISO-mediated cAMP production in cell membranes in a dose-dependent manner when WT Gαs was reintroduced into the *GNAS* KO cells by transient transfection. By contrast, when the drug resistant mutant Gαs S275L was reintroduced into the *GNAS* KO cells, the inhibitory effect of GN13 was abolished (Figure 2.5I), providing further evidence that the observed pharmacological activity is due to GN13 binding to the switch II/α3 pocket in Gαs.

Inactive state binding cyclic peptide GD20 is a Gαs specific guanine nucleotide dissociation inhibitor (GDI)

Gα GTPase activity promotes GTP hydrolysis to GDP and rearranges the switch regions to adopt a GDP-bound inactive conformation. This precisely orchestrated nucleotide binding conformation prevents GDP release, which makes GDP dissociation the rate-limiting step of G protein activation (Dror et al., 2015) (Figure 2.7A, left). An inactive state binder could hypothetically modulate GDP-bound Gαs either by inhibiting GDP release as a guanine nucleotide dissociation inhibitor (GDI) or by facilitating the exchange of GDP to GTP serving as a guanine nucleotide exchange factor (GEF) (Ghosh et al., 2017). In order to understand how inactive state binders control GDP-bound Gαs function, we carried out a multiple turnover assay to evaluate Gαs steady-state GTPase activity in the presence of top hits from the inactive state binder selection (Figure 2.7B). The inactive state selected cyclic peptides are indicated with a "GD" (Gαs/GDP) preceding their ranking number, and all of the tested GD peptides showed strong, dose-dependent inhibition against Gαs steady-state GTPase activity. GD20 showed the greatest inhibition, with an IC_{50} of 1.15 ± 0.16 μM (Figure 2.7B and 2.7C, see also Figure 2.8A). Interestingly, GN13 significantly increased Gαs steady-state GTPase activity (Figure 2.8A). In order to understand how GD20 and GN13 regulate Gαs enzymatic activity, we determined rate constants for both GDP dissociation and GTPγS binding in the GTPases cycle. GD20 displayed profound GDI activity towards Gαs by drastically reducing Gαs GDP dissociation rates (k_{off}) and the apparent rate of GTPγS binding (k_{app}) to Gαs (Figure 2.7D and 2.7E). On the contrary, GN13 only slightly influenced Gαs GDP dissociation (Figure S4B). Instead, GN13 increased Gαs GTPγS binding (Figure 2.8C). The discrepancy between GD20, a synthetic Gαs GDI, and GN13, a synthetic Gαs GEF, exemplifies how state-selective Gαs binders fine-tune Gαs enzymatic activity. The precise

regulation of Gαs by cyclic peptides not only appears at the level of nucleotide binding state, but also at the G protein family level. The nucleotide exchange step of Gαi is much less sensitive towards GD20 and GN13 (Figure 2.8D and 2.8E), confirming the class-specificity of both GD20 and GN13 for Gαs (Gαs vs. Gαi).

The crystal structure of GDP-bound Gαs in complex with GD20

GD20 also potently inhibited the long isoform of Gαs, with an IC_{50} of 1.32 ± 0.17 μM (Figure 2.8F), suggesting that GD20 might bind in a similar region compared to GN13. To understand the underlying molecular determinants of how cyclic peptide GD20 favors GDP-bound Gαs and inhibits GDP dissociation. We solved a co-crystal structure of the Gαs/GDP/GD20 complex. The structure was determined by molecular replacement and refined to 1.95 Å (Table 2.3). The overall structure is shown in Figure 5A. Four well-defined water molecules and a number of intramolecular hydrogen bonds constructed a unique helical secondary structure in GD20 (Figure 2.10A-E). One molecule of GD20 binds to the cleft between switch II and the α3 helix of GDP-bound Gαs through electrostatic interactions, hydrogen bonding, and hydrophobic interactions (Figure 2.9B and 2.9C). Specifically, the side chain of residue R6 in GD20 forms a salt bridge with Gαs E268, and this ion pair is further stabilized by Gαs N271; the main chain carbonyl oxygen of F10 in GD20 forms a hydrogen bond network with S275 and N279 from the α3 helix in Gαs; R231 and W234 on Gαs switch II coordinate a complex hydrogen bond network with W8, N11, L12, C13 and D-tyrosine in GD20; deep inside of the GD20 binding pocket, the main chains of I3 and F5 form multiple hydrogen bonds with G225, Q227, and D229 in Gαs (Figure 2.9B). These charge and hydrogen bonding interactions rearrange the flexible Gαs switch II and bury residues F5 and W8 of GD20 inside of a hydrophobic pocket (Figure 2.9C). These

hydrophobic interactions between GD20 and Gαs likely contribute to the high Gαs binding affinity. GD20 binds to GDP-bound Gαs with a K_D value of 31.4 ± 0.7 nM (Figure 2.10F). Single point mutations of GD20, F5A, R6A, and W8A, almost completely abolished Gαs binding, confirming the importance of both polar and hydrophobic interactions mediated by these residues (Figure 2.10G). We performed Gαs alanine scanning mutagenesis at the GD20 binding interface to further validate the hypothesized interactions (Figure 2.10H). Gαs alanine mutations at contact-residues (D229A, R231A, R232A, E268A, N271A, and N279A) eliminated GD20 binding to different extents, however, mutations at non-contact residues (K274A and R280A) did not influence GD20 binding. These mutagenesis studies were in line with our Gαs/GD20 structural model.

Structural basis for the nucleotide state-selectivity and biochemical activity of GD20

GD20 showed high nucleotide state-selectivity in the BLI binding experiment (Figure 2.10I). The high resolution GD20-bound Gαs complex structure elucidated the molecular mechanism by which GD20 distinguishes Gαs inactive state from its active state. We superimposed our GD20-bound Gαs structure to the structure of active GTPγS-bound Gαs (PDB: 1AZT) (Sunahara et al., 1997). The presence of a rigidified switch II in the GTPγS-bound Gαs clashes with GD20 (Figure 2.9D). In particular, R231, R232 and W234 of switch II (shown in space filling) are predicted to create a steric clash with GD20. Indeed, GD20 did not inhibit active state Gαs-mediated AC activation in both biochemical and cell membrane experiments (Figure 2.10J and 2.10K). Next, we compared our GD20-bound Gαs structure with the inactive GDP-bound Gαs structure in complex with Gβγ (chain I in PDB 6EG8) (Liu et al., 2019) (Figure 2.9E). GD20 binding expands the switch II/α3 pocket by repositioning both motifs. However, structural

motifs (such as switch I, III, and the P loop) that are critical for GDP binding remain unchanged with no discernible difference, highlighting the GDP-state selective nature of GD20.

By comparing our GD20/Gαs structure with the Gαs/Gβγ structure, we noticed that GD20 induces a significant conformational shift at the Gβγ binding surface, and GD20 occupies the Gβγ binding surface in a competitive manner (Figure 2.9F and 2.9G). We measured the interaction of GDP-bound Gαs and Gβγ in the presence of GD20 or a Gαs binding deficient analog GD20-F5A using a fluorescence resonance energy transfer (FRET) assay (Figure 2.10L). GD20, but not GD20-F5A, showed potent, dose-dependent inhibition of Gαs/Gβγ interaction, with an IC_{50} of 18.4 ± 2.0 nM (Figure 2.9H).

The GD20-bound Gαs complex structure also demonstrates the molecular basis of GD20 GDI activity (Figure 2.9I). GDP dissociation from Gαs nucleotide binding site requires both conformational changes that weaken the guanine nucleotide affinity and Ras/Helical domain separation that allows GDP release (Dror et al., 2015). GD20 does not engage the GDP exit tunnel, therefore is not directly occluding GDP release. Instead, GD20 phenocopies the effects of Gβγ GDI activity, stabilizing the juxtapositions of switch I, III, and the P loop in the GDP-bound state. Such a conformational lock not only orients Gαs R201 and E50 to directly capture the β-phosphate of GDP, but also inhibits the spontaneously Ras/Helical domain separation by stabilizing two hydrogen bonds between Gαs R201 and N98. As a result, GD20 strongly antagonizes GDP dissociation from Gαs. These data suggested that GD20 selectively captures GDP-bound Gαs, contributing to Gαs GDI activity and Gαs/Gβγ interaction inhibition.

G protein class-specificity of GN13 and GD20

There are four main families of Gα proteins: Gαs, Gαi, Gα12/13, and Gαq. These Gα proteins are structurally similar, yet they transduce divergent GPCR signaling activation through binding to distinct effectors (Syrovatkina., 2017). To assess whether GN13 and GD20 were capable of distinguishing Gαs from other Gα proteins, we measured their binding kinetics to Gαi, Gα13, and Gαq using biolayer interferometry (BLI). In contrast to the binding of GN13 to GNP-bound Gαs (Figure 2.4C), GN13 showed little to no detectable binding to Gα13, Gαq, and Gαi at the highest concentration tested (Figure 2.12A-E), confirming the class-specificity of GN13. Similarly, the potent Gαs/GDP binder GD20 (Figure S5F) showed little to no detectable binding to Gα13, Gαq, and Gαi at the highest concentration tested (Figure 2.12F, 2.12G, and 2.12J). Furthermore, GD20 was at least 100-fold more selective for Gαs than Gαi to disrupt the Gα/Gβγ interaction in a FRET assay (Figure 2.12K). These results demonstrated that both GN13 and GD20 have excellent G protein class-specificity, although we did not include other Gα proteins as a part of the negative selection.

To identify G protein specificity determinants of both cyclic peptides, we performed Gα protein sequence alignment at the cyclic peptide binding interfaces (Figure 2.11B) and compared our structures with structures of other Gα proteins in complex with their effectors or peptide inhibitors (Chen et al., 2008; Taylor et al., 2016; Johnston et al., 2006; Nishimura et al., 2010; Wall et al., 1995) (Figure 2.11C-R).

The GDP-AlF4--bound active states of Gα13, Gαq, and Gαi from their complex structures were superimposed to GNP-bound Gαs in our Gαs/GN13 complex (Figure 2.11C). We found that there were a few profound differences among the Gα proteins. First, the presence of a distinctive π–π stacking between W277 and H357 and a unique R283 in Gαs (the WHR triad) define the

positions of the h3s5 and h4s6 loops, which present the side chain of N279 to form a strong hydrogen bond with the main chain carbonyl oxygen of V5 in GN13 (Figure 2.11D and 2.11H). Mutations of the WHR triad in Gα13 (VKS), Gαq (IKQ), and Gαi (CKT) separate the h3s5 and h4s6 loops, therefore, diminish the interactions with GN13 (Figure 2.11E-G). The replacement of N279 by Y261 in Gαq further limits the interaction between Gαq and GN13 (Figure 2.11H). Second, I8 of GN13 docks into a hydrophobic pocket made of two non-polar residues F238 and L282 from Gαs. The substitution of L282 with a phenylalanine residue in Gα13, Gαq, and Gαi sterically reshape the hydrophobic pocket by forming CH/π interactions with nearby phenylalanine residues (Figure 2.11E-G), which dislocates the correct orientation for GN13 Van der Waals interactions. The same hydrophobic pocket also controls the binding of other Gα effectors (Chen et al., 2005; Tesmer et al., 2005). Next, K274 in Gαs (E273 in Gα13; D251 in Gαi) interacts with the negatively charged side chain of E3 in GN13. Homologous residues in Gα13 and Gαi repel the negative charge of GN13, rendering the lack of GN13 binding. Finally, we noticed that a unique D229 residue (S228 in Gα13; S211 in in Gαq; S206 in Gαi) might participate in a hydrogen bond interaction between GN13 T11 and Gαs R232. However, alanine mutation of the Gαs D229 residue did not influence GN13 binding (Figure S3G), indicating that Gαs D229 is dispensable for GN13 interaction.

We compared our GD20-bound Gαs structure with GDP-bound Gα13, Gαq, and Gαi from their complex structures (Figure 2.11I). The specificity of GD20 is determined by three major contact points which involve electrostatic interactions, Van der Waals interactions, and hydrogen bonding. (1) The α3 helices in Gαs, Gα13, Gαq, and Gαi, have distinct hydrogen bond networks. Gαs N271 precisely orchestrated positioning of E268 to interact with the positively charged side chain of R6 in GD20 (Figure 2.11J). Rewired hydrogen bond networks in other Gα proteins,

however, disfavor the salt bridge formation between Gα and GD20 (Figure 2.11K-M). (2) The WHR triad also orients Gαs for better GD20 binding. Gαs N279 and the α3 helix in Gαs formed water-mediated hydrogen bonds with the main chain carbonyl oxygen of A9 in GD20 (Figure 2.11N). (3) The switch II region is mostly conserved across Gα proteins with several notable differences. The presence of three unique residues (D229, Q236, and N239) and a conserved R231 in Gαs support a helical structure of switch II and form hydrogen bond networks with I3, Q7 and L12 of GD20 (Figure 2.11O). Alanine mutation of the Gαs D229 residue negatively influenced GD20 binding (Figure 2.12H), indicating that Gαs D229 participates in GD20 binding. The dynamic Gαs switch II also shapes a distinctive hydrophobic pocket (L282-F238-I235) for engagement of GD20. Homologous residues in Gα13, Gαq, and Gαi on the switch II adopt different conformations which are not compatible with GD20 binding (Figure 6P-R). In summary, our sequence alignment and structural analysis revealed that some of the Gαs residues directly interacting with GN13 and GD20 are not conserved in other Gα proteins, which explains the outstanding G protein class-specificity of both cyclic peptides.

A cell permeable GD20 analog, cpGD20, is a dual-effect G protein modulator

Receptor coupled G protein signaling releases GTP-bound Gα and free Gβγ to engage their own effectors to transduce downstream signaling. GDP-bound Gα is a functional "OFF" switch by tightly reassociating with the obligate Gβγ dimers and masking the effector binding surfaces on both Gαs and Gβγ (Gulati et al., 2018). A potent Gαs Gβγ protein-protein interaction (PPI) inhibitor should potentially block Gαs Gβγ reassociation and further prolong Gβγ-mediated effector activation (Figure 2.13A). With a potent Gαs Gβγ PPI inhibitor, GD20, functioning in

vitro, we next asked whether GD20 could modulate the heterometric Gs protein complex following receptor stimulation in the cells.

We first tested the cell permeability of GD20, as peptide-based chemical probes often suffer from poor cell permeability. Several G protein-specific linear peptides exhibit in vitro activities but have no reported cellular efficacy, likely due to their low cell permeability (Ja and Roberts, 2004; Johnston et al., 2005; Johnston et al., 2005; Johnston et al., 2006; Austin et al., 2008). The carboxyl terminus of GD20 (G15) was conjugated with a chloroalkane tag to make ct-GD20 (Figure 2.14A). While ct-GD20 is cell permeable, a single amino acid substitution F10L significantly improved cell penetration (Figure 2.13B, see also Figure 2.14B and 2.14C). cpGD20 (GD20-F10L) retains a similar level of binding affinity for GDP-bound Gαs with a K_D value of 14.5 ± 0.4 nM (Figure 2.14D), and comparable biochemical activity, state-selectivity, and class-specificity (Figure 2.14E, and 2.12H-J). cpGD20 disrupted the Gαs/Gβγ interaction with an IC_{50} of 14.0 ± 0.6 nM and exhibited a near 100-fold selectivity over Gαi (Figure 2.12L).

cpGD20 did not inhibit Gαs-mediated cAMP production in live HEK293 cells, confirming its nucleotide-state-selectivity (Figure 2.14F). We tested whether cpGD20 could inhibit Gαs/Gβγ interaction in HEK293 cells overexpressing both β2AR and Gαs/Gβγ. Rluc8 was inserted within a flexible loop region between the αB-αC helices of Gα (Figure 2.14G) and GFP2 was inserted at the N-terminus of Gγ2 to capture Gαβγ heterotrimer interaction. A decrease in the bioluminescence resonance energy transfer (BRET2) signal between labeled G protein subunits can detect Gαβγ dissociation in live cells (Olsen et al., 2020) (Figure 2.14H). We examined Gαβγ trimer dissociation elicited by the GPCR agonist at various concentrations of cyclic peptides by monitoring the net BRET2 signal. In cells that were transiently transfected with β2AR, GαsShort_Rluc8, Gβ1, and Gγ-GFP2, ISO application stimulated a basal net BRET response.

Pretreatment with cpGD20 induced a greater net BRET2 signal between Gαs and Gβγ (Figure 2.13C, see also Figure 2.14I). In comparison, the Gαs binding deficient mutant cpGD20-F5A failed to induce a larger BRET2 response (Figure 2.13C). To assess the specificity of cpGD20 at the G protein level, we tested it against the Gαi/Gβγ interaction. HEK293 cells transiently expressing Gαi-coupled muscarinic acetylcholine receptor M2 (M2R), Gαi1_Rluc8, Gβ1, and Gγ-GFP2 were challenged with M2R agonist, acetylcholine. Pretreatment with cpGD20 did not induce a net BRET2 signal change between Gαi and Gβγ (Figure 2.13D). These data suggested that cpGD20 can specifically capture monomeric Gαs after G protein activation and interfere with Gαs/Gβγ reassociation.

We next investigated whether cpGD20 could prolong Gβγ-mediated effector activation after Gαs/Gβγ dissociation. We focused on a well-studied Gβγ effector: G protein-activated inward rectifier K^+ (GIRK) channel, which produces inward K^+ current upon Gβγ binding. It was known that when the stimulatory G protein trimer is overexpressed, GIRK channels can be activated by Gβγ upon ISO-stimulated β2AR activation (Touhara and MacKinnon, 2018). Indeed, voltage-clamp experiments on HEK293 cells transiently transfected with β2AR, overexpressed Gαs, Gβγ, and GIRK4 showed GIRK activation in response to ISO stimulation (Black curve in Figure 2.13E). Treatment with either cyclic peptides or DMSO did not attenuate the amplitude of GIRK activation (Figure 2.13E and 2.13G). However, cpGD20, but not cpGD20-F5A or DMSO control, significantly delayed GIRK channel deactivation after ISO washout (Figure 2.13E and 2.13F). These results suggested that the cell-permeable Gαs-specific inactive state inhibitor, cpGD20, acts as a dual-effector G protein modulator, liberating Gαs-bound Gβγ while sequestering GDP-bound Gαs.

Discussion

GPCRs and G proteins comprise the largest family of signal transducing proteins in the human genome. Although approximately 35% of approved drugs target GPCRs, directly targeting the downstream integrator G proteins has the potential for broader efficacy via blocking convergent pathways shared by multiple GPCRs (Bonacci et al., 2006; Gulati et al., 2018). However, there is a striking absence of drug-like chemical matter that specifically targets the Gα proteins in cells. Cyclic peptides bridge the chemical space between small molecules and biologics, and are therefore capable of recognizing shallow effector binding pockets at PPI interfaces while maintaining optimal pharmacological properties. This is demonstrated here by the development of Gαs selective cyclic peptide inhibitors GN13 and GD20, which specifically recognize the Gαs switch II/α3 pocket, the site where downstream effectors bind. Cyclization of the peptide sequence and introduction of a non-canonical amino acid (D-tyrosine) provide these Gαs inhibitors better cell permeability and chemical stability (Figure 2.13B, see also Figure 2.4I, Table 2.5 and 2.6), making them comparable to small molecule drugs. Moreover, in contrast to the complex cyclic peptide natural product YM-254890, our Gαs-binding cyclic peptides can be easily derivatized through side-chain substitutions. The high-resolution co-crystal structures that we obtained of Gαs with our cyclic peptides enable us to program the protein-inhibitor interaction for desired biological effects. This tunability is exemplified by two GD20 analogs, cpGD20 (GD20-F10L) and GD20-F5A, in which a single point substitution drastically changed the biochemical and pharmacological properties of a given cyclic peptide, providing opportunities for further optimization.

Gαs is one of the most frequently mutated G proteins in human cancer. Hotspot mutations in Gαs (Q227 and R201) lock Gαs in a constitutively active conformation (Zachary et al., 1990;

Hu and Shokat, 2018). We found that the cyclic peptide GN13, but not GD20, recognized this particular Gαs conformation and inhibited all the tested Gαs oncogenic mutants (Q227L, R201C, R201H, and R201S) in the AC activation assay (Figure 2.6J and 2.10J). To our knowledge, this is the first demonstration of the ligandability of oncogenic Gαs. Moreover, the cell permeable cpGN13 has opened up potential to uncover molecular mechanism of tumorigenic Gαs signaling.

Both GN13 and GD20 bind at the switch II/α3 pocket in Gαs. This pocket is evolutionally conserved and is commonly used for effector binding, with subtle differences conferred by sequence variability between homologous Gα proteins and by binding of different nucleotides (Wall et al., 1995; Tesmer et al., 1997; Slep et al., 2001; Tesmer et al., 2005; Chen et al., 2005; Liu et al., 2019). Our extremely diverse chemical library along with both positive and negative selection enabled us to survey the sequence space of cyclic peptides and discover selective binders that capture specific, subtly different conformations of the switch II/α3 pocket. The resulting Gαs-cyclic peptide interactions are highly class-specific and state-selective, allowing for precise detection of particular Gαs nucleotide binding states. This molecular recognition could be useful for developing biosensors that directly probe Gαs/GTP or Gαs/GDP in cells, which is complementary to Gαs nanobody sensors that only capture the guanine-nucleotide-free form of Gαs (Manglik et al., 2017). For example, a fluorescently tagged cpGD20 could potentially be used for tracking real-time translocation of endogenous Gαs following receptor activation and internalization, which bypasses the need of G protein overexpression or genetic modification (Maziarz et al., 2020; Olsen et al., 2020).

Pharmacological interrogation of GPCR-mediated signaling events has been largely limited to the receptors. The cell permeable cyclic peptides cpGN13 and cpGD20 offer an

opportunity to directly probe the Gαs/Gβγ trimer at the G protein level and exemplify a new mode of pharmacological intervention in stimulatory GPCR signaling.

The active state inhibitor, cpGN13 directly competes Gαs from binding to its effector, AC. As a result, short-term pretreatment with cpGN13 significantly inhibited β2AR mediated second messenger stimulation in live HEK293 cells (Figure 2.3H). In comparison, treatment with the previously used Gαs protein regulator, cholera toxin catalyzes Gαs ADP-ribosylation, which leads to transient Gαs activation and subsequent Gαs protein degradation (Chang and Bourne, 1989). cpGN13 provides a distinct mechanism for inhibiting the active state of Gαs, bypassing the prerequisite activation and degradation.

The inactive state inhibitor, cpGD20 provides a new tool to study the role of Gβγ signaling during GPCR stimulation. Gαs-cpGD20 interaction sterically occludes Gβγ binding to Gαs. After acute stimulation of a Gαs-coupled receptor (β2AR), cpGD20 functions as a dual-effect G protein PPI inhibitor by sequestering monomeric Gαs and releasing Gβγ from the natural inhibition of Gαs/GDP. As a result, cpGD20 co-treatment with the β2AR agonist, ISO maintains a higher Gβγ concentration after GPCR activation, which is comparable to the Gβγ concentration following M2R (a Gαi-coupled receptor) activation (Figure 2.13C and 2.13D). The increased amount of free Gβγ continues to signal and extend the lifetime of the Gβγ-dependent receptor activation (Figure 2.13E-F). Therefore, cpGD20 could potentially provide a novel approach to elucidate or even rewire the downstream signaling of Gαs-coupled receptors via activating Gβγ dependent pathways. Moreover, rapid Gα Gβγ reassociation terminates canonical GPCR-dependent G protein signaling within seconds (Ghosh et al., 2017). However, the slow dissociating Gαs/GD20-F10L interaction (Figure 2.14D and Table 2.4) offers the opportunity to trap the inactive state Gαs for a longer time and consequently lengthen one branch of GPCR signaling — the Gβγ heterodimer.

Our demonstration of the use of the RaPID cyclic peptide platform through both positive and negative selection steps provides proof of principle for a path to discovering other cell-permeable, class-specific and state-selective inhibitors of the remainder of the GTPase family. The state-selective Gαs inhibitors GN13 and GD20 provide novel pharmacological strategies for understanding and modulating GPCR signaling.

Limitations of the study

Although GN13, GD20 and their analogs are strong binders to Gαs, with KD values in the nanomolar range, their potencies are compromised in cell experiments. This is likely due to the difficulty of competing tight protein-protein interactions on cell membranes and the relatively lower cell penetration of cyclic peptides. Optimizing cyclic peptides with non-canonical residues could potentially further improve the potency and cell permeability of cpGN13 and cpGD20 to overcome this limitation. Second, we purified Gα13, Gαq, and Gαi1 from three other Gα families as examples to confirm the G protein class-specificity of both GN13 and GD20, we have not performed binding experiments with the entire Gα protein family (e.g., Gαolf, Gα11, G12, and others). It will be of interest in the future to test the specificity of GN13 and GD20 against other Gα proteins. Last, we investigated the cellular activities of cpGN13 and cpGD20 with two well-studied GPCRs, β2AR and M2R, and one well-studied Gβγ effector, GIRK4. Both cell-penetrating cyclic peptides showed great efficacy in the β2AR and GIRK4 systems, but it would be worthwhile to test more Gαs-coupled receptors and Gβγ effectors with cpGN13 and cpGD20 to further explore the scope of their utility.

Materials and Methods

Cell lines

HeLa cells stably expressing the Halo-Tag-GFP-Mito construct were provided by the Kritzer lab (Peraro et al., 2018). HEK293 cells used for cADDis were from ATCC (CRL-1573), and were cultured at 37 °C, 5% CO_2 in DMEM (Thermo Fisher Scientific, Cat#11965118) supplemented with 10% heat-inactivated FBS (HyClone, cat# SH30910.03c). In all other cell-based assays, wild-type HEK293, GNAS KO HEK293 were provided by the Inoue lab. Wild-type HEK293, GNAS KO HEK293 and HeLa cells were cultured at 37 °C, 5% CO_2 in DMEM (Thermo Fisher Scientific, Cat# 11995073) supplemented with 10% heat-inactivated FBS (AxeniaBiologix). All the cells are female in origin.

WT Gαs, all the mutants of Gαs, the C1 domain (residues 442-658, VC1) of human ADCY5 (adenylyl cyclase V) and the C2 domain (residues 871-1082, IIC2) of human ADCY2 (adenylyl cyclase II) were overexpressed in *Escherichia coli* BL21(DE3) cultured in Terrific Broth (TB) Medium. Human GNB1 (Gβ1) and GNG2 (Gγ2) were co-expressed in Sf9 insect cells cultured in Sf-900 III SFM medium at 28 °C. Human GNB1 (Gβ1) and GNG2 (Gγ2) were co-expressed in Sf9 insect cells cultured in Sf-900 III SFM medium at 28 °C. Human Gα(i/13) was expressed in Sf9 insect cells cultured in Sf-900 III SFM medium at 28 °C.

Protein expression and purification

(1) Proteins used in the AC assay, the radioactivity assay, and the steady-state GTPase assay

The wild-type, S275L, R201C, R201H, R201S, Q227L, D229A, R231A, R232A, E268A, N271A, K274A, N279A, and R280A mutants of Gαs, C2 domain of human ADCY2, C1 domain of human ADCY5, and human Gβ1/Gγ2(C68S) complex used in the AC activity assay were

cloned, expressed and purified as described (Hu and Shokat, 2018). All the non-WT Gαs plasmids were constructed using Gibson assembly from the WT Gαs plasmid. Gαs used in the RaPID selection The gene encoding residues 7-380 of the short isoform of human Gαs (GNAS, accession number in PubMed: NP_536351) with an Avi tag and a TEV cleavage site at its N-terminus was cloned into the multiple cloning site 1 of the pETDuet vector. The resulting protein sequence is as follows:

MGSSHHHHHHSGMSGLNDIFEAQKIEWHESSGENLYFQGMSKTEDQRNEEKAQREAN
KKIEKQLQKDKQVYRATHRLLLLGAGESGKSTIVKQMRILHVNGFNGDSEKATKVQDI
KNNLKEAIETIVAAMSNLVPPVELANPENQFRVDYILSVMNVPDFDFPPEFYEHAKALW
EDEGVRACYERSNEYQLIDCAQYFLDKIDVIKQADYVPSDQDLLRCRVLTSGIFETKFQV
DKVNFHMFDVGGQRDERRKWIQCFNDVTAIIFVVASSSYNMVIREDNQTNRLQEALNL
FKSIWNNRWLRTISVILFLNKQDLLAEKVLAGKSKIEDYFPEFARYTTPEDATPEPGEDPR
VTRAKYFIRDEFLRISTASGDGRHYCYPHFTCAVDTENIRRVFNDCRDIIQRMHLRQYEL
L

In the same pETDuet plasmid, the gene encoding BirA (accession number in PubMed: NP_418404.1) was inserted between NdeI and XhoI sites of the multiple cloning site 2. This plasmid was transformed into *Escherichia coli* BL21(DE3). The transformed cells were grown in TB medium supplemented with 50 μg/mL carbenicillin at 37 °C until OD600 reached 0.5, and then cooled to 22 °C followed by addition of 40 μM β-D-thiogalactopyranoside. After overnight incubation, 50 μM biotin was added into the culture for 2 hours. The cells were harvested by centrifugation, resuspended in lysis buffer (150 mM NaCl, 25 mM Tris 8.0, 1 mM $MgCl_2$, 250 μM biotin, protease inhibitor, and then lysed by a microfluidizer. The cell lysate was centrifuged at 14000 g for 1 hour at 4 °C. The supernatant was incubated with TALON Resin at 4 °C for 2 hours,

then the resin was washed by 500 mM NaCl, 25 mM Tris 8.0, 1 mM MgCl2 and 5 mM imidazole 8.0. Gαs was eluted by 25 mM Tris 8.0, 1 mM MgCl2, 250 mM imidazole 8.0, 10% glycerol and 0.1 mM GDP. After adding 5 mM Dithiothreitol (DTT), the eluate was loaded onto a Source-15Q column. Gαs was eluted by a linear gradient from 100% IEC buffer A (25 mM Tris 8.0, 1 mM MgCl2) to 40% IEC Buffer B (25 mM Tris 8.0, 1 M NaCl, 1 mM MgCl2). The peak fractions were pooled and supplemented with 5 mM DTT. One half of peak fractions was mixed with equal volume of GNP exchange buffer (150 mM NaCl, 25 mM HEPES 8.0, 2 mM EDTA, 2 mM GNP, 5 mM DTT) for 2 hours, followed by addition of 5 mM $MgCl_2$. GNP-bound Gαs and GDP-bound Gαs were concentrated and purified by gel filtration (Superdex 200 increase, 10/30) with SEC buffer (150 mM NaCl, 20 mM HEPES 8.0, 5 mM $MgCl_2$ and 1 mM EDTA-Na 8.0). The peak fractions were pooled and concentrated for biochemical assay.

(2) WT Gαs, Gαs S275L mutant and full-length Gαi used in the TR-FRET assay and the bio-layer interferometry assay

The gene of residues 7-380 of the short isoform of human Gαs (GNAS, accession number in PubMed: NP_536351) with a stop codon at its end was cloned into the NdeI/XhoI site of a modified pET15b vector, in which a Drice cleavage site (AspGluValAsp↓Ala) and an Avi tag were inserted at the N-terminus. The resulting protein sequence after Drice protease cleavage is as follows:

AHMGLNDIFEAQKIEWHESKTEDQRNEEKAQREANKKIEKQLQKDKQVYRATHRLLLL
GAGESGKSTIVKQMRILHVNGFNGDSEKATKVQDIKNNLKEAIETIVAAMSNLVPPVEL
ANPENQFRVDYILSVMNVPDFDFPPEFYEHAKALWEDEGVRACYERSNEYQLIDCAQY
FLDKIDVIKQADYVPSDQDLLRCRVLTSGIFETKFQVDKVNFHMFDVGGQRDERRKWIQ

CFNDVTAIIFVVASSSYNMVIREDNQTNRLQEALNLFKSIWNNRWLRTISVILFLNKQDL
LAEKVLAGKSKIEDYFPEFARYTTPEDATPEPGEDPRVTRAKYFIRDEFLRISTASGDGRH
YCYPHFTCAVDTENIRRVFNDCRDIIQRMHLRQYELL

The AviTagged Gαs S275L mutant plasmid was constructed using quick-change mutagenesis from the AviTagged WT Gαs plasmid. The resulting protein sequence after Drice protease cleavage is as follows:

AHMGLNDIFEAQKIEWHESKTEDQRNEEKAQREANKKIEKQLQKDKQVYRATHRLLLL
GAGESGKSTIVKQMRILHVNGFNGDSEKATKVQDIKNNLKEAIETIVAAMSNLVPPVEL
ANPENQFRVDYILSVMNVPDFDFPPEFYEHAKALWEDEGVRACYERSNEYQLIDCAQY
FLDKIDVIKQADYVPSDQDLLRCRVLTSGIFETKFQVDKVNFHMFDVGGQRDERRKWIQ
CFNDVTAIIFVVASSSYNMVIREDNQTNRLQEALNLFKLIWNNRWLRTISVILFLNKQDL
LAEKVLAGKSKIEDYFPEFARYTTPEDATPEPGEDPRVTRAKYFIRDEFLRISTASGDGRH
YCYPHFTCAVDTENIRRVFNDCRDIIQRMHLRQYELL

The gene of residues 2-354 of human Gαi1 (GNAI1, accession number in PubMed: NP_002060.4) with a stop codon at its end was cloned into the NdeI/XhoI site of a modified pET15b vector, in which a Drice cleavage site (AspGluValAsp↓Ala) and an Avi tag were inserted at the N-terminus. The resulting protein sequence after Drice protease cleavage is as follows:

AHMGLNDIFEAQKIEWHEGCTLSAEDKAAVERSKMIDRNLREDGEKAAREVKLLLLGA
GESGKSTIVKQMKIIHEAGYSEEECKQYKAVVYSNTIQSIIAIIRAMGRLKIDFGDSARAD
DARQLFVLAGAAEEGFMTAELAGVIKRLWKDSGVQACFNRSREYQLNDSAAYYLNDL
DRIAQPNYIPTQQDVLRTRVKTTGIVETHFTFKDLHFKMFDVGGQRSERKKWIHCFEGV
TAIIFCVALSDYDLVLAEDEEMNRMHESMKLFDSICNNKWFTDTSIILFLNKKDLFEEKIK

KSPLTICYPEYAGSNTYEEAAAYIQCQFEDLNKRKDTKEIYTHFTCATDTKNVQFVFDA
VTDVIIKNNLKDCGLF

The above-mentioned plasmids were transformed into *Escherichia coli* BL21(DE3), respectively. The transformed cells were grown in TB medium supplemented with 50 μg/mL carbenicillin at 37 °C until OD600 reached 0.4, and then cooled to 22 °C followed by addition of 100 μM IPTG. After overnight incubation, the cells were harvested by centrifugation, resuspended in lysis buffer (150 mM NaCl, 25 mM Tris 8.0, 1 mM $MgCl_2$, protease inhibitor cocktail), and then lysed by a microfluidizer. The cell lysate was centrifuged at 14000 g for 1 hour at 4 °C. The supernatant was incubated with TALON resin at 4 °C for 1 hour, then the resin was washed by 500 mM NaCl, 25 mM Tris 8.0, 1 mM $MgCl_2$ and 5 mM imidazole 8.0. G protein was eluted by 25 mM Tris 8.0, 1 mM $MgCl_2$, 250 mM imidazole 8.0, 10% glycerol and 0.1 mM GDP. After adding 5 mM Dithiothreitol (DTT), the eluate was incubated with Drice protease at 4 °C overnight to remove the hexahistidine tag. Purified BirA (A gift from the Wells lab) and biotin were added at 4 °C until LC-MS showed complete biotinylation. G protein was loaded onto a Source-15Q column and eluted by a linear gradient from 100% IEC buffer A (25 mM Tris 8.0, 1 mM $MgCl_2$) to 40% IEC Buffer B (25 mM Tris 8.0, 1 M NaCl, 1 mM $MgCl_2$). The peak fractions were pooled, nucleotide exchanged, and supplemented with 5 mM DTT and 0.1 mM nucleotide, and then concentrated and purified by gel filtration (Superdex 200 increase, 10/30) with SEC buffer (150 mM NaCl, 20 mM HEPES 8.0, 5 mM $MgCl_2$ and 1 mM EDTA-Na 8.0). The peak fractions were pooled and concentrated for biochemical assay.

(3) WT Gα(i/13) used in the bio-layer interferometry assay

The gene of residues 1-28 of human Gαi1 (GNAI1, accession number in PubMed: NP_002060.4) and the gene of residues 47-377 of human Gα13 (GNA13, accession number in PubMed: NP_006563.2) with a stop codon at its end was cloned into the pFastBacHTA vector, in which a Drice cleavage site (AspGluValAsp↓Ala) and an Avi tag were inserted at the N-terminus. The resulting protein sequence after Drice protease cleavage is as follows: AHMGLNDIFEAQKIEWHEMGCTLSAEDKAAVERSKMIDRNLREDGERSARLVKILLLG AGESGKSTFLKQMRIIHGQDFDQRAREEFRPTIYSNVIKGMRVLVDAREKLHIPWGDNS NQQHGDKMMSFDTRAPMAAQGMVETRVFLQYLPAIRALWADSGIQNAYDRRREFQLG ESVKYFLDNLDKLGEPDYIPSQQDILLARRPTKGIHEYDFEIKNVPFKMVDVGGQRSERK RWFECFDSVTSILFLVSSSEFDQVLMEDRLTNRLTESLNIFETIVNNRVFSNVSIILFLNKT DLLEEKVQIVSIKDYFLEFEGDPHCLRDVQKFLVECFRNKRRDQQQKPLYHHFTTAINTE NIRLVFRDVKDTILHDNLKQLMLQ

Amplified Gα(i/13) baculovirus stock was generated using the above-mentioned plasmid in Sf9 insect cells. Avi tagged Gα(i/13) was expressed and purified as described (Kreutz et al., 2006).

RaPID Selection

Selections were performed with thioether-macrocyclic peptide library against biotinylated Gαs. Thioether-macrocyclic peptide libraries were constructed with N-chloroacetyl-D-tyrosine (ClAcDTyr) as an initiator by using the flexible in vitro translation (FIT) system (Goto et al., 2011). The mRNA libraries, ClAcDTyr-tRNAfMetCAU were prepared as reported (Yamagishi et al., 2011). The mRNA library corresponding for the thioether-macrocyclic peptide library was

designed to have an AUG initiator codon to incorporate N-chloroacetyl-D-tyrosine (ClAcDTyr), followed by 8–12 NNK random codons (N = G, C, A or U; K = G or U) to code random proteinogenic amino acids, and then a fixed downstream UGC codon to assign Cys. After in vitro translation, a thioether bond formed spontaneously between the N-terminal ClAc group of the initiator DTyr residue and the sulfhydryl group of a downstream Cys residue.

In the first round of selection, the initial cyclic peptide library was formed by adding puromycin ligated mRNA library (225 pmol) to a 150 μL scale flexible in vitro translation system, in the presence of 30 μM of ClAcDTyr-tRNAfMetCAU. The translation was performed 37 °C for 30 min, followed by an extra incubation at 25 °C for 12 min. After an addition of 15 μL of 200 mM EDTA (pH 8.0) solution, the reaction solution was incubated at 37 °C for 30 min to facilitate cyclization. Then the library was reversed transcribed by M-MLV reverse transcriptase at 42 °C for 1 hour and subject to pre-washed Sephadex G-25 columns to remove salts. The desalted solution of peptide–mRNA/cDNA was applied to Gαs (positive selection state)-immobilized Dynabeads M280 streptavidin magnetic beads and rotated at 4 °C for 1 hour in selection buffer (25 mM HEPES pH 7.5, 150 mM NaCl, 1 mM $MgCl_2$ and 0.05% Tween 20) containing 0.5 mM corresponding nucleotide and 0.1% acetylated BSA. Bead amounts were chosen that the final concentration of Gαs protein was 200 nM. This process is referred to as positive selection. The selected peptide–mRNA/cDNAs were isolated from the beads by incubating in 1xPCR reaction buffer heated at 95 °C for 5 min. The amount of eluted cDNAs was measured by quantitative PCR. The remaining cDNAs were amplified by PCR, purified and transcribed into mRNAs as a library for the next round of selection.

In the subsequent rounds of selection, ligated mRNA from previous round (7.5 pmol) was added to a 5 μL scale reprogrammed in vitro translation system. This was incubated at 37 °C for

30 min and at 25 °C for 12 min. Then 1 μL of 100 mM EDTA (pH 8.0) was added and incubated at 37 °C for 30 min. After reverse transcription and subject to pre-washed Sephadex G-25 columns to remove salts, negative selection was performed by adding the desalted solution of peptide–mRNA/cDNA to Gαs (negative selection state)-immobilized Dynabeads M280 streptavidin magnetic beads and rotated at 4 °C for 30 min in selection buffer containing 0.1% acetylated BSA. This process was repeated several times by removing the supernatant to fresh beads immobilized with Gαs (negative selection state). The supernatant from the last negative selection was then added to beads immobilized with the positive selection state of Gαs (final conc. 200nM) and rotated at 4 °C for 30 min in selection buffer containing 0.5mM corresponding nucleotide and 0.1% acetylated BSA. As described in the first round of selection, the cDNA was quantified with qPCR, amplified with PCR, transcribed and ligated to puromycin. The subsequent selection was repeated for several rounds until a significant enrichment of cDNA was observed for positive selection state. The recovered cDNA was then identified by next generation sequencing (Miseq, Illumina).

Comparison selection

In comparison selection, ligated mRNA (7.5 pmol) from last round selection was added to a 5 μL scale reprogrammed in vitro translation system. After translation, cyclization, reverse transcription and prewashed with Sephadex G-25 columns, the desalted solution of peptide–mRNA/cDNA library was split equally into three fractions, and perform three paralleled selections with the same amount of blank, GDP-bound Gαs-immobilized or GNP-bound Gαs-immobilized Dynabeads M280 streptavidin magnetic beads, individually. For each of the paralleled selections, the beads were rotate at 4 °C for 30 min, washed three times with selection buffer. The remaining

cDNAs were then eluted from the beads, quantified by qPCR, followed by Miseq sequencing. Finally, identified sequences from each paralleled selection were compared by normalization of Miseq abundance of the sequence with the qPCR reads of the paralleled selection.

Bio-layer interferometry (BLI)

BLI experiments were performed using an OctetRED384 instrument from ForteBio. All experiments were performed at 25 °C using BLI buffer (10 mM HEPES pH 7.4, 150 mM NaCl, 1mM $MgCl_2$, 0.05% Tween-20, 0.1% DMSO, 0.2 mM GNP or GDP). Cyclic peptides or Gα proteins were diluted to a series of concentrations (Final concentrations were indicated in Figures) in BLI buffer plus 10 μM Biotin. Assays were conducted in Greiner 384well, black, flat bottom polypropylene plates containing the protein solutions, BLI buffer plus 10 μM Biotin for dissociation, and serial dilutions of cyclic peptides to be tested.

Biotinylated proteins or cyclic peptides were immobilized on Streptavidin biosensors by dipping sensors into plate wells containing protein solutions at a concentration of 50 - 150 nM. Protein loading is around 2-3 nm. Cyclic peptide loading is around 0.2-0.3 nm. Sensors loaded with proteins or cyclic peptides were moved and dipped into wells with BLI buffer plus 10 μM Biotin to block unlabeled Streptavidin. Association–dissociation cycles of compounds were started by moving and dipping sensors to cyclic peptides dilutions and BLI buffer plus 10 μM Biotin wells alternatively. Association and dissociation times were indicated in the figure legend.

Raw kinetic data collected were processed with the Data Analysis software provided by the manufacturer using single reference subtraction in which buffer-only reference was subtracted (For GN13 analysis). Because GD20 analogs have a low level of background binding, we used a double reference subtraction (buffer-only reference and non-protein-loading reference) method to

calculate their kinetics values. The resulting data were analyzed based on a 1:1 binding model from which k_{on} and k_{off} values were obtained and then K_d values were calculated.

Adenylyl cyclase activity assay

(1) Cyclic peptides dose dependent inhibition

Cyclic peptides (4 mM stock in DMSO) were diluted to 4X stocks with a series of concentrations in reaction buffer (1x PBS 7.4, 0.1% BSA). WT Gαs at a concentration of 8.5 mg/mL (about 190 μM) in 20 mM HEPES 8.0, 150 mM NaCl, 5 mM $MgCl_2$, 1 mM EDTA-Na 8.0 was diluted to 0.5 μM in dilution buffer (1x PBS 7.4, 0.1% BSA, 1 mM EDTA-Na 8.0, 2 mM DTT, 0.1mM $MgCl_2$) plus 1mM GNP. After incubation at room temperature for 1 hour to allow nucleotide exchange, 2.5 μL of 4x Gαs dilution was mixed with 1 μL MgCl2 stock (20 mM $MgCl_2$, 1x PBS 7.4, 0.1% BSA) in an OptiPlate-384, White Opaque 384-well Microplate to lock Gαs in GNP-bound state. 2 μL of 5x AC stock (2 μM VC1, 2 nM IIC2, 150 μM FSK, 1x PBS 7.4, 0.1% BSA) was added, followed by addition of 2.5 μL 4X cyclic peptides stock. Reaction mixture was further incubated at room temperature for 2 hours and placed on ice for 5 minutes. cAMP production was initiated by addition of 2 μL of ATP stock (1 mM ATP, 1x PBS 7.4, 0.1% BSA). The reaction was carried out at 30 °C for 10 minutes in a PCR machine and stopped by heating at 95 °C for 3 minutes. The cAMP concentrations were measured by the LANCE Ultra cAMP kit. Final [cyclic peptide]: 0, 0.39, 0.78, 1.56, 3.12, 6.25, 12.5, 25 μM; Final [Gαs]: 125 nM; Final [VC1]: 400 nM; Final [IIC2]: 0.4 nM; Final [FSK]: 30 μM; Final [ATP]: 200 μM.

(2) GN13 inhibition of Gαs proteins at various concentrations

WT Gαs and S275L mutant at a concentration of 8.5 mg/mL (about 190 μM) in 20 mM HEPES 8.0, 150 mM NaCl, 5 mM $MgCl_2$, 1 mM EDTA-Na 8.0 were diluted to a series of concentrations in dilution buffer (1x PBS 7.4, 0.1% BSA, 1 mM EDTA-Na 8.0, 2 mM DTT, 0.1mM $MgCl_2$) plus 1mM GNP. After incubation at room temperature for 1 hour to allow nucleotide exchange, 2.5 μL of 4x each sample was then mixed with 1μL of $MgCl_2$ stock (20 mM MgCl2, 1x PBS 7.4, 0.1% BSA) in an OptiPlate-384, White Opaque 384-well Microplate. 2 μL of AC/Gβγ 5x stock (2 μM VC1, 2 nM IIC2, 150 μM FSK, 1x PBS 7.4, 0.1% BSA, 10 μM Gβ1/γ2(C68S)) was added, followed by addition of 2.5 μL 25 μM GN13 4x stock in 1x PBS 7.4, 0.1% BSA. Reaction mixture was further incubated at room temperature for 2 hours and placed on ice for 5 minutes. cAMP production was initiated by addition of 2 μL of ATP stock (1 mM ATP, 1x PBS 7.4, 0.1% BSA). The reaction was carried out at 30 °C for 10 minutes in a PCR machine and stopped by heating at 95 °C for 3 minutes. The cAMP concentrations were measured by the LANCE Ultra cAMP kit. Final [cyclic peptide]: 6.25 μM; Final [Gαs]: 0, 1.37, 4.12, 12.3, 37.0, 111, 333,1000 nM; Final [VC1]: 400 nM; Final [IIC2]: 0.4 nM; Final [FSK]: 30 μM; Final [Gβ1/γ2(C68S)]: 2 μM; Final [ATP]: 200 μM.

(3) GN13 inhibition of Gαs proteins in HEK293 cell membranes

Cell membrane preparation: HEK293cells, *GNAS* KO HEK293 cells were plated two day before transfection at a density of 1M cells per 10cm plate. One plate of *GNAS* KO HEK293 cells was transfected with 4 μg of *GNAS* WT or *GNAS* S275L plasmids. After overnight transfection, cells were lifted with TypLE, washed, resuspended in stimulation buffer (1X PBS, protease inhibitor cocktail, 5 mM $MgCl_2$). Cell membranes were disrupted by using the Dounce homogenizer for 25 strokes. Nuclei and unbroken cells were removed by centrifugation for 5 min

at 500 g. The supernatant suspension was carefully removed and centrifuged for 30 min at 45K g. Cell membranes were suspended in stimulation buffer. The protein concentrations were measured using BCA, and were normalized to 750 μg/mL with stimulation buffer. A final concentration of 0.1% BSA was added into the cell membrane suspension. b: AC activity assay in cell membranes: 600 μL of cell membrane suspension was mixed with 60 μL of GTP/GDP 20x stock (stock concentration: 10 mM/1 mM). 5.5 μL of the mixture from last step was mixed with 2.5 μL of GN13 4x stocks and incubated at room temperature. After 2 hours, membrane/cyclic peptide mixture was transferred on ice for 5 minutes, followed by the addition of 2 μL of IBMX/ISO/ATP or IBMX/DMSO/ATP 5x stock (5 mM IBMX, 0.2 mM ISO or DMSO, 2.5 mM ATP in stimulation buffer with 0.1% BSA). The reaction was carried out at 30 °C for 30 minutes in a PCR machine and stopped by heating at 95 °C for 3 minutes. The cAMP concentrations were measured by the LANCE Ultra cAMP kit. Final [cyclic peptide]: 0, 0.78, 1.56, 3.12, 6.25, 12.5, 25, 50 μM; Final [membrane]: 375 μg/mL; Final [IBMX]: 1 mM; Final [ISO]: 40 μM; Final [ATP]: 500 μM; Final [GTP]: 500 μM; Final [GDP]: 50 μM.

(4) cAMP concentrations measurement by the LANCE Ultra cAMP kit

A cAMP standard curve was generated in the same plate using the 50 μM cAMP standard in the kit. Before the measurement, the samples were diluted by stimulation buffer (1x PBS 7.4, 0.1% BSA) to 1/60, 1/120, 1/240 or 1/480 to make sure the cAMP concentrations were in the dynamic range of the cAMP standard curve. 10 μL of each diluted sample was mixed with 5 μL of 4X Eu-cAMP tracer and 5 μL of 4X ULight-anti-cAMP in a white, opaque Optiplate-384 microplate, incubated for 1 hour at room temperature, and the time-resolved fluorescence resonance energy transfer (TR-FRET) signals were read on a Spark 20M plate reader. The cAMP

standard curve was fitted by the software GraphPad Prism using the following equation in which ‘‘Y’’ is the TR-FRET signal and ‘‘X’’ is the log of cAMP standard concentration (M):

Y = Bottom + (Top-Bottom)/(1 + 10^ ((LogIC50-X)* HillSlope))

After obtained the values of the four parameters ‘‘Bottom’’, ‘‘Top’’, ‘‘LogIC50’’ and ‘‘HillSlope’’, we used this equation to convert the TR-FRET signals of the samples into cAMP production values. The cyclic peptides dose dependent inhibition curves were fitted by the following equation to calculate the IC50 of each cyclic peptide:

Y = Bottom + (Top-Bottom)/(1 + 10^ ((LogIC50-X)* HillSlope)), in which ‘‘Y’’ is the cAMP production value, ‘‘X’’ is the log of cyclic peptide concentration (M).

FRET based Gαs/adenylyl cyclase interaction assay

Cyclic peptides GN13 and others (4 mM stock in DMSO) were diluted to 5X stocks with a series of concentrations (0, 0.0034, 0.0102, 0.0305, 0.0914, 0.274, 0.823, 2.47, 7.41, 22.2, 66.7, 200 μM) in assay buffer (1X PBS 7.4, 0.1% BSA, 2 mM DTT, 2 mM $MgCl_2$). WT Gαs and Gαs S275L mutant at a concentration of 4.6 mg/mL (about 100 μM) in 20 mM HEPES 8.0, 150 mM NaCl, 5 mM $MgCl_2$ were diluted to 4 μM in EDTA GNP buffer (1x PBS 7.4, 0.1% BSA, 2 mM EDTA-Na 8.0, 2 mM DTT, 0.1mM $MgCl_2$, 1mM GNP). After incubation at room temperature for 1 hour to allow nucleotide exchange, Gαs dilutions were mixed with equal volume of MgCl2 stock (3.8 mM $MgCl_2$, 1x PBS 7.4, 0.1% BSA, 2mM DTT) to lock Gαs in GNP-bound state. GNP-bound Gαs proteins were then diluted to 500 nM (5X stocks) in assay buffer plus 0.5 mM GNP. In an OptiPlate-384 White Opaque 384-well Microplate, 5X Gαs proteins were mixed with 5X GN13 serial dilution stocks, 5X streptavidin XL665 stock (125 nM), 5X AC stock (VC1: 100 nM, IIC2: 200 nM, FSK 0.5mM) and 5X anti-6His-Tb cryptate stock (0.26 μg/mL) in assay buffer for 1 hour

at room temperature. The plate was read on a TECAN Spark 20 M plate reader using the TR-FRET mode with the following parameters: Lag time: 70 μs, Integration time: 500 μs, Read A: Ex 320(25) nm (filter), Em 610(20) nm (filter), Gain 130, Read B: Ex 320(25) nm (filter), Em 665(8) nm (filter), Gain 165. FRET Signal was calculated as the ratio of [Read B]/[Read A]. In Figure 2A, Final [cyclic peptide]: 0, 0.020, 0.039, 0.078, 0.16, 0.31, 0.62, 1.25, 2.5, 5, 10, 20 μM; Final [Gαs]: 100 nM; Final [VC1]: 20 nM; Final [IIC2]: 40 nM; Final [FSK]: 100 μM. In Figure S3L, Final [cyclic peptide]: 0, 0.677, 2.03, 6.10, 18.3, 54.9, 165, 494, 1481, 4444, 13333, 40000 nM; Final [Gαs]: 100 nM; Final [VC1]: 20 nM; Final [IIC2]: 40 nM; Final [FSK]: 100 μM.

The cADDis cAMP assay

Real-time cAMP dynamics were measured using the Green Up cADDis cAMP biosensor according to the manufacturer's protocol. Briefly, cells were lifted using TrypLE Express and resuspended in media supplemented with the appropriate volume of cADDis BacMam. Cells were plated into a 96-well plate at a concentration of 50,000 cells per well and incubated overnight. In the case of 24 hour drug pretreatment, cADDis media was replaced with 25 μM drug in DMEM supplemented with 1% dialyzed FBS after 4 hours. The next day, plates were washed once with assay buffer (20 mM HEPES pH 7.4, 135 mM NaCl, 5 mM KCl, 0.4 mM $MgCl_2$, 1.8 mM $CaCl_2$, 5 mM d-glucose) before a ten-minute incubation with DMSO or 25 μM drug in a plate reader pre-warmed to 37°C. Fluorescence was detected using an excitation wavelength of 500 nm and an emission wavelength of 530 nm every 30 seconds. After a five-minute baseline reading, vehicle or 20 nM isoproterenol were added, and fluorescence was measured for 30 minutes. A baseline fluorescence (F_0) was calculated for each well by averaging its fluorescence over the five-minute baseline reading, and the fluorescence response at each timepoint was calculated as the change in

fluorescence ($\Delta F = F - F_0$) normalized to the baseline (F_0). Each biological replicate represents the average of at least two technical replicates.

Steady-state GTPase assay

WT Gαs (both short and long) was diluted to a 6 μM stock (4X) in GTPase assay buffer (20 mM HEPES 7.5, 150 mM NaCl, 1 mM $MgCl_2$). The protein was 1:1 (v:v) diluted with 4X cyclic peptide stock (0, 1.56, 3.12, 6.25, 12.5, 25, 50, 100 μM) in GTPase assay buffer, and incubated at 37 °C for an hour. The samples were then 1:1 (v:v) diluted with reaction buffer (20 mM HEPES 7.5, 150 mM NaCl, 1 mM $MgCl_2$, and 1 mM GTP) and incubated at 37 °C. After 30, 50, 70, 90 minutes, 50 μL of the sample was removed to measure the inorganic phosphate (Pi) concentration by PiColorLock™ Phosphate Detection kit. A standard curve was made using the 0.1 mM Pi stock in the kit. Final [cyclic peptide]: 0, 0.39, 0.78, 1.56, 3.12, 6.25, 12.5, 25 μM; Final [Gαs]: 1.5 μM; Final [GTP]: 500 μM.

GDP dissociation assay

Gα proteins were diluted to 400 nM in the EDTA buffer (20 mM HEPES 7.5, 150 mM NaCl, 1 mM EDTA-Na 8.0, 2 mM DTT). [^{3}H]GDP (1 mCi/mL, 25.2 μM) was added to a final concentration of 1.2 μM, followed by cyclic peptides addition. After incubation at 20 °C for 30 minutes, the same volume of assay buffer (20 μM HEPES-Na 7.5, 150 mM NaCl, 2 mM $MgCl_2$, and 1 mM GDP) was added to initiate [^{3}H]GDP dissociation. Final [cyclic peptide]: 10 μM; Final [Gα]: 187 nM; Final [GDP]: 500 μM. At various points, 10 μL of the sample was removed and mixed with 390 μL of ice-cold wash buffer (20 mM HEPES 7.5, 150 mM NaCl, 20 mM $MgCl_2$). The mixture was immediately filtered through a mixed cellulose membrane (25 mm, 0.22 μm)

held by a microanalysis filter holder (EMD Millipore). The membrane was washed by ice-cold wash buffer (500 μL x 3), put in a 6-mL plastic vial and air-dried (room temperature 1.5 h). 5 mL of CytoScint-ES Liquid Scintillation Cocktail was added to each vial. After incubation overnight at room temperature, the vial was used for liquid scintillation counting with a LS 6500 Multi-Purpose Scintillation Counter. The GDP dissociation curves were fitted by the software GraphPad Prism using the following equation to calculate the dissociation rates (k_{off}):

$$Y=Y0 * \exp(-k_{off} * X)$$

in which ‘‘Y’’ is the radioactivity (Counts per minute) of the sample at time ‘‘X’’ (minutes), and Y0 is the calculated radioactivity of the sample at the time point 0.

GTPγS binding assay

Gα proteins were diluted to 10 μM with dilution buffer (20 mM HEPES 7.5, 150 mM NaCl, 1 mM $MgCl_2$, 2 mM DTT, and 20 μM GDP) and incubated with 5X stocks of cyclic peptides at room temperature for 2 hours. GTPγS binding was initiated by mixing with the reaction buffer at room temperature (50 nM [^{35}S]GTPγS and 100 μM GTPγS in dilution buffer) at room temperature. Final [cyclic peptide]: 10 μM; Final [Gα]: 2 μM; Final [GTPγS]: 100 μM. At various time points, 10 μL of the sample was removed and mixed with 390 μL of ice-cold wash buffer (20 mM HEPES 7.5, 150 mM NaCl, 20 mM $MgCl_2$). The mixture was filtered through a mixed cellulose membrane (25 mm, 0.22 μm). The membrane was washed by ice-cold wash buffer (500 μL x 3), put in a 6-mL plastic vial and air-dried (room temperature 1.5 h). 5 mL of CytoScint-ES Liquid Scintillation Cocktail (MP Biomedicals) was added to each vial. After incubation overnight at room temperature, the vial was used for liquid scintillation counting with a LS 6500 Multi-Purpose Scintillation Counter. A standard curve was generated using [^{35}S]GTPγS. The radioactive activity

(Counts per minute) of the samples were converted to the GTPγS concentration. The GTPγS binding curves were fitted by the software GraphPad Prism using the following equation to calculate the apparent GTPγS binding rates (k_{app}):

$$Y = Plateau * (1-exp(-k_{app} * X))$$

in which ‘‘Y’’ is the concentration of GTPγS that bound to Gα protein at time ‘‘X’’ (minutes).

FRET based Gα/Gβγ interaction assay

Biotinylated avi-Gαs (6-end, WT) and avi-Gαi (FL, WT) were diluted to 32 nM (8X) using assay buffer (1X PBS 7.4, 2 mM DTT, 0.1% BSA, 2 mM $MgCl_2$, 0.05% Tween plus 0.5 mM GDP), followed by mixing with a same volume of 8X streptavidin XL665 stock (32 nM in the assay buffer). 8X His-Gβ/γ (C68S) stock (16 nM) and 8X anti-6His-Tb cryptate stock (0.4 μg/mL) were added into the Gα/XL665 mixtures. Finally, 2X stocks of cyclic peptides were (Final cyclic peptide concentrations were indicated in Figures) added with the protein mixtures. After incubation at room temperature for 2 hour at room temperature. The plate was read on a TECAN Spark 20 M plate reader using the TR-FRET mode with the following parameters: Lag time: 70 μs, Integration time: 500 μs, Read A: Ex 320(25) nm (filter), Em 610(20) nm (filter), Gain 130, Read B: Ex 320(25) nm (filter), Em 665(8) nm (filter), Gain 165. FRET Signal was calculated as the ratio of [Read B]/[Read A]. Final [cyclic peptide]: 0, 0.002, 0.006, 0.019, 0.056, 0.169, 0.508, 1.524, 4.57, 12.7, 41.2, 123, 370, 1111, 3333, 10000 nM; Final [Gα]: 4 nM; Final [Gβ1/γ2(C68S)]: 2 nM.

Crystallization

GN13/GNP/Gαs complex: Wild type Gαs (residues 7-380) that was preloaded with GNP and purified by gel filtration was concentrated to 10 mg/mL. The protein was then mixed with 1 mM of GNP (50 mM stock in H2O) and 0.42 mM of the cyclic peptide GN13 (14 mM stock in DMSO). For crystallization, 0.2 µL of the protein sample was mixed with 0.2 µL of the well buffer containing 0.1 M HEPES 7.2, 20% PEG4000, 10% v/v 2-propanol. Crystals were grown at 20 °C in a 96-well plate using the hanging-drop vapour-diffusion method, transferred to a cryoprotectant solution (0.1 M HEPES 7.2, 20% PEG4000, 10% v/v 2-propanol, 150 mM NaCl, 20 mM HEPES 8.0, 5 mM $MgCl_2$, 1 mM GNP, 25% v/v glycerol), and flash-frozen in liquid nitrogen.

GD20/GDP/Gαs complex: Wild type Gαs (NCBI Reference Sequence: NP_536351.1, residues 35-380) was preloaded with GDP, purified by gel filtration and then concentrated to 11.6 mg/mL. Before crystallization, the protein was mixed with 5 mM of Dithiothreitol (0.5 M stock in H2O), 1 mM of GDP (50 mM stock in H2O) and 0.76 mM of the cyclic peptide GD20 (42.6 mM stock in DMSO). For crystallization, 1.5 µL of the protein sample was mixed with 1.5 µL of the well buffer containing 0.1 M Tris 8.2, 26% PEG4000, 0.8 M LiCl. Crystals were grown at 20 °C in a 15-well plate using the hanging-drop vapour-diffusion method, and flash-frozen in liquid nitrogen.

Data collection and structure determination

The data set was collected at the Advanced Light Source beamline 8.2.1 with X-ray at a wavelength of 0.999965 Å. Then the data set was integrated using the HKL2000 package (Otwinowski and Minor, 1997), scaled with Scala (Evans., 2006) and solved by molecular replacement using Phaser (McCoy et al., 2007) in CCP4 software suite (Winn et al., 2011). The

crystal structure of GDP-bound human Gαs R201C/C237 mutant (PDB code: 6AU6) was used as the initial model. The structure was manually refined with Coot (Emsley et al., 2010) and PHENIX (Adams et al., 2010). Data collection and refinement statistics are shown in Table 2.2 and 2.3.

Chloroalkane penetration assay (CAPA)

The cell lines used for CAPA were HeLa cell lines, generated by Chenoweth and co-workers, that stably express HaloTag exclusively in the cytosol (Peraro et al., 2018). Cells were seeded in a 96-well plate the day before the experiment at a density of 4×10^4 cells per well. The day of the experiment the media was aspirated, and 100 µL of cyclic peptide dilutions in DMEM were added to the cells. Plate was incubated for 19.5 h at 37 °C with 5% CO_2. The contents of the wells were aspirated off, and wells were washed using fresh Opti-MEM for 15 min. The wash was aspirated off, and the cells were chased using 5 µM ct-TAMRA for 15 min, except for the No-ct-TAMRA control wells, which were incubated with Opti-MEM alone. The contents of the wells were aspirated and washed with fresh Opti-MEM for 30 min. After aspiration, cells were rinsed once with phosphate-buffered saline (PBS). The cells were then trypsinized, quenched with DMEM, resuspended in PBS, and analyzed using a benchtop flow cytometer (CytoFLEX, Beckman). Final [cyclic peptide]: 0, 0.034, 0.10, 0.31, 0.93, 2.78, 8.33, 25 µM.

BRET2 based Gα Gβγ interaction assay

The plasmids encoding M2R was a gift from Dr. Roderick MacKinnon. The plasmids encoding Gα-RLuc8, Gβ1, and Gγ1-GFP2 were gifts from Dr. Bryan Roth. The plasmid encoding Gγ2-GFP2 was generated by replacing the Gγ1 sequence of pcDNA3.1-GGamma1-GFP2 by digestion with BamHI/XbaI and subsequent insertion of the Gγ2 sequence

(MASNNTASIAQARKLVEQLKMEANIDRIKVSKAAADLMAYCEAHAKEDPLLTPVPASE NPFREKKFFCAIL). All plasmids were sequenced to ensure their identities.

The BRET2 assay was conducted as reported (Olsen et al., 2020). Cells were plated in 10 cm dishes at 2.5-3 million cells per dish the night before transfection. Cells were transfected using a 6:6:3:1 DNA ratio of receptor:Gα-RLuc8:Gβ:Gγ-GFP2 (750:750:375:125 ng for 10 cm dishes). Transit 2020 was used to complex the DNA at a ratio of 3 µL Transit per µg DNA, in OptiMEM at a concentration of 10 ng DNA per µl OptiMEM. 16 hours after transfection, cells were harvested from the plate using TrypLE and plated in poly-D-lysine-coated white, clear-bottom 96-well assay plates at a density of 30,000 -35,000 cells per well.

8 hours after plating in 96-well assay plates, media was replaced with 100 µL of cyclic peptide dilutions (Final cyclic peptide concentrations were indicated in Figures) in DMEM with 1% dialyzed FBS. 16 hours after drug treatment at 37 °C with 5% CO_2, white backings were applied to the plate bottoms, and growth medium was carefully aspirated and replaced immediately with 60 µL of 1.67X drug dilutions in assay buffer (1× Hank's balanced salt solution (HBSS) + 20 mM HEPES, pH 7.4), followed by a 10 µl addition of freshly prepared 50 µM coelenterazine 400a. After a 5 min equilibration period, cells were treated with 30 µL of 3.33X GPCR agonist or DMSO dilutions in assay buffer for an additional 5 min. Plates were then read in a TECAN Spark 20M plate reader with 395 nm (RLuc8-coelenterazine 400a) and 510 nm (GFP2) emission filters, at integration times of 1 s per well. Plates were read serially six times, and measurements from the fourth read were used in all analyses. BRET2 ratios were computed as the ratio of the GFP2 emission to RLuc8 emission.

Whole-cell voltage-clamp recordings on HEK293 cells

The plasmids encoding Gβ1-C Venus, Gγ2-N Venus, and GIRK4-NLuc were gifts from Dr. Roderick MacKinnon. Cells were plated in 6 well plate at 0.55 million cells per well the night before transfection. Cells were transfected β2AR (100 ng), Gβ1-C Venus (25 ng), Gγ2-N Venus (25 ng), GIRK4-NLuc (100 ng). 1.75 µL of Lipofectamine 2000 was used to complex the DNA in 88 µL of OptiMEM. Transfected cells were incubated at 37˚C for 12 hr. After 12 h, cells were plated on glass coverslips and incubated at 37˚C for 12 hr for electrophysiological recordings. Whole-cell voltage-clamp recordings were performed with an Axopatch 200B amplifier (Molecular Devices, San Jose, CA) in the whole-cell mode. The analog current signal was low-pass filtered at 5 kHz (Bessel) and digitized at 50 kHz with a Digidata 1550B digitizer (Molecular Devices, San Jose, CA). Digitized data was recorded using the software pClamp 10.7. Patch electrodes (resistance 2.0–4.0 MΩ) were pulled on a Sutter P-97 puller (Sutter Instrument Company, Novato, CA) from 1.5 mm outer diameter filamented borosilicate glass. Extracellular solution contained 140 mM NaCl, 5 mM KCl, 2 mM $CaCl_2$, 2 mM $MgCl_2$, 10 mM D-glucose, 10 mM HEPES-NaOH (pH 7.4) (~330 mOsm). The extracellular solution was exchanged to high K+ solution containing 40 mM NaCl, 100 mM KCl, 2 mM $CaCl_2$, 2 mM $MgCl_2$, 10 mM D-glucose, 10 mM HEPES-NaOH (pH 7.4) (~330 mOsm). The pipette solution contained 13.5 mM NaCl, 140 mM K-aspartate, 1.6 mM MgCl2, 0.09 mM EGTA-K, 9 mM HEPES-KOH (pH 7.2) (~290 mOsm). 1% DMSO, 25 µM F5A in 1% DMSO, or 25 µM F10L in 1% DMSO was added to the pipette solution before the experiments.

Chemical stability assay in DMEM with 10% FBS or human Plasma

These assays were conducted by Pharmaron Beijing CO., Ltd. Cyclic peptides working solutions were prepared at 10 μM in DMEM with 10% FBS (Avantor, Cat# 76294-180) or human plasma (Pooled, Male & Female, BioIVT, Cat# HMN666664). The assays were performed in duplicate. Vials were incubated at 37°C at 60 rpm in a water bath and taken at designated time points including 0, 480, 1080 and 1440 min. For each time point, the initiation of the reaction was staggered so all the time points were terminated with cold acetonitrile containing internal standards (IS, 100 nM alprazolam, 200 nM labetalol, 200 nM Imipramine and 2 μM ketoplofen) at the same time. Samples were vortexed then centrifuged at 4°C to remove proteins. The supernatants from centrifugation were diluted by ultra-pure H2O and used for LC-MS/MS analysis. All calculations were carried out using GraphPad Prism. Remaining percentages of parent compounds at each time point were estimated by determining the peak area ratios from extractedion chromatograms.

Chemical synthesis

(1) Solid phase synthesis of cyclic peptides

Macrocyclic peptides (25 μmol scale) were synthesized by a standard Fmoc solid phase peptide synthesis method using a Syro Wave automated peptide synthesizer (Morimoto et al., 2012). After addition of a chloroacetyl group onto the N-terminal amide group (for the formation of cyclic peptide), peptides were cleaved from the NovaPEG Rink Amide resin (Novabiochem) by a solution of 92.5% trifluoroacetic acid (TFA), 2.5% 3,6-Dioxa-1,8-octanedithiol ethanedithiol (DODT), 2.5% triisopropylsilane (TIPS) and 2.5% water and precipitated by diethyl ether. To conduct the macrocyclization reaction, the peptide pellet was dissolved in 10 ml DMSO containing 10 mM tris(2-carboxyethyl)phosphine hydrochloride (TCEP), adjusted to pH>8 by addition of

triethylamine (TEA) and incubated at 25 °C for 1 hour. This cyclization reaction was quenched by acidification of the solution with TFA. The crude products were purified by reverse-phase HPLC (RP-HPLC) (Shimadzu) with a Chromolith RP-18 100-25 prep column. Molecular masses were verified by a time-of-flight mass spectrometer (Waters Xevo G2-XS), and the purity was verified by analytical HPLC on a Waters Acquity UPLC BEH C18 1.7 μm column.

(2) General synthesis route of chloroalkane tagged cyclic peptides

In this work, we prepared a chloroalkane tag (ct) that has been previously used with the HaloTag system (Neklesa et al., 2011). Instead of using the Rink amide resin, peptides were synthesized using the Fmoc-Wang resin (Anaspec, AS-20058) to generate a carboxylate at the C-terminus. To cap the C-terminus with the chloroalkane tag (ct), 10 equiv of chloroalkane tag (ct), 5 equiv of HATU, and 20 equiv of DIPEA were dissolved in DMF and stirred for 1 hour at room temperature. Crude peptides were purified by reverse-phase HPLC (Waters XBridge C18 column 5 μm particle size 30 x 250 mm, 5–95% acetonitrile–water + 0.1% formic acid, 40 min, 20 mL/min) to afford the chloroalkane tagged peptides.

(3) Characterization Data for Cyclic Peptides

Mass Spectrometry

GN13: HRMS (ESI): Calcd for ($C_{79}H_{106}N_{16}O_{21}S$ + 2H)2+: 824.3798, Found: 824.3973.

GN13-E3A: HRMS (ESI): Calcd for ($C_{77}H_{104}N_{16}O_{19}S$ + 2H)2+: 795.3770, Found: 795.3749.

GN13-I8A: HRMS (ESI): Calcd for ($C_{76}H_{100}N_{16}O_{21}S$ + 2H)2+: 803.3563, Found: 803.3563.

GN13-W9A: HRMS (ESI): Calcd for ($C_{71}H_{101}N_{15}O_{21}S$ + 2H)2+: 766.8587, Found: 766.8610.

cpGN13: HRMS (ESI): Calcd for ($C1_{40}H_{223}N_{53}O_{37}S$ + 3H)3+: 1091.2384, Found: 1091.5806.

GN13-E3Q-Biotin: HRMS (ESI): Calcd for ($C_{113}H_{170}N_{20}O_{33}S_2$ + 2H)2+: 1200.5919, Found: 1200.5970.

ct-GN13-E3Q: HRMS (ESI): Calcd for ($C_{89}H_{126}ClN_{17}O_{22}S$ + 2H)2+: 926.9416, Found: 926.9422.

GD20: HRMS (ESI): Calcd for ($C_{90}H_{126}N_{22}O_{20}S$ + 2H)2+: 934.4698, Found: 934.4844. cpGD20 (GD20-F10L): HRMS (ESI): Calcd for ($C_{87}H_{128}N_{22}O_{20}S$ + 2H)2+: 917.4776, Found: 917.4901.

ct-GD20: HRMS (ESI): Calcd for ($C_{100}H_{145}ClN_{22}O_{22}S$ + 2H)2+: 1037.5235, Found: 1037.5303.

ct-GD20-F10L: HRMS (ESI): Calcd for ($C_{97}H_{147}ClN_{22}O_{22}S$ + 2H)2+: 1020.5313, Found: 1020.5193.

GD20-Biotin: HRMS (ESI): Calcd for ($C_{124}H_{189}N_{25}O_{33}S_2$ + 2H)2+: 1311.1739, Found: 1311.1741.

cpGD20-Biotin: HRMS (ESI): Calcd for ($C_{121}H_{191}N_{25}O_{33}S_2$ + 2H)2+: 1294.1817, Found: 1294.1805.

GD20-F5A: HRMS (ESI): Calcd for ($C_{84}H_{122}N_{22}O_{20}S$ + 2H)2+: 896.4542, Found: 896.4604.

cpGD20-F5A: HRMS (ESI): Calcd for ($C_{81}H_{124}N_{22}O_{20}S$ + 2H)2+: 879.4620, Found: 879.4648.

GD20-R6A: HRMS (ESI): Calcd for ($C_{87}H_{119}N_{19}O_{20}S$ + 2H)2+: 891.9378, Found: 891.9394.

GD20-W8A: HRMS (ESI): Calcd for ($C_{82}H_{121}N_{21}O_{20}S$ + 2H)2+: 876.9487, Found: 876.9509

Absorbance was recorded at 280 nm.

Quantification and statistical analysis

All of the curves in Figures except those from the BLI experiments were fitted by GraphPad Prism. Raw kinetic data collected from the BLI experiments were processed with the Data Analysis software provided by the manufacturer. All the details can be found in the figure legends and in the Materials and Methods. The data collection and refinement statistics of the crystal structures can be found in Tables.

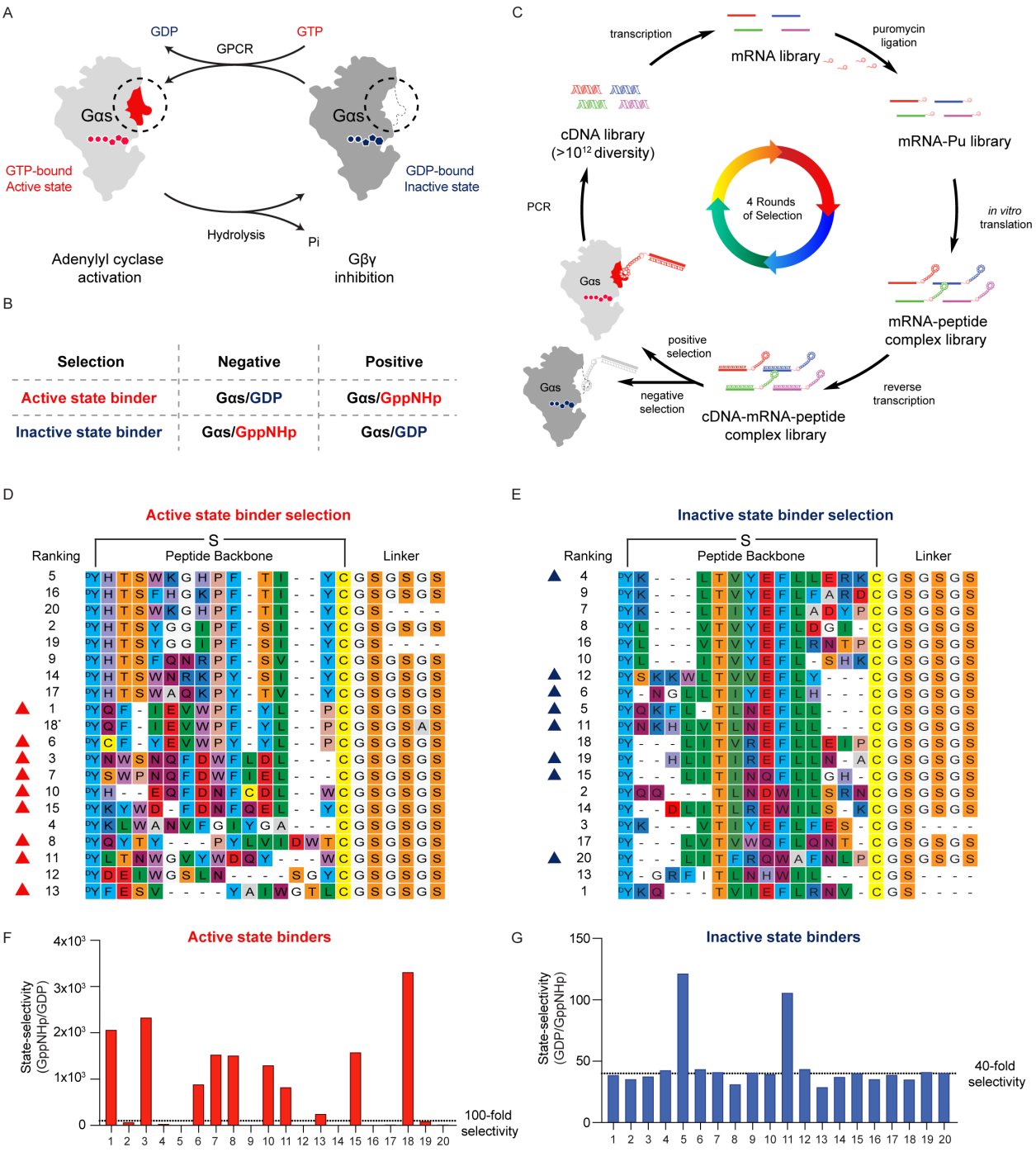

Figure 2.1 | RaPID selection of state-selective Gαs binding cyclic peptides. (**A**) The molecular switch Gαs adopts distinct conformations, governed by its guanine nucleotide binding state. Switch regions are highlighted with circle. (**B**) A selection strategy to achieve state-selectivity of Gαs binders. (**C**) Schematic representation of RaPID selection. (e.g., Gαs active state binder selection, positive selection = Gαs/GNP (light grey), negative selection = Gαs/GDP (dark grey)). (**D-E**) Sequence alignment of top 20 cyclic peptides from the last round of positive selections. The 18th peptide (asterisk) from the active state binder selection was not selected because it has the same core sequence as the 1st peptide. (**F-G**) Comparison

selection was performed by analyzing peptide-mRNA-cDNA complex binding to GDP- or GNP-bound Gαs-immobilized beads from the last round of selections, respectively. Cyclic peptides with high selectivity are marked with triangles and were selected for solid phase synthesis.

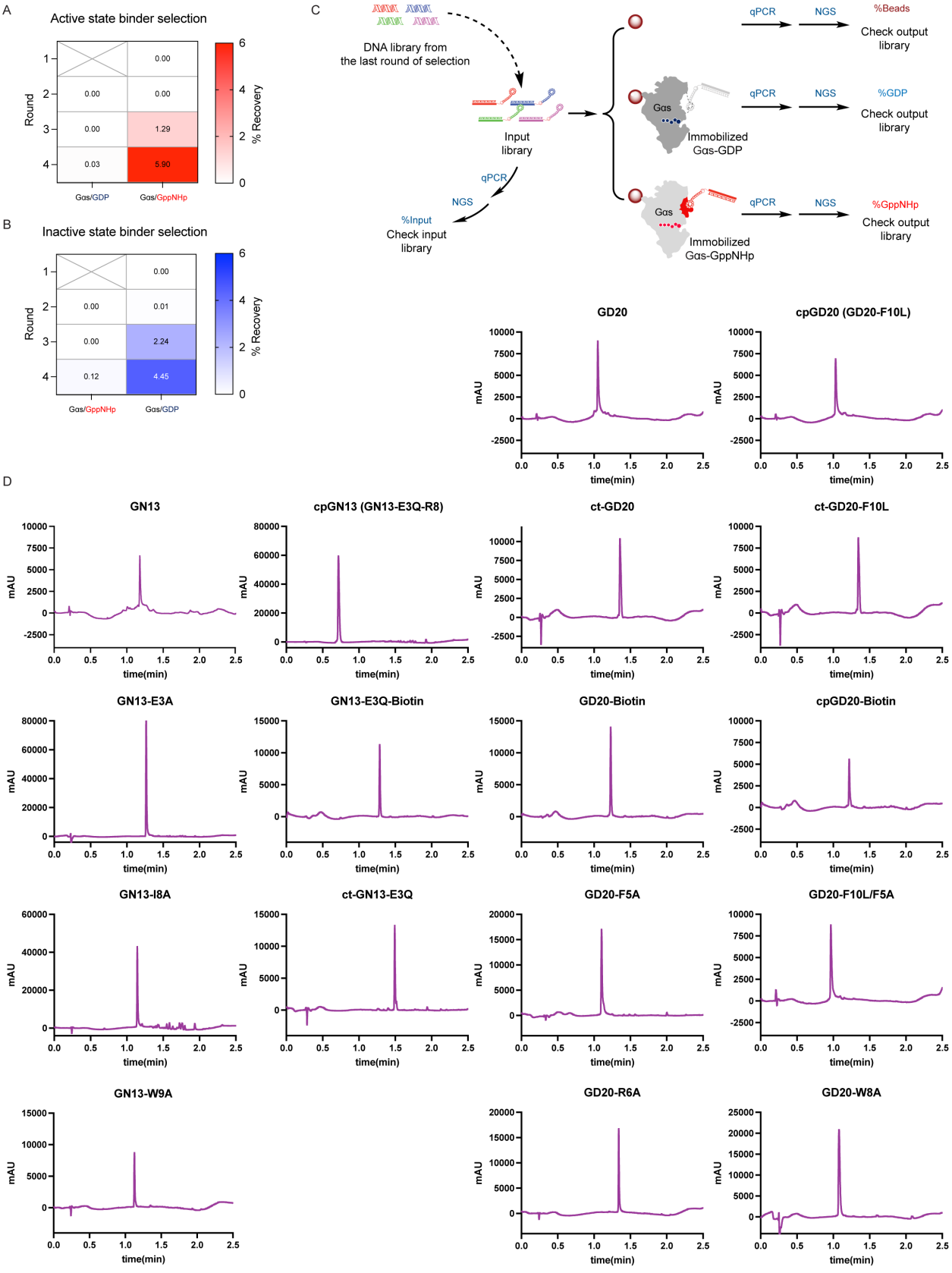
A
Active state binder selection
Round
Gαs/GDP
Gαs/GppNHp
% Recovery
B
Inactive state binder selection
C
DNA library from the last round of selection
Input library
qPCR
NGS
%Input
Check input library
Immobilized Gαs-GDP
Immobilized Gαs-GppNHp
%Beads
%GDP
%GppNHp
Check output library
D
GD20
cpGD20 (GD20-F10L)
GN13
cpGN13 (GN13-E3Q-R8)
ct-GD20
ct-GD20-F10L
GN13-E3A
GN13-E3Q-Biotin
GD20-Biotin
cpGD20-Biotin
GN13-I8A
ct-GN13-E3Q
GD20-F5A
GD20-F10L/F5A
GN13-W9A
GD20-R6A
GD20-W8A
mAU
time(min)

Figure 2.2 | RaPID selection of state-selective Gαs binding cyclic peptides and cyclic peptides characterizations. (**A** and **B**) The percentage of enriched peptide-mRNA-cDNA complex in the input library after each selection was quantified by qPCR. Cyclic peptides that bind to GNP-bound (A) or GDP-bound (B) Gαs were enriched through four rounds of RaPID selection. To ensure a maximum library diversity at the initial stage of selection, negative selection was not included in the first round of selection. (**C**) Comparison selection. DNA sequences of cyclic peptide binders from the last round of selection were quantified and identified by qPCR and NGS. A peptide-mRNA-cDNA complex library was produced based on the above-mentioned DNA sequences and equally split into three fractions. Binding of each individual peptide-mRNA-cDNA complex to blank, GDP-bound Gαs-immobilized or GNP-bound Gαs-immobilized beads was quantified by qPCR and NGS, respectively. (**D**) Analytical HPLC Traces of resynthesized cyclic peptides. Absorbance was recorded at 280 nm.

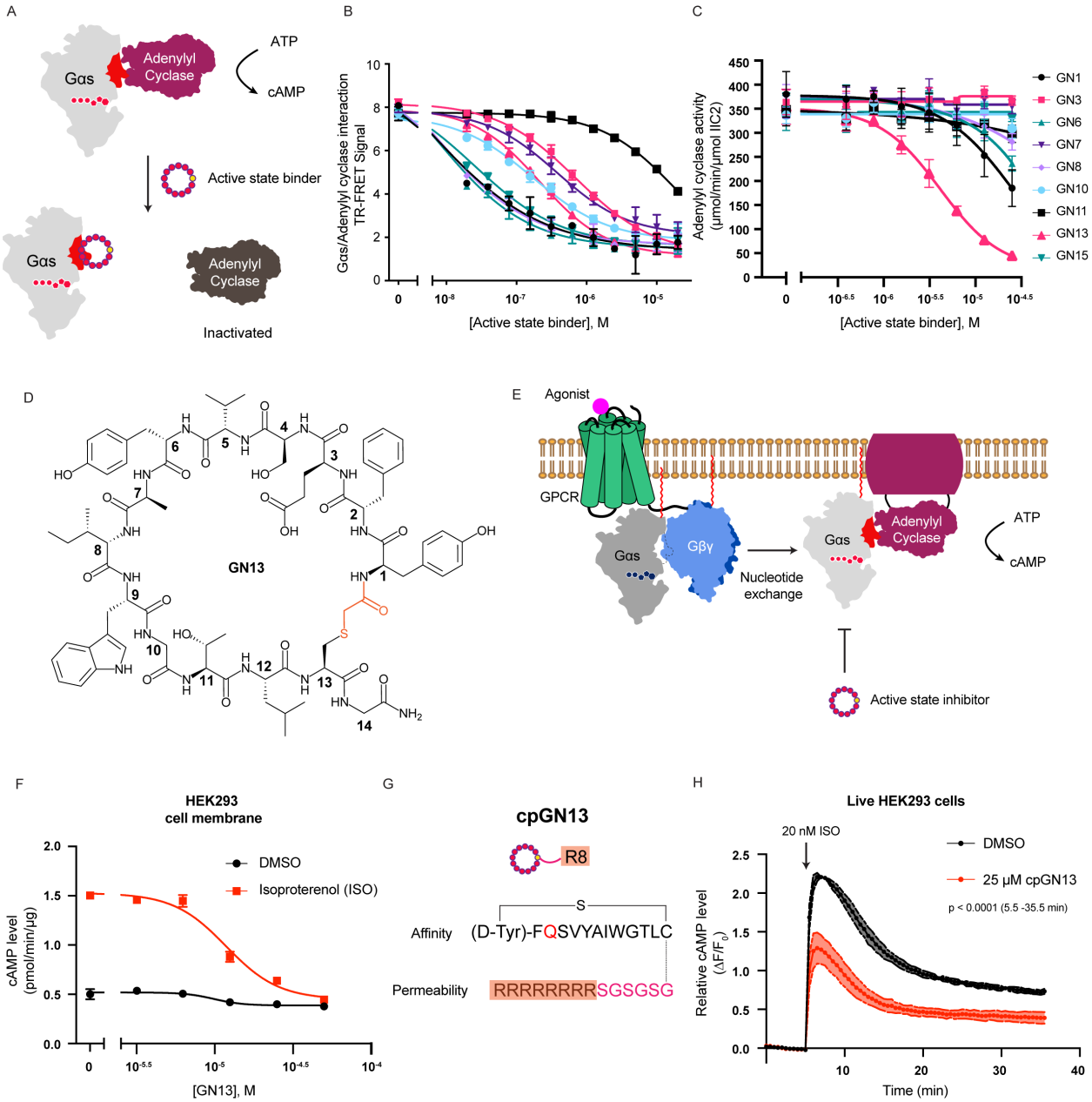

Figure 2.3 | Gαs active state inhibitor GN13 inhibits Gαs-mediated adenylyl cyclase activation. (**A**) Schematic representation of active state binders inhibiting Gαs-mediated AC activation. (**B**) Active state binders inhibited protein-protein interaction between Gαs/GNP and AC. Mean ± SD, n = 3. (**C**) Gαs/GNP mediated AC activation was inhibited by active state binders. Mean ± SE, n = 3. (**D**) Structure of the resynthesized cyclic peptide GN13. (**E**) Schematic representation of GN13 inhibiting GPCR-stimulated Gαs/AC activity in cells. (F) GN13 inhibited ISO-stimulated cAMP production in HEK293 cell membranes. Mean ± SD, n = 3. (**G**) Design of a cell permeable GN13 analog, cpGN13. (**H**) GN13 inhibited ISO-stimulated cAMP production in live HEK293 cells. Mean ± SD, n = 3. Two-tailed unpaired t-tests were performed using data after 5min.

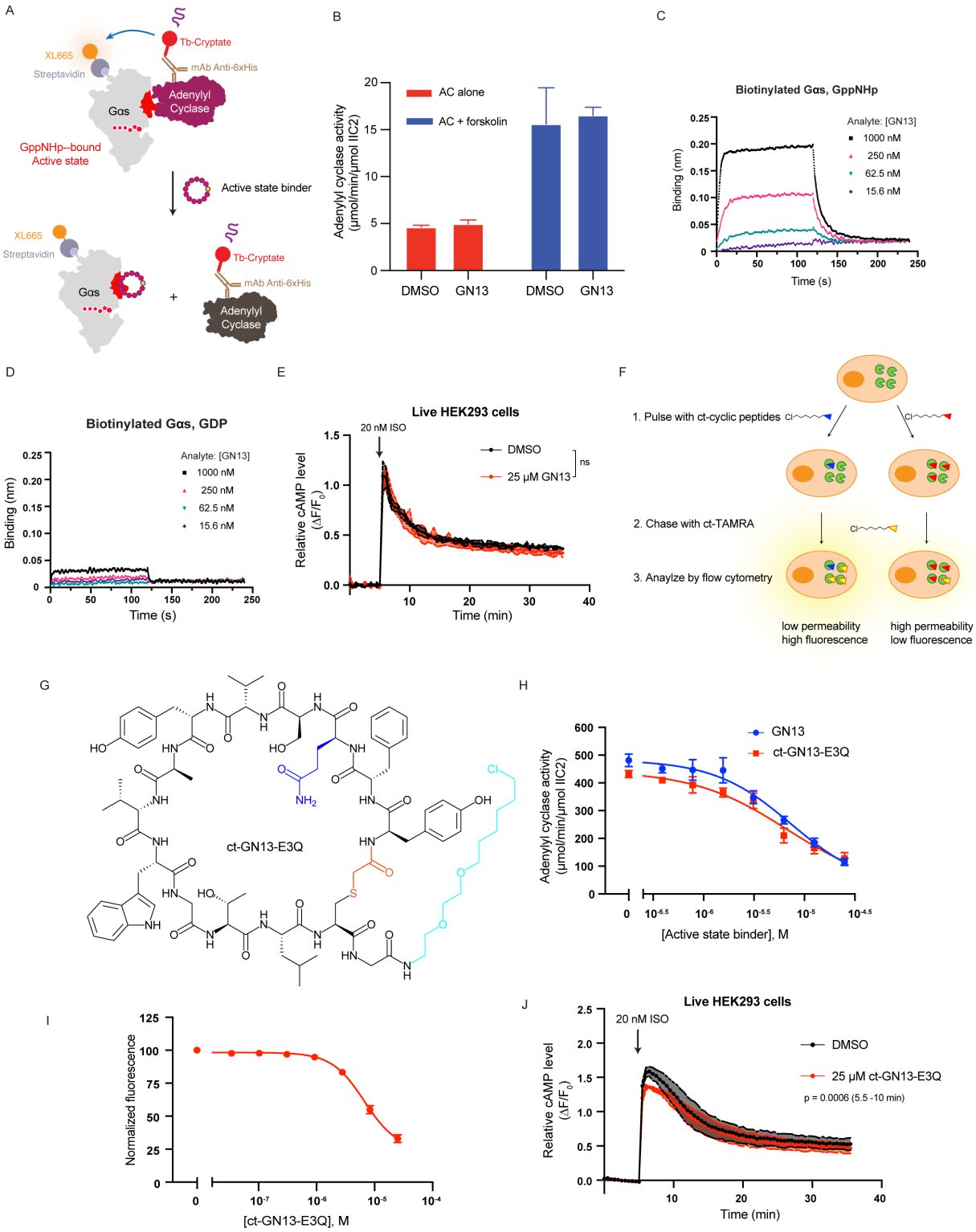
A
Tb-Cryptate
XL665
Streptavidin
mAb Anti-6xHis
Adenylyl Cyclase
Gαs
GppNHp–bound Active state
Active state binder
B
AC alone
AC + forskolin
Adenylyl cyclase activity (µmol/min/µmol IIC2)
DMSO
GN13
C
Biotinylated Gαs, GppNHp
Analyte: [GN13]
1000 nM
250 nM
62.5 nM
15.6 nM
Binding (nm)
Time (s)
D
Biotinylated Gαs, GDP
E
Live HEK293 cells
20 nM ISO
DMSO
25 µM GN13
ns
Relative cAMP level (ΔF/F0)
Time (min)
F
1. Pulse with ct-cyclic peptides
2. Chase with ct-TAMRA
3. Anaylze by flow cytometry
low permeability high fluorescence
high permeability low fluorescence
G
ct-GN13-E3Q
H
GN13
ct-GN13-E3Q
[Active state binder], M
I
Normalized fluorescence
[ct-GN13-E3Q], M
J
Live HEK293 cells
20 nM ISO
DMSO
25 µM ct-GN13-E3Q
p = 0.0006 (5.5 -10 min)

Figure 2.4 | Characterizations of the Gαs active state inhibitor GN13 and its analogs. (**A**) Schematic representation of active state binders inhibiting the protein-protein interaction between biotinylated GNP-bound Gαs WT and His-tagged AC. (**B**) GN13 did not directly inhibit AC activity in the absence of Gαs. 25 μM of GN13 or DMSO were mixed with AC (VC1/IIC2), followed by addition of DMSO or forskolin. After adding ATP, the reaction was carried out at 30 °C for 10 min. Production of cAMP was evaluated by the LANCE Ultra cAMP kit. The data represent the mean ± SE of three independent measurements. (**C-D**) Binding kinetics of GN13 to GNP-bound (C) or GDP-bound (D) Gαs were quantified using bio-layer Interferometry (BLI). Biotinylated Gαs proteins were immobilized to give a relative intensity of 2-3 nm on streptavidin biosensors. Association (t = 0-120 s) and dissociation (t = 120-240 s) cycles of compounds were started by dipping sensors into cyclic peptide solutions and control buffer. Binding signals were reference-subtracted. The assay was performed in duplicate, and the data represent one of the two replicates. (**E**) Real-time cAMP levels in HEK293 cells were measured using the Green Up cADDis cAMP biosensor after 24 hours of 25 μM GN13 treatment. The data represent the mean ± SD of three independent biological replicates. Each biological replicate represents the average of at least two technical replicates. Two-tailed unpaired t-tests were performed using data after 5min. $P < 0.05$ was considered significant. ns $p > 0.05$. (**F**) Schematic representation of the chloroalkane penetration assay (CAPA). HeLa cells stably express GFP-tagged HaloTag on the mitochondrial outer membrane. If the pre-dosed chloroalkane-tagged molecule (ct-molecule) penetrates the cell membrane, it will covalently label HaloTag and block subsequent HaloTag labeling with ct-TAMRA. Intracellular ct-TAMRA fluorescence intensity is inversely related to the amount of cytosolic ct-molecule. (**G**) Structure of ct-GN13-E3Q. Mutations are colored blue. The ct tag is colored cyan. (**H**) Activation of AC by Gαs was inhibited by both GN13 and ct-GN13-E3Q in a dose-dependent manner. Both peptides showed similar inhibitory effects. The assay was performed as descried in Figure 2C. The data represent the mean ± SE of three independent measurements. (**I**) CAPA cell permeability assay result of ct-GN13-E3Q. Each point is the median ct-TAMRA fluorescence of 10,000 cells. The data were normalized using cells that were only treated with ct-TAMRA as 100% signal and cells that were not treated with any ct-compound as 0% signal. The data represent the mean ± SD of three independent biological replicates. (**J**) Real-time cAMP levels in HEK293 cells were measured using the Green Up cADDis cAMP biosensor after 24 hours of 25 μM ct-GN13-E3Q treatment. The data represent the mean ± SD of three independent biological replicates. Each biological replicate represents the average of at least two technical replicates. Two-tailed unpaired t-tests were performed using data between 5.5-10 min (peak activation). $P < 0.05$ was considered significant.

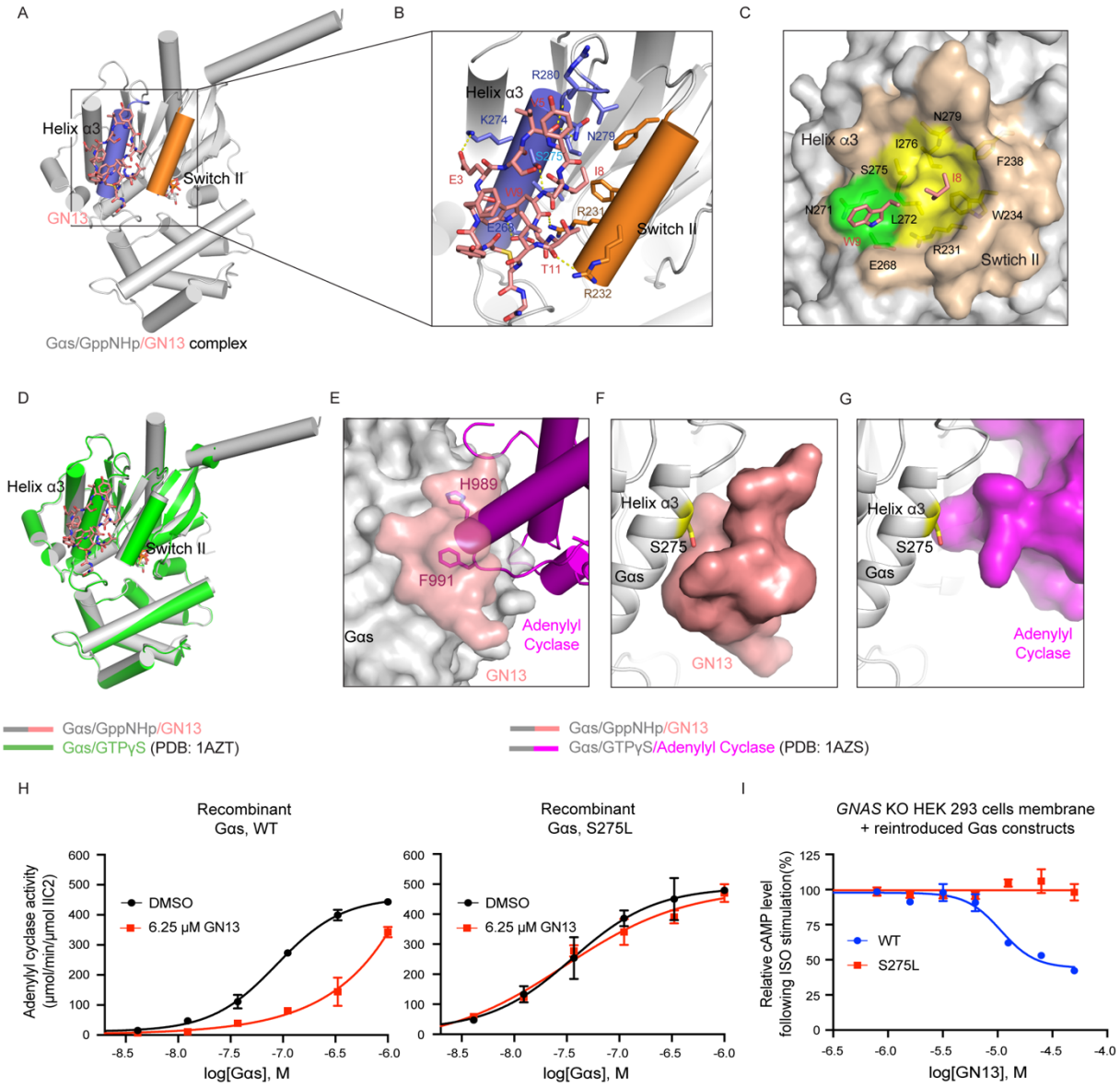

Figure 2.5 | The crystal Structure of GNP-bound Gαs in complex with GN13. (**A**) Overall structure of the GN13/GNP/Gαs complex. GN13 (salmon) binds in between switch II (orange) and the α3 helix (slate). (**B**) Structural details of GN13/Gαs interaction. Hydrogen bonds are represented by yellow dashed lines. (**C**) Close-up view of two Gαs hydrophobic pockets (green and yellow) that accommodate I8 and W9 of GN13 (salmon). Gαs residues that form those pockets are depicted as stick models. (**D**) Alignment of Gαs/GN13 complex structure (grey) with the structure of GTPγS-bound Gαs (green) (PDB: 1AZT). Root mean square deviation (RMSD) = 0.479 Å. (**E**) Our Gαs/GN13 (grey/salmon) complex structure was superimposed to the Gαs/AC complex structure (grey/magenta) (PDB: 1AZS). GN13 blocks H989/F991 of AC from binding to the same pocket in Gαs. (**F-G**) Close-up view of the interaction between GN13 (salmon) and the Gαs α3 helix (grey) in (F) and the interaction between AC (magenta) and the Gαs α3 helix in (G) (PDB: 1AZS). S275 is shown as sticks. (**H**) Gαs WT and Gαs S275L have comparable biochemical activities in the AC activation assay (black curves). GN13 inhibited AC activation by Gαs WT

(red curve, left) but not by Gαs S275L (red curve, right). Mean ± SD, n = 3. (**I**) Gαs S275L confers resistance to GN13 inhibition in HEK293 cell membranes. Mean ± SD, n = 3.

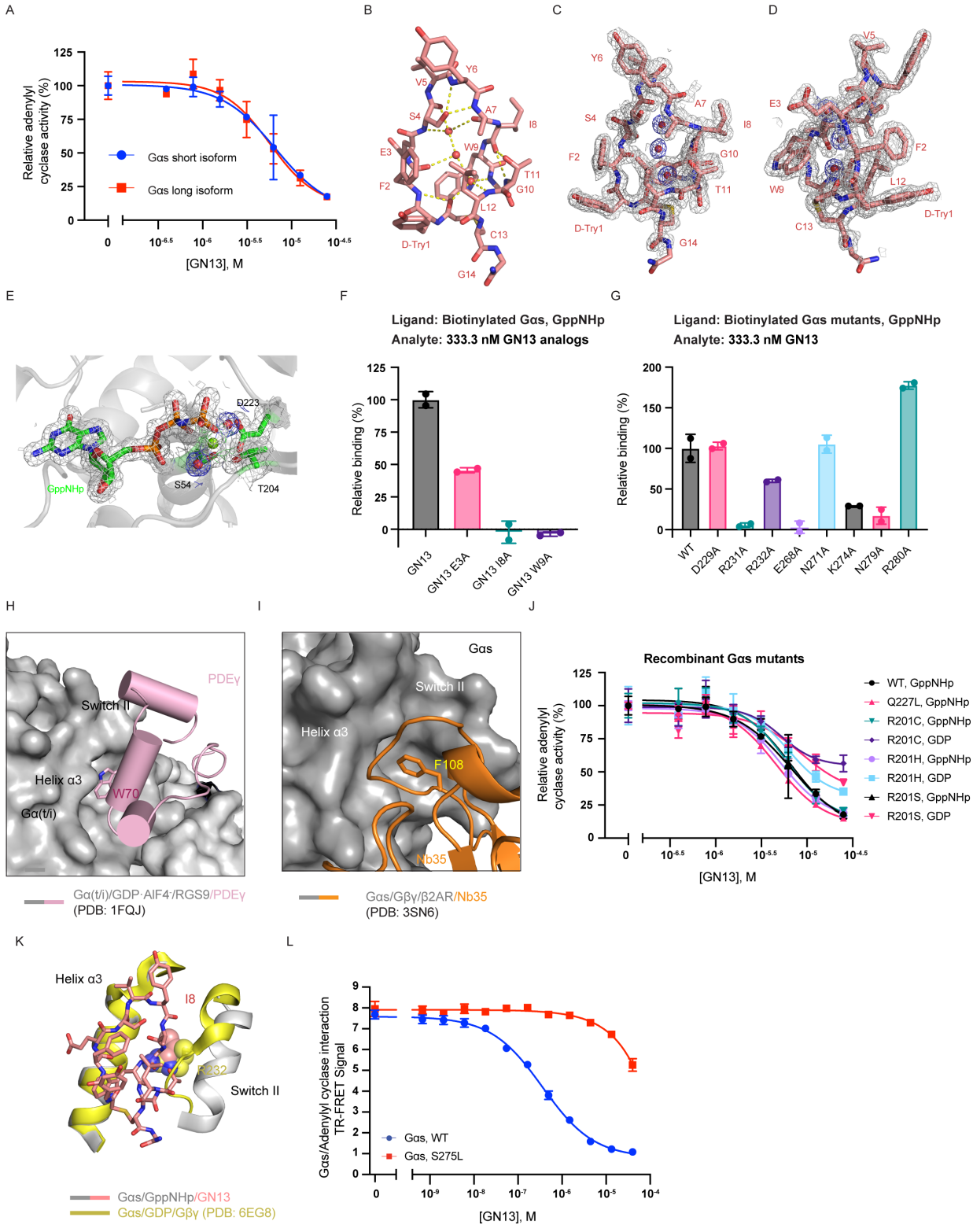
A
Relative adenylyl cyclase activity (%)
Gαs short isoform
Gαs long isoform
[GN13], M
B
C
D
E
GppNHp
D223
S54
T204
F
Ligand: Biotinylated Gαs, GppNHp
Analyte: 333.3 nM GN13 analogs
Relative binding (%)
GN13
GN13 E3A
GN13 I8A
GN13 W9A
G
Ligand: Biotinylated Gαs mutants, GppNHp
Analyte: 333.3 nM GN13
Relative binding (%)
WT
D229A
R231A
R232A
E268A
N271A
K274A
N279A
R280A
H
PDEγ
Switch II
Helix α3
W70
Gα(t/i)
Gα(t/i)/GDP·AlF4⁻/RGS9/PDEγ
(PDB: 1FQJ)
I
Gαs
Switch II
Helix α3
F108
Nb35
Gαs/Gβγ/β2AR/Nb35
(PDB: 3SN6)
J
Recombinant Gαs mutants
Relative adenylyl cyclase activity (%)
WT, GppNHp
Q227L, GppNHp
R201C, GppNHp
R201C, GDP
R201H, GppNHp
R201H, GDP
R201S, GppNHp
R201S, GDP
[GN13], M
K
Helix α3
I8
R232
Switch II
Gαs/GppNHp/GN13
Gαs/GDP/Gβγ (PDB: 6EG8)
L
Gαs/Adenylyl cyclase interaction
TR-FRET Signal
Gαs, WT
Gαs, S275L
[GN13], M

Figure 2.6 | GN13 specifically inhibits Gαs through binding to a crystallographically defined pocket. (**A**) Activation of AC by both short and long isoforms of Gαs was inhibited by GN13 in a dose-dependent manner. The assay was performed as descried in Figure 2C. The data represent the mean ± SD of three independent replicates. (**B**) GN13 adopts a highly ordered three-dimensional structure through intramolecular and intermolecular hydrogen bonding network. GN13 is shown as salmon sticks. Three water molecules with well-defined electron density are shown as red spheres. Hydrogen bonds are represented by yellow dash lines. (**C** and **D**) Electron density map of GN13. GN13 is shown as salmon sticks. Three water molecules with well-defined electron density are shown as red spheres. The 2mFo-DFc electron density map of the structure is contoured at 1.0 σ and colored grey (GN13) and blue (Water), respectively. (**E**) Electron density map of GNP. GNP and the side chains of S54, T204 and D223 are shown as sticks. The Mg2+ and two water molecules coordinated with the Mg2+ are shown as green and red spheres, respectively. The 2mFo-DFc electron density map of the structure is contoured at 1.0 σ. (**F**) Binding of GN13 analogs to WT GNP-bound Gαs were quantified using BLI. Biotinylated WT GNP-bound Gαs proteins were immobilized to give a relative intensity of 2-3 nm on streptavidin biosensors, following the same association/dissociation cycles descried in Figure S2C. Binding signals were double referenced and normalized to WT Gαs loading and GN13/WT Gαs binding signal. The data represent the mean ± SD of two independent measurements. (**G**) Binding of GN13 to different GNP-bound Gαs mutants were quantified using BLI. Biotinylated GNP-bound Gαs proteins were immobilized to give a relative intensity of 2-3 nm on streptavidin biosensors, following the same association/dissociation cycles descried in Figure S2C. Binding signals were double referenced and normalized to Gαs loading and GN13/WT Gαs binding signal. The data represent the mean ± SD of two independent measurements. (**H**) Structure of the GDP•AlF4--bound Gα(t/i)/RGS9/PDEγ complex (PDB: 1FQJ). A critical tryptophan residue from PDEγ (pink, cartoon) engages the hydrophobic pocket between the switch II region and the α3 helix. Gα(t/i) and RGS9 are shown as surface. PDEγ is shown as cartoon. (**I**) Structure of the Gαs/Gβγ/β2AR/Nb35 complex (PDB: 3SN6). A critical phenylalanine residue from Nb35 (orange, cartoon) engages the hydrophobic pocket between the switch II region and the α3 helix. Gαs is shown as surface. Nb35 is shown as cartoon. (**J**) Activation of AC by Gαs oncogenic mutants was inhibited by GN13 in a dose-dependent manner. The assay was performed as descried in Figure 2C. The data represent the mean ± SD of three independent measurements. (**K**) Structural basis for nucleotide-state-selective binding of GN13 to Gαs. In GDP-bound Gαs (yellow), switch II is partially disordered, which disrupts polar contacts with GN13 and creates extensive steric hindrance. In particular, R232 of switch II (shown in space filling) is predicted to create a steric clash with I8 of GN13. (**L**) GN13 inhibited protein-protein interaction between Gαs WT and AC in a dose-dependent manner (blue). This inhibitory effect was significantly diminished by the S275L mutation (red). The data represent the mean ± SD of three independent measurements.

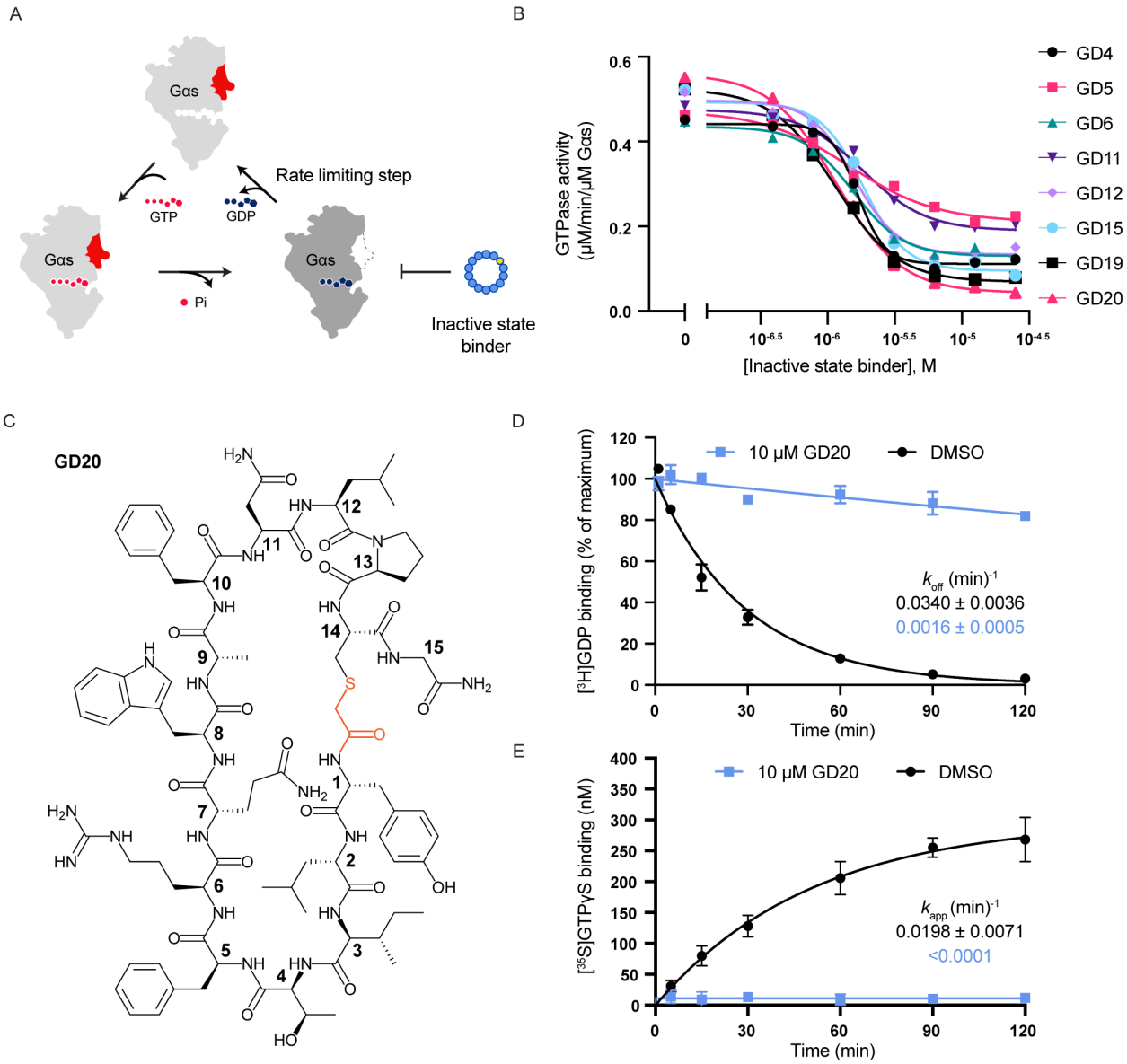

Figure 2.7 | Inactive state binding cyclic peptide GD20 is a Gαs specific guanine nucleotide dissociation inhibitor (GDI). (**A**) Schematic representation of inactive state binders inhibiting Gαs steady-state GTPase activity. (**B**) Gαs steady-state GTPase activity was inhibited by inactive state. The data represent one measurement. Gαs steady-state GTPase activity in the presence of GD20 was repeated twice in Figure S4A. (**C**) Structure of the resynthesized cyclic peptide GD20. (**D**) GD20 inhibited Gαs GDP dissociation. Mean ± SD, n = 3. (**E**) GD20 inhibited GTPγS binding to Gαs. Mean ± SD, n = 3.

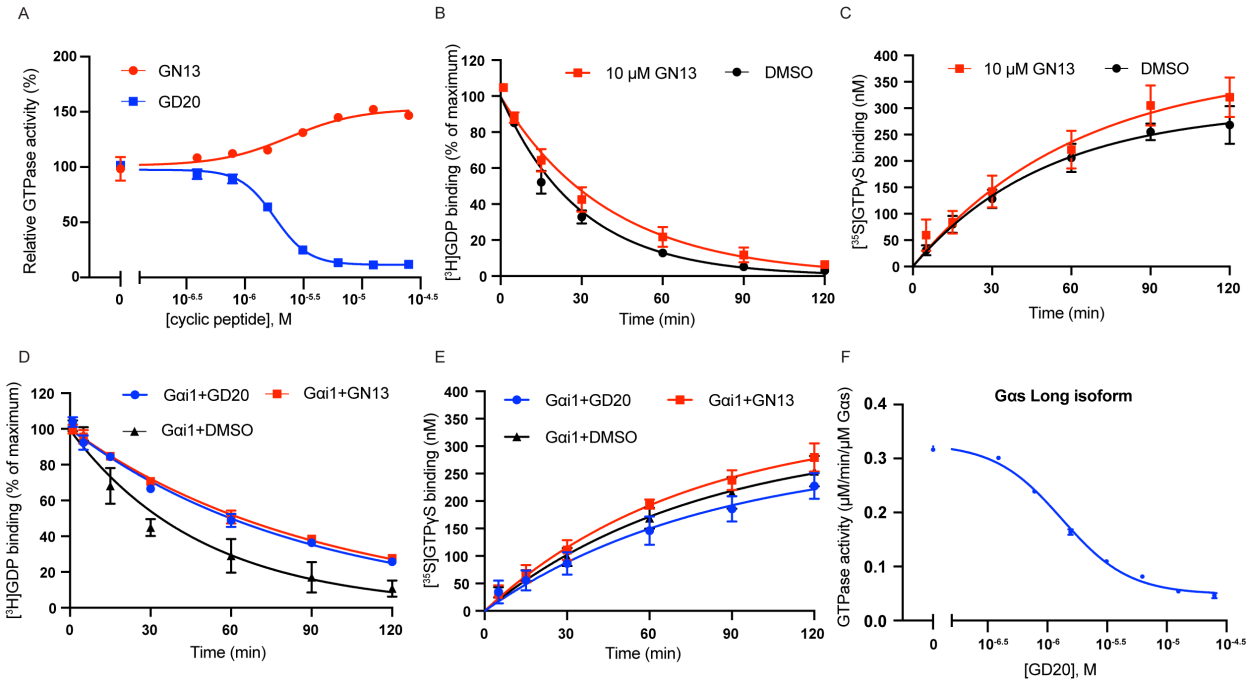

Figure 2.8 | GN13 and GD20 modulate Gαs GTPase activity through a Gαs-specific manner. (**A**) Gαs steady-state GTPase activity was modulated by GN13 and GD20 in a dose-dependent manner. The data represent the mean ± SD of three independent measurements. (**B**) The rates of GDP dissociation from Gαs in the presence (red) or absence (black) of 10 μM GN13 were determined. Gαs preloaded with [^{3}H]GDP was assayed in a buffer containing 1 mM MgCl2, 0.5 mM GDP, and the indicated concentration of GN13. The data represent the mean ± SD of three independent replicates. (**C**) The rates of GTPγS binding to Gαs in the presence (red) or absence (black) of 10 μM GN13 were determined by mixing GDP-bound Gαs with a mixture of [^{35}S]GTPγS and GTPγS in a buffer containing 1 mM MgCl2. The data represent the mean ± SD of three independent replicates. (**D**) The rates of GDP dissociation from Gαi1 in the presence of 10 μM GN13 (red), or 10 μM GD20 (blue) or DMSO (black) were determined. Gαi1 preloaded with [^{3}H]GDP was assayed in a buffer containing 1 mM MgCl2, 0.5 mM GDP, and the indicated concentration of cyclic peptides. The data represent the mean ± SD of three independent replicates. (**E**) The rates of GTPγS binding to Gαi1 in the presence of 10 μM GN13 (red), or 10 μM GD20 (blue) or DMSO (black) were determined by mixing GDP-bound Gαi1 with a mixture of [^{35}S]GTPγS and GTPγS in a buffer containing 1 mM MgCl2. The data represent the mean ± SD of three independent replicates. (**F**) Steady-state GTPase activities of short and long isoforms of Gαs were inhibited by GD20 in a dose-dependent manner. The data represent the mean ± SD of three independent measurements.

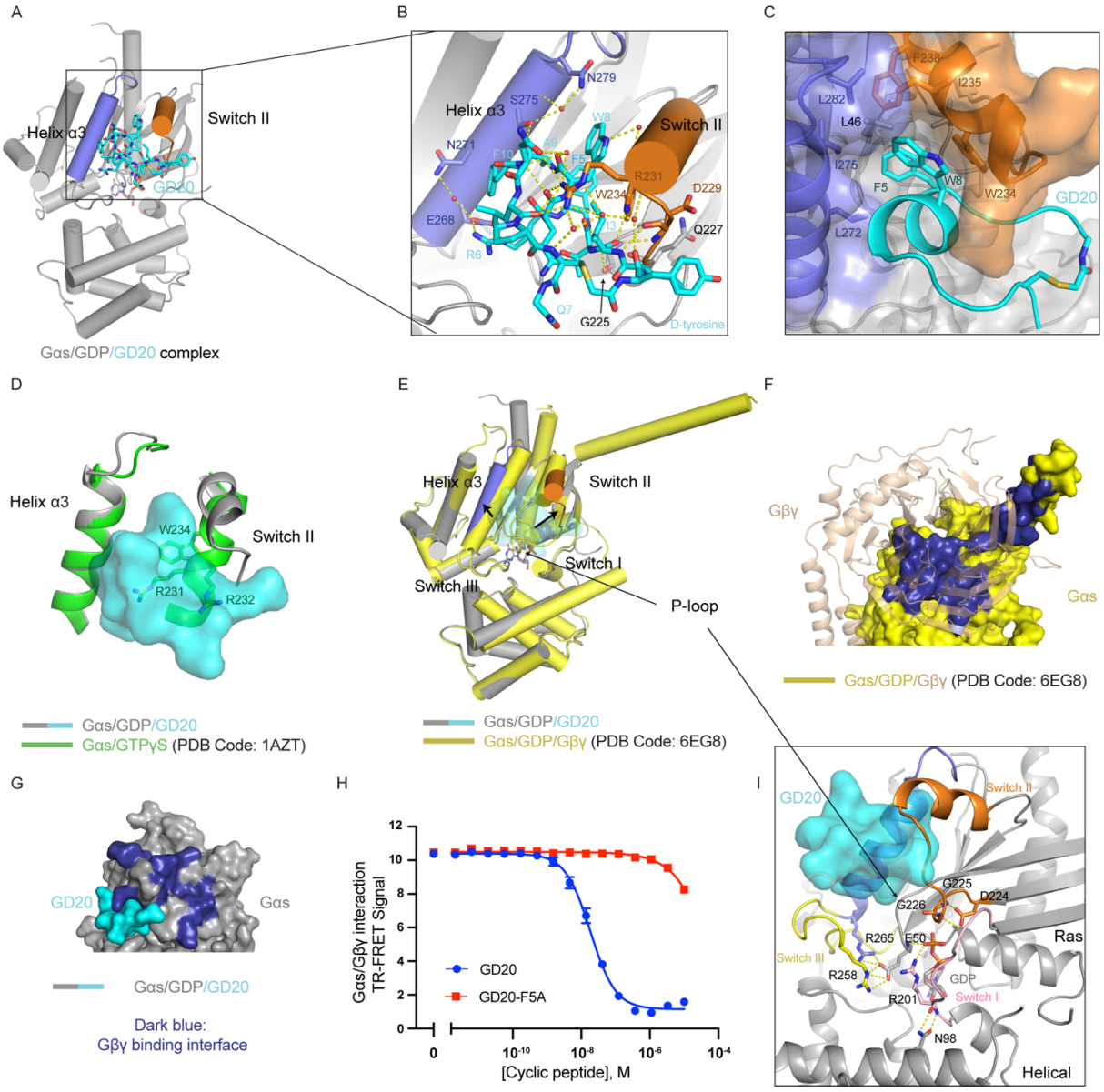

Figure 2.9 | The crystal structure of GDP-bound Gαs in complex with GD20. (**A**) Overall structure of the GD20/GDP/Gαs complex. GD20 (cyan) binds in between switch II (orange) and the α3 helix (slate). (**B**) Structural details of GD20/Gαs interaction. Ion pair and hydrogen bonds are represented by yellow dashed lines. (**C**) Close-up view of a hydrophobic pocket in Gαs that accommodates F5 and W8 of GD20 (cyan). Gαs residues that form the hydrophobic pocket are depicted as stick model. (**D**) Alignment of Gαs/GD20 complex structure (grey) with the structure of Gαs/GTPγS (green) in the switch II/α3 pocket (PDB: 1AZT). (**E**) Alignment of Gαs/GD20 complex structure (grey) with the structure of Gαs/GDP (yellow) in the crystal structure of Gαs/Gβ1/γ2 heterotrimer (PDB: 6EG8). Gβγ was hidden for clarity. (**F**) Structural details of the Gαs (yellow, surface) and Gβγ (wheat, cartoon) binding interface (dark blue) (PDB: 6EG8). (**G**) The Gβγ binding interface (dark blue) of Gαs is significantly rearranged when GD20 (cyan) binds to Gαs (grey). Gβγ was hidden for clarity. (H) GD20, but not GD20-F5A, inhibited protein-protein

interaction between Gαs/GDP and Gβγ(C68S). Mean ± SD, n = 3. (**I**) Close-up view of Gαs nucleotide binding pocket in our Gαs/GD20 complex structure. Residues that stabilize GDP binding are depicted as stick models. Hydrogen bonds are represented by yellow dashed lines.

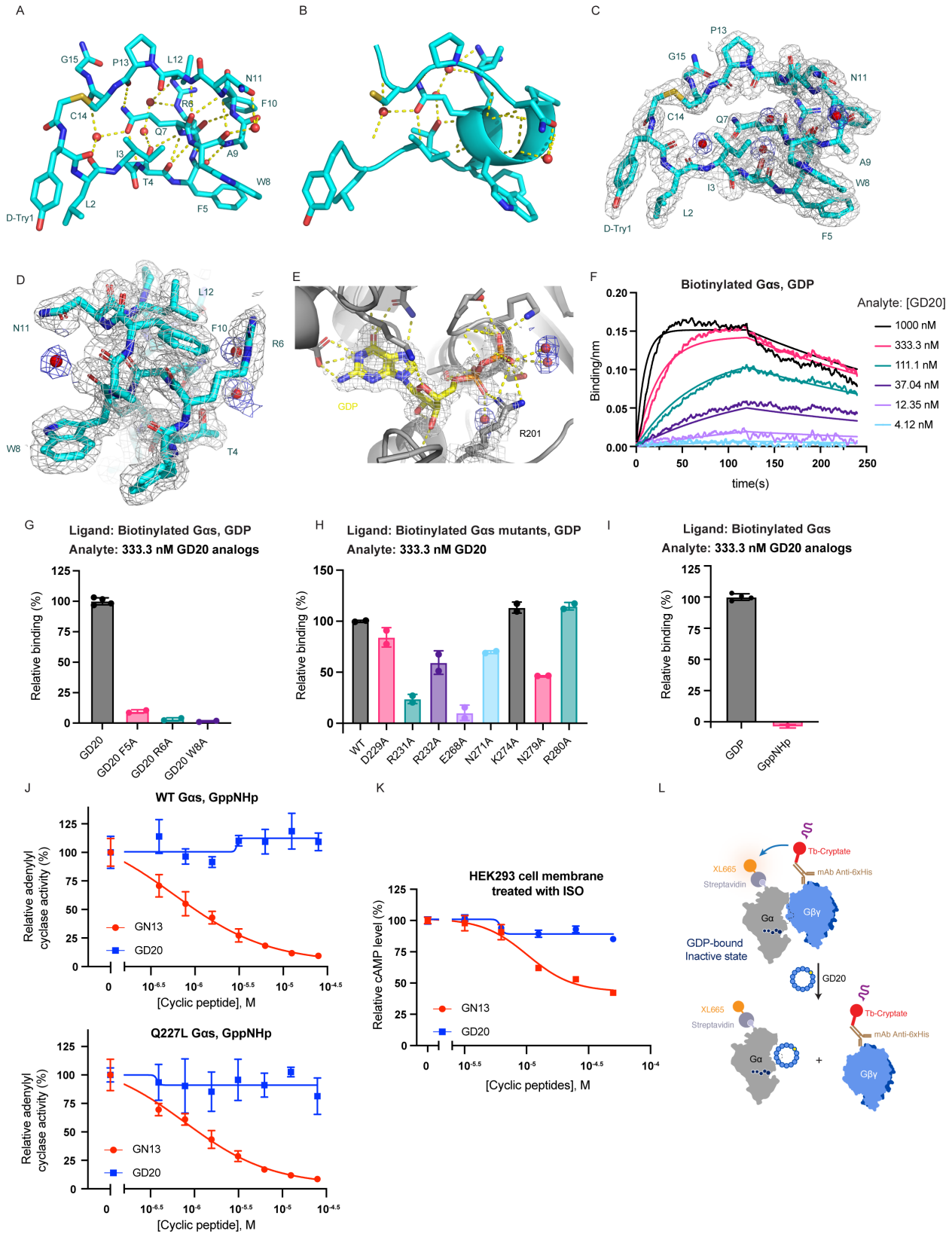
A
G15
P13
L12
N11
R6
F10
C14
Q7
I3
A9
T4
W8
L2
F5
D-Try1
B
C
P13
G15
N11
C14
Q7
A9
I3
W8
L2
D-Try1
F5
D
L12
N11
F10
R6
W8
T4
E
GDP
R201
F
Biotinylated Gαs, GDP
Analyte: [GD20]
1000 nM
333.3 nM
111.1 nM
37.04 nM
12.35 nM
4.12 nM
Binding/nm
time(s)
G
Ligand: Biotinylated Gαs, GDP
Analyte: 333.3 nM GD20 analogs
Relative binding (%)
GD20
GD20 F5A
GD20 R6A
GD20 W8A
H
Ligand: Biotinylated Gαs mutants, GDP
Analyte: 333.3 nM GD20
Relative binding (%)
WT
D229A
R231A
R232A
E268A
N271A
K274A
N279A
R280A
I
Ligand: Biotinylated Gαs
Analyte: 333.3 nM GD20 analogs
Relative binding (%)
GDP
GppNHp
J
WT Gαs, GppNHp
Relative adenylyl cyclase activity (%)
GN13
GD20
[Cyclic peptide], M
Q227L Gαs, GppNHp
Relative adenylyl cyclase activity (%)
GN13
GD20
[Cyclic peptide], M
K
HEK293 cell membrane treated with ISO
Relative cAMP level (%)
GN13
GD20
[Cyclic peptides], M
L
Tb-Cryptate
XL665
mAb Anti-6xHis
Streptavidin
Gα
Gβγ
GDP-bound
Inactive state
GD20

Figure 2.10 | GD20 specifically inhibits Gαs through binding to a crystallographically defined pocket. (**A** and **B**) GD20 adopts a highly ordered three-dimensional structure through intramolecular and intermolecular hydrogen bonding network. GD20 is shown as cyan sticks (A) or cartoon (B). Four water molecules with well-defined electron density are shown as red spheres. Hydrogen bonds are represented by yellow dash lines. (**C** and **D**) Electron density map of GD20. GD20 is shown as cyan sticks. Four water molecules with well-defined electron density are shown as red spheres. The 2mFo-DFc electron density map of the structure is contoured at 1.0 σ and colored grey (GD20) and blue (Water), respectively. (**E**) Electron density map of GDP. GDP and the side chain of R201 are shown as sticks. The Mg2+ and two water molecules coordinated with the Mg2+ are shown as green and red spheres, respectively. The 2mFo-DFc electron density map of the structure is contoured at 1.0 σ. (**F**) Binding kinetics of GD20 to WT GDP-bound Gαs were quantified using BLI. Biotinylated WT GDP-bound Gαs was immobilized to give a relative intensity of 2-3 nm on streptavidin biosensors, following the same association/dissociation cycles descried in Figure S2C. The assay was performed in duplicate, and the data represent one of the two replicates. (**G**) Binding of GD20 analogs to WT GDP-bound Gαs were quantified using BLI. Biotinylated WT GDP-bound Gαs proteins were immobilized to give a relative intensity of 2-3 nm on streptavidin biosensors, following the same association/dissociation cycles descried in Figure S2C. Binding signals were double referenced and normalized to WT Gαs loading and GD20/WT Gαs binding signal. The data represent the mean ± SD of two independent measurements. (**H**) Binding of GD20 to different GDP-bound Gαs mutants were quantified using BLI. Biotinylated GDP-bound Gαs proteins were immobilized to give a relative intensity of 2-3 nm on streptavidin biosensors, following the same association/dissociation cycles descried in Figure S2C. Binding signals were double referenced and normalized to Gαs loading and GDP/WT Gαs binding signal. The data represent the mean ± SD of two independent measurements. (**I**) Binding of GD20 analogs to WT GDP-bound or GNP-bound Gαs were quantified using BLI. Biotinylated WT Gαs proteins were immobilized to give a relative intensity of 2-3 nm on streptavidin biosensors, following the same association/dissociation cycles descried in Figure S2C. Binding signals were double referenced and normalized to Gαs loading and GD20/GDP-bound Gαs binding signal. The data represent the mean ± SD of two independent measurements. (**J**) Activation of AC by GNP-bound WT Gαs or GNP-bound Gαs oncogenic mutant Q227L were inhibited by GN13 but not GD20. The assay was performed as descried in Figure 2C. AC activity was normalized to DMSO control group (100%). The data represent the mean ± SD of three independent measurements. (**K**) GD20 did not inhibit ISO-stimulated Gαs activation. Cell membranes were prepared from HEK293 cells and were preincubated with GTP/GDP mixture (500/50μM) and various concentrations of GN13 or GD20 for 2hours, and then stimulated with 40 μM of β2AR agonist ISO. After adding ATP, the reaction was carried out at 30 °C for 30 min. Production of cAMP was evaluated by the LANCE Ultra cAMP kit. The data represent the mean ± SD of three independent replicates. (**L**) Schematic representation of inactive state binders inhibiting protein-protein interaction between biotinylated GDP-bound WT Gαs and His-tagged Gβγ(C68S).

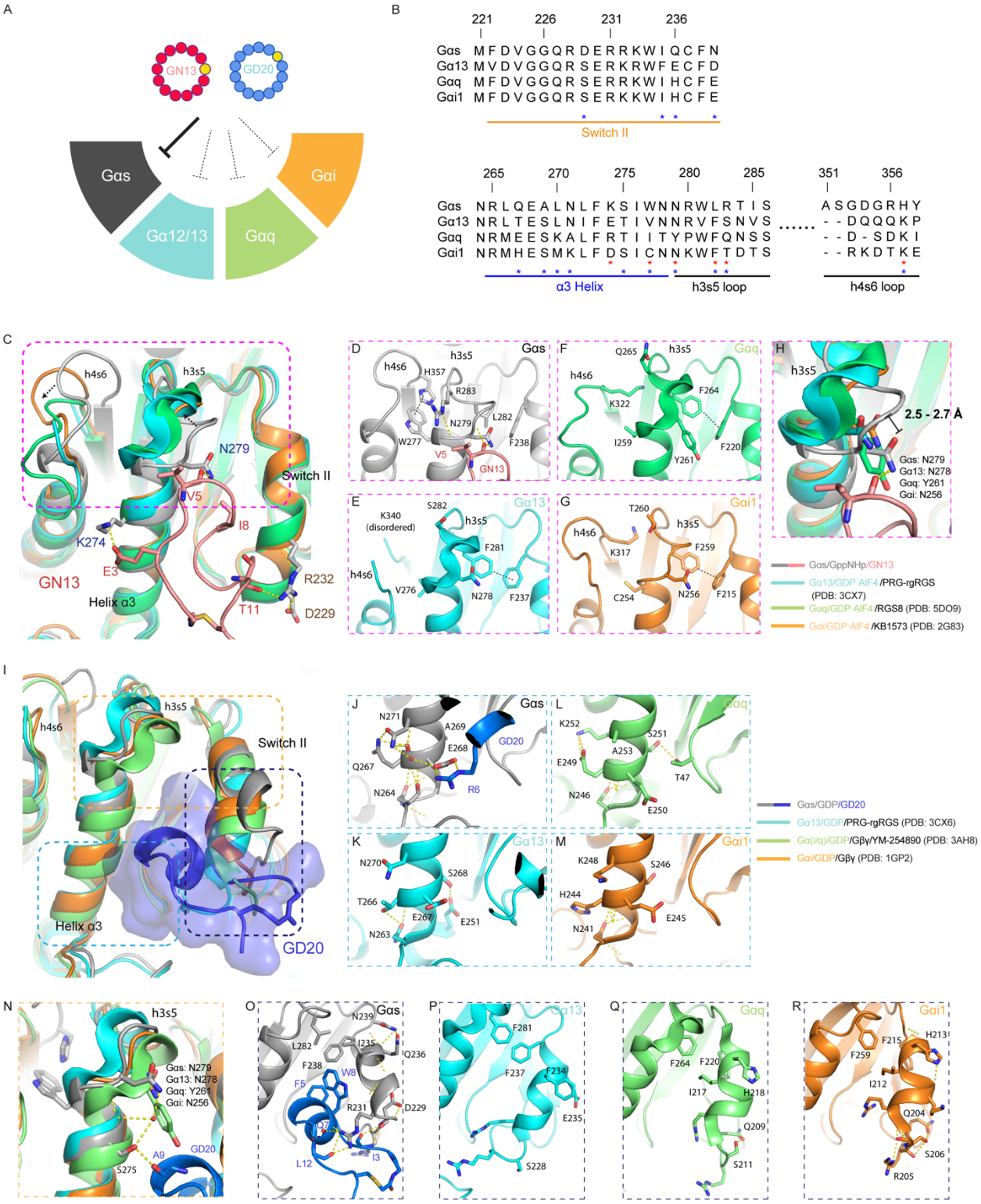

Figure 2.11 | G protein class-specificity of GN13 and GD20. (**A**) The Gαs targeting cyclic peptides, GN13 and GD20 did not bind Gα proteins from the other three Gα protein families.

(**B**) Sequence alignment of Gα proteins around the cyclic peptide binding site. The residue numbering is based on Gαs. Conserved structural motifs are indicated with colored lines. The residues that determine the specificity of GN13 (red) or GD20 (blue) are marked with asterisks. (**C**) The GDP-AlF4--bound active states of Gα13 (cyan, 3CX7), Gαq (green, 5DO9), and Gαi (orange, 2G83) from their complex structures were superimposed to Gαs/GNP in our Gαs (grey)/GN13 (salmon) complex. (**D-G**) Structural details of the GN13 binding pocket in four different active state Gα proteins. Gαs residues that are important for GN13 binding and homologous residues in Gα13, Gαq, and Gαi are depicted as stick models. Hydrogen bonds are represented by yellow dashed lines. (**H**) Close-up view of the critical N279 in Gαs/GNP. Homologous residues in Gα13, Gαq, and Gαi are labeled with different colors. The distances between the Cα of Gαs N279 and the Cα of other homologous residues are indicated. Hydrogen bonds are represented by yellow dashed lines. (**I**) The GDP-bound inactive states of Gα13 (cyan, 3CX6), Gαq (green, 3AH8), and Gαi (orange, 1GP2) from their complex structures were superimposed to Gαs/GDP in our Gαs (dark grey)/GD20 (blue) complex. (**J-M**) Structural details of the α3 helices in four different GDP-bound Gα proteins. Gαs residues that are important for GD20 binding and homologous residues in Gα13, Gαq, and Gαi are depicted as stick models. Hydrogen bonds are represented by yellow dashed lines. (**N**) Close-up view of the critical N279 in Gαs/GDP. Homologous residues in Gα13, Gαq, and Gαi are labeled with different colors. Hydrogen bonds are represented by yellow dashed lines. **(O-R**) Structural details of the switch II regions in four different GDP-bound Gα proteins. Gαs residues that are important for GD20 binding and homologous residues in Gα13, Gαq, and Gαi are depicted as stick models. Hydrogen bonds are represented by yellow dashed lines.

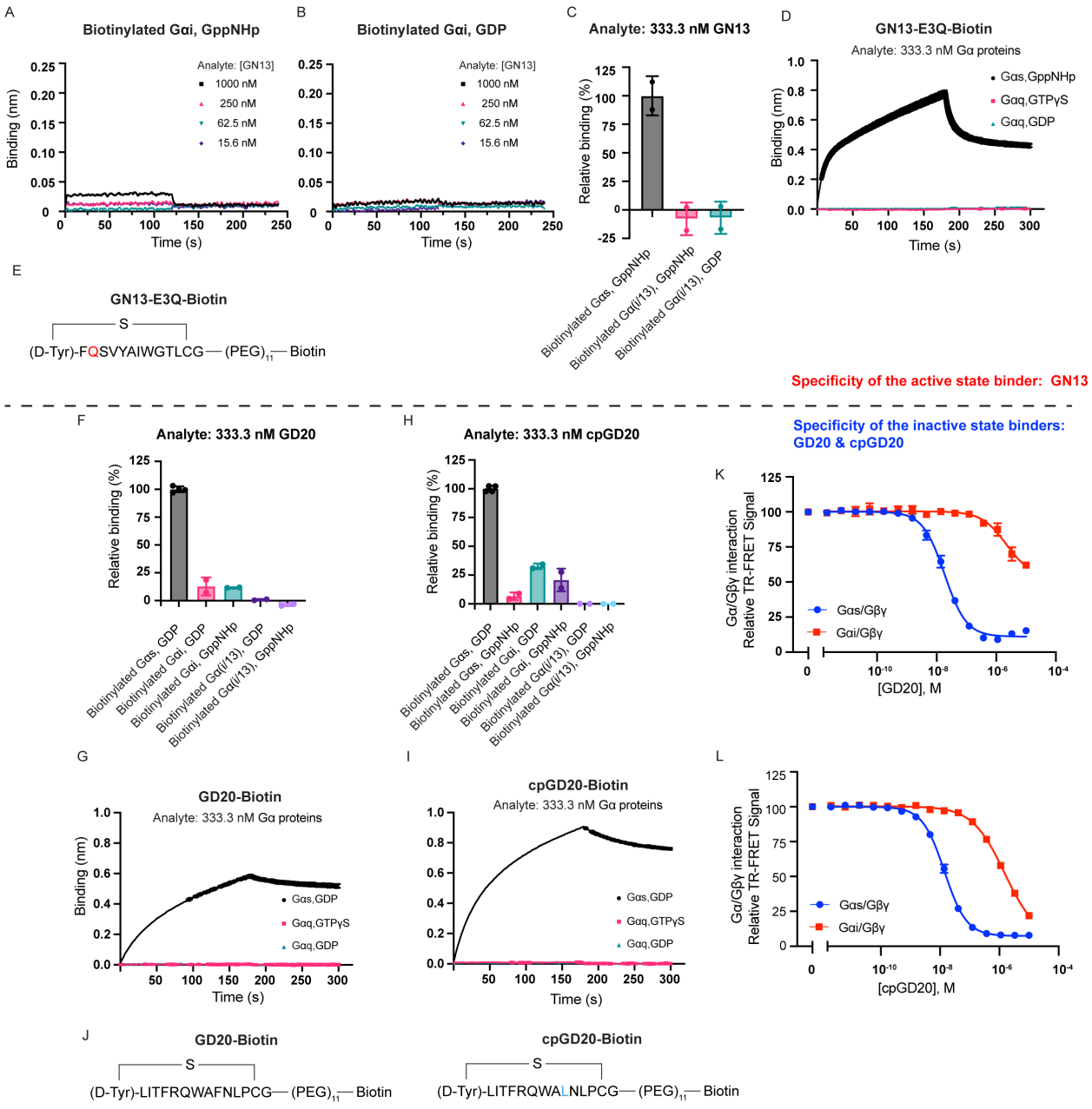

Figure 2.12 | G protein class-specificity of GN13 and GD20 is confirmed by biochemical characterizations. (**A-B**) Binding kinetics of GN13 to Gαi were quantified using BLI. Biotinylated Gαi proteins were immobilized to give a relative intensity of 2-3 nm on streptavidin biosensors, following the same association/dissociation cycles descried in Figure S2C. Binding signals were reference-subtracted. The assay was performed in duplicate, and the data represent one of the two replicates. (**C**) Binding of GN13 to Gαs and Gα(i/13) were quantified using BLI. The substitution of the N-terminal helix of Gαi1 for the corresponding region of Gα13 generated soluble chimeric Gα(i/13) protein. The N-terminal helix substitution is far away from GN13 binding interface, therefore will not influence its binding. Biotinylated Gα proteins were immobilized to give a relative intensity of 2-3 nm on streptavidin biosensors, following the same association/dissociation cycles descried in Figure S2C. Binding signals were double referenced

and normalized to Gα protein loading and GN13/GNP-bound Gαs binding signal. The data represent the mean ± SD of two independent measurements. (**D**) The Avi tagged Gαq was insoluble (data not shown), therefore, biotinylated GN13-E3Q was immobilized to give a relative intensity of 0.2-0.3 nm on streptavidin biosensors. GN13-E3Q was chosen to simplify chemical synthesis of biotinylated cyclic peptides. Binding kinetics of untagged Gαs and Gαq to immobilized GN13-E3Q were quantified using BLI. Association (t = 0-180 s) and dissociation (t = 180-300 s) cycles of Gα proteins were started by dipping sensors into Gα protein solutions and control buffer. Binding signals were double referenced. The data represent the mean ± SD of two independent measurements. (**E**) Design of biotinylated GN13-E3Q. (**F** and **H**) Binding of GD20 (F) or cpGD20 (H) to Gαs, Gα(i/13) and Gαi were quantified using BLI. Biotinylated Gα proteins were immobilized to give a relative intensity of 2-3 nm on streptavidin biosensors, following the same association/dissociation cycles descried in Figure S2C. Binding signals were double referenced and normalized to Gα protein loading and the GD20(or cpGD20)/GDP-bound Gαs binding signal. The data represent the mean ± SD of two independent measurements. (G and I) Biotinylated GD20 (G) or Biotinylated cpGD20 (**I**) was immobilized to give a relative intensity of 0.3-0.4 nm on streptavidin biosensors. Binding kinetics of untagged Gαs and Gαq to immobilized GD20 or cpGD20 were quantified using BLI. Association (t = 0-180 s) and dissociation (t = 180-300 s) cycles of Gα proteins were started by dipping sensors into Gα protein solutions and control buffer. Binding signals were double referenced. The data represent the mean ± SD of two independent measurements. (**J**) Design of biotinylated GD20 and biotinylated cpGD20. (**K**) GD20 inhibited protein-protein interaction between biotinylated GDP-bound Gαs WT and His-tagged Gβγ(C68S) in a dose-dependent manner. GD20 was 100-fold more selective for Gαs than Gαi. The data represent the mean ± SD of three independent replicates. (**L**) cpGD20 inhibited protein-protein interaction between biotinylated Gαs WT and His-tagged Gβγ(C68S) in a dose-dependent manner. cpGD20 was nearly 100-fold more selective for Gαs than Gαi. The data represent the mean ± SD of three independent replicates.

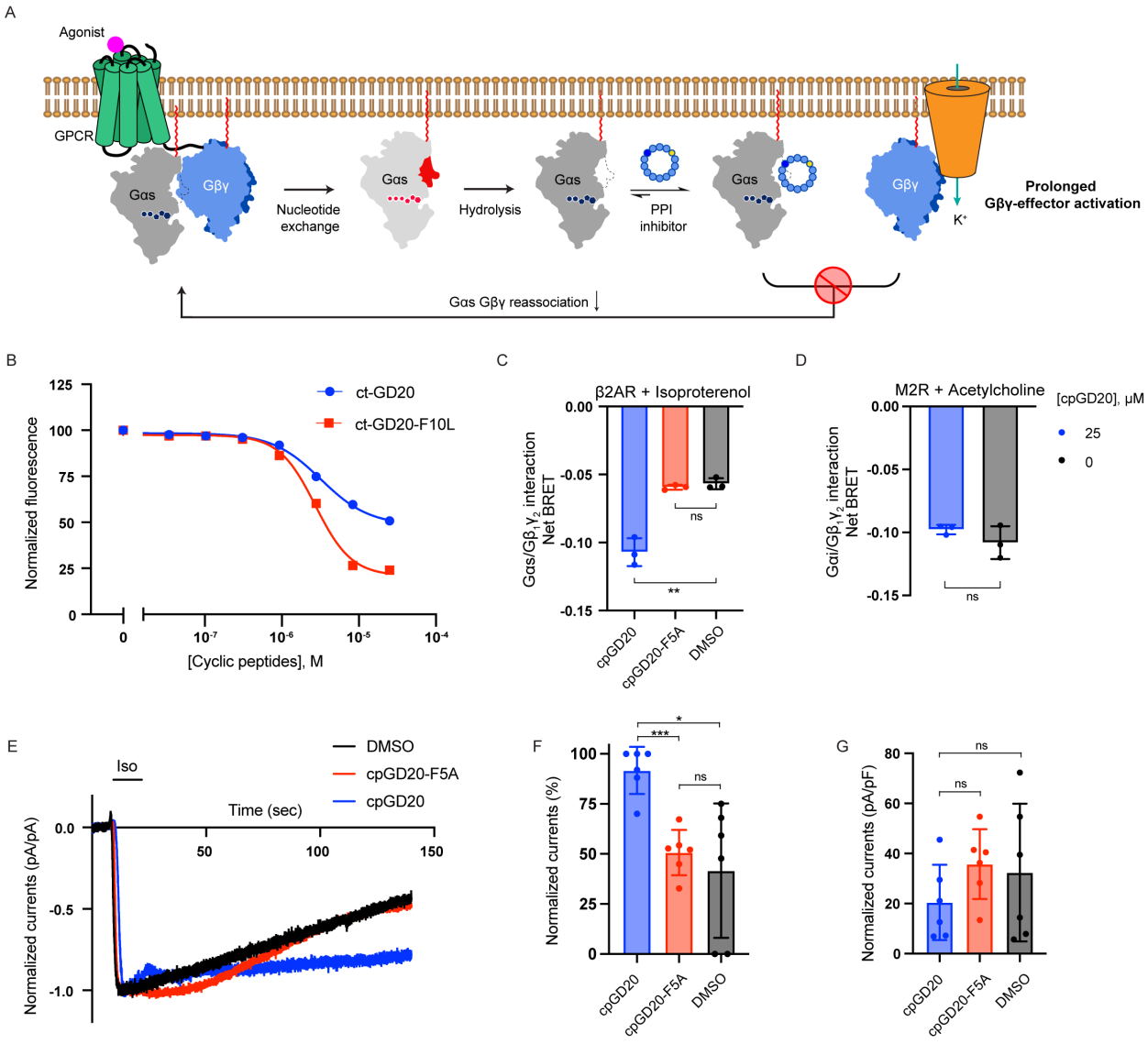

Figure 2.13 | A cell permeable GD20 analog, cpGD20, is a dual-effect G protein modulator. (**A**) Schematic representation of Gαs/Gβγ PPI inhibitors acting as dual-effect G protein modulators in cells. (**B**) CAPA cell permeability assay results of ct-GD20 (blue) and ct-GD20-F10L (red). Mean ± SD, n = 3. (**C**) 25 μM cpGD20, but not 25 μM cpGD20-F5A, inhibited Gαs/Gβγ reassociation in HEK293 cells transfected with β2AR, Gαs-RLuc8, Gβ1, and Gγ2-GFP2. Gαs/Gβγ dissociation was measured by BRET2 signal reduction after 10 nM ISO application. BRET2 signal was normalized to cells that were not treated with ISO. Mean ± SD, n = 3. Two-tailed unpaired t-tests were performed, *p < 0.05, **p < 0.01, ns p > 0.05. (**D**) cpGD20 did not inhibit Gαi/Gβγ reassociation in HEK293 cells transfected with M2R, Gαi1-RLuc8, Gβ1, and Gγ2-GFP2. Gαi1/Gβγ dissociation was measured by BRET2 signal reduction after 100 nM acetylcholine application. BRET2 signal was normalized to cells that were not treated with acetylcholine. Mean ± SD, n = 3. Two-tailed unpaired t-tests were performed, *p < 0.05, **p < 0.01, ns p > 0.05. (**E**) Representative voltage-clamp recordings of HEK293 cells transiently transfected with β2AR, GIRK4, Gβγ-Venus, and Gαs. Membrane potential was held at -80 mV. 1 μM ISO was applied as indicated. 25 μM of cpGD20, cpGD20-F5A, or DMSO were added to the pipette solution prior to

recordings. (**F**) The amounts of residual ISO-activated currents after 60 seconds of washout normalized to the maximum ISO-activated currents. 25 μM of cpGD20, cpGD20-F5A, or DMSO were added to the pipette solution prior to recordings. Mean ± SD, n = 6. Two-tailed unpaired t-tests with Welch's correction were performed, *$p < 0.05$, **$p < 0.01$, ***$p < 0.001$, ns $p > 0.05$. (**G**) Maximum ISO-activated currents normalized to the capacitance of the cells. 25 μM of cpGD20, cpGD20-F5A, or DMSO were added to the pipette solution prior to recordings. Mean ± SD, n = 6. Two-tailed unpaired t-tests with Welch's correction were performed, *$p < 0.05$, **$p < 0.01$, ns $p > 0.05$.

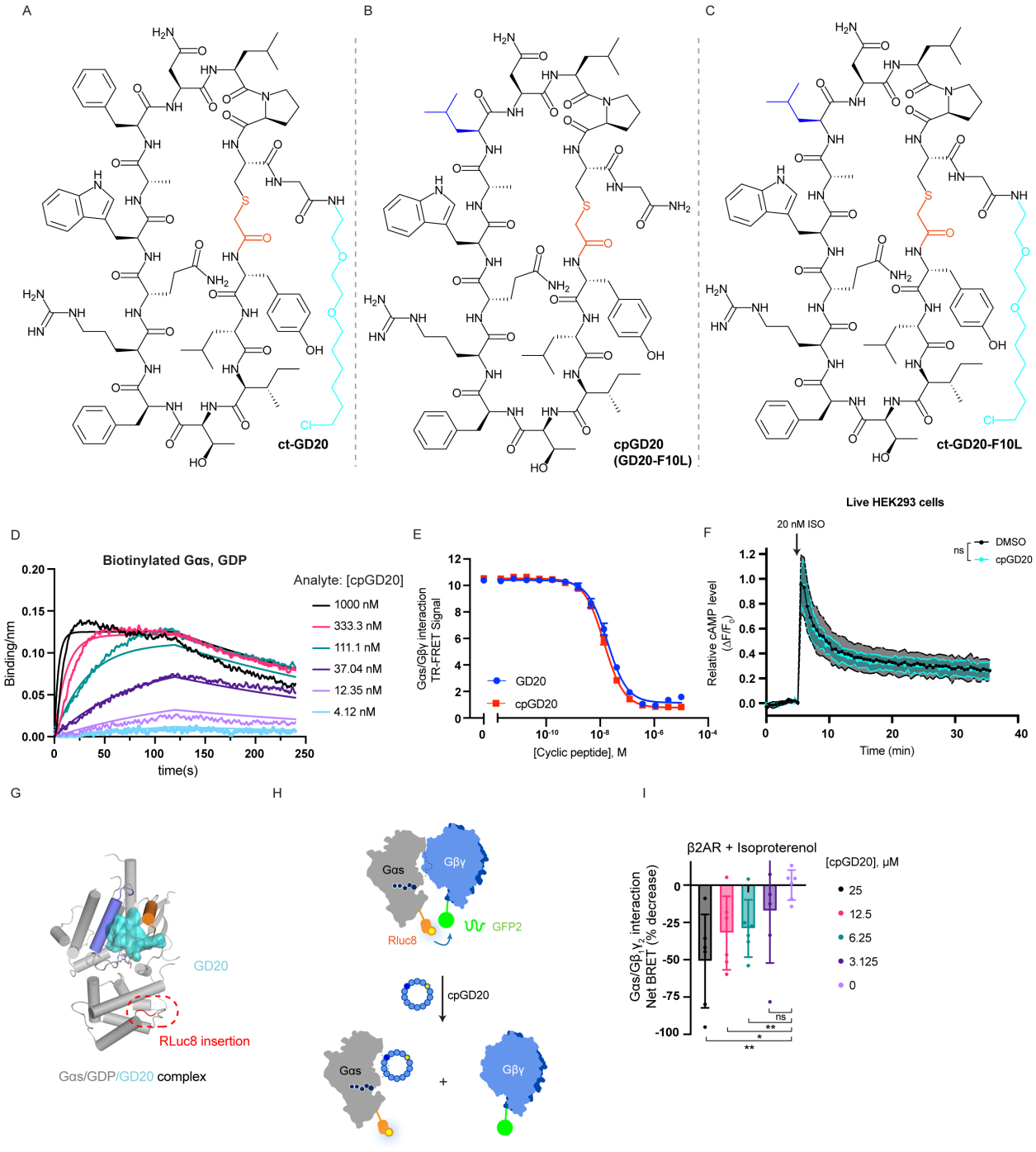

Figure 2.14 | A cell permeable GD20 analog, cpGD20, is a dual-effect G protein modulator. (**A** to **C**) Structure of derivatized cyclic peptides. (A) ct-GD20 (B) cpGD20 (GD20-F10L) (C) ct-GD20-F10L. (**D**) Binding kinetics of cpGD20 to WT GDP-bound Gαs were quantified using BLI. Biotinylated WT GDP-bound Gαs was immobilized to give a relative intensity of 2-3 nm on streptavidin biosensors, following the same association/dissociation cycles descried in Figure S2C. The assay was performed in duplicate, and the data represent one of the two replicates. (**E**) cpGD20 inhibited protein-protein interaction between biotinylated GDP-bound Gαs WT and His-tagged Gβγ(C68S) in a dose-dependent manner. The data represent the mean ± SD of three independent

replicates. (**F**) Real-time cAMP levels in HEK293 cells were measured using the Green Up cADDis cAMP biosensor after 24 hours of 25 μM cpGD20 treatment. The data represent the mean ± SD of three independent biological replicates. Each biological replicate represents the average of at least two technical replicates. Two-tailed unpaired t-tests were performed using data after 5min. $P < 0.05$ was considered significant. ns $p > 0.05$. (**G**) The GD20/Gαs complex structure provides structural basis for the Rluc8 insertion. Rluc8 is inserted between αB and αC helices. (G) Schematic representation of cpGD20 inhibiting protein-protein interaction between GαsShort_Rluc and Gβ1/GFP2_γ2 in a BRET2 assay. (**H**) HEK293 cells transfected with β2AR, Gαs-RLuc8, Gβ1, and Gγ2-GFP2 were pretreated with various concentrations of cpGD20 for 16hours. Gαs/Gβγ dissociation was measured by BRET2 signal reduction after 1 nM ISO application. BRET2 signal was normalized to cells that were not treated with ISO and the percentage decrease was calculated based on the net BRET2 signal at [cpGD20] = 0 μM. The data represent the mean ± SD of six biological replicates. Two-tailed unpaired t-tests were performed. $P < 0.05$ was considered significant. *$p < 0.05$, **$p < 0.01$, ns $p > 0.05$.

Table 2.1 | Key resources table.

REAGENT or RESOURCE	SOURCE	IDENTIFIER
Bacterial and virus strains		
Escherichia coli BL21(DE3)	Invitrogen	Cat# C600003
MAX Efficiency DH10Bac Competent Cells	Thermo Fisher Scientific	Cat# 10361012
Chemicals, peptides, and recombinant proteins		
GDP	Sigma-Aldrich	Cat# G7127-100MG
GTP	Sigma-Aldrich	Cat# 11140957001
ATP	Discoverx	Cat# 90-0099
Guanosine 5'-[β,γ-imido]triphosphate (GNP, GppNHp)	Axorra	Cat# JBS-NU-401-50
100X GTPγS, 10mM	EMD Millipore	Cat# 20-176
Guanosine 5'-Diphosphate, Trisodium Salt, [8,50-3H]-, Specific Activity: 25-50Ci (0.925-1.85TBq)/mMole, 250 µCi (9.25MBq)	Perkin-Elmer	Cat# NET966250UC
GTP, [γ-32P]- 6000Ci/mmol 10mCi/ml Lead, 250 µCi	Perkin-Elmer	Cat# NEG004Z250UC
GTPγS, [35S]- 1250Ci/mmol, 12.5mCi/ml, 250 µCi	Perkin-Elmer	Cat# NEG030H250UC
Forskolin	Cayman Chemical Company	Cat# 11018: 50 mg
Isoproterenol Hydrochloride	TCI	Cat# I0260
Acetylcholine Chloride	Selleckchem	Cat# S1805
Activated Charcoal Norit	Sigma-Aldrich	Cat# 53663-250G
Cytoscint-ES liquid scintillation cocktail	MP Biomedicals	Cat# 0188245301
Acrylonitrile	Sigma-Aldrich	Cat# 110213-5ML
cOmplete Protease Inhibitor Cocktail	Sigma-Aldrich	Cat# 5056489001
Carbenicillin	Goldbio	Cat# C-103-100
Kanamycin	Goldbio	Cat# K-120-25
IPTG	Goldbio	Cat# I2481C100
DTT	Goldbio	Cat# DTT10
Biotin	Sigma-Aldrich	Cat# B4501-5G
M-MLV reverse transcriptase	Promega	Cat# 3683
acetylated BSA	Nacalai Tesque	Cat# 01278-44
TrypLE™ Express Enzyme (1X), no phenol red	Fisher Scientific	Cat# 12604013
PBS, pH 7.4	Thermo Fisher Scientific	Cat# 10010049
3-Isobutyl-1-methylxanthine, BioUltra, >=99% (IBMX)	Sigma-Aldrich	Cat# I7018
DMSO sterile filtered	Sigma-Aldrich	Cat# D2650
ct-TAMRA	Promega	Cat# G8251
Coelenterazine-400a (Nanolight Technology)	Prolume Ltd	Cat# 340-1
Bovine Serum Albumin (BSA), Fraction V, low Heavy Metals	EMD Millipore	Cat# 12659-100GM
Critical commercial assays		
LANCE Ultra cAMP Detection Kit	Perkin-Elmer	Cat# TRF0263
GTPase Colorimetric Assay Kit 480 Tests	Innova Biosciences	Cat# 602-0121
Pierce™ BCA® Protein Assay Kits and Reagents, Thermo Scientific, BCA	Fisher Scientific	Cat# PI23227
Streptavidin XL665	Cisbio	Cat# 610SAXLF
Anti-6His-Tb cryptate	Cisbio	Cat# 61HI2TLF
Green Up cADDis cAMP Assay Kit	Montana Molecular	Cat# U0200G
Deposited data		

REAGENT or RESOURCE	SOURCE	IDENTIFIER
GppNHp-bound Gαs in complex with the cyclic peptide inhibitor GN13	This paper	7BPH
GDP-bound Gαs in complex with the cyclic peptide inhibitor GD20	This paper	7E5E
Experimental models: Cell lines		
Sf9 cells	Thermo Fisher Scientific	Cat# 12659017
Halo-Tag-GFP-Mito expressing HeLa cells	J. Kritzer (Tufts University) (Peraro et al., 2018)	N/A
HEK293 cells	ATCC	Cat# CRL-1573
(Parent) HEK293 cells	A. Inoue (Tohoku University) (Stallaert et al., 2017)	N/A
GNAS KO HEK293 cells (CL4)	A. Inoue (Tohoku University) (Stallaert et al., 2017)	N/A
Recombinant DNA		
Gαs(WT) cloned into a modified pET15b vector	Hu et al., 2018	N/A
Gαs(Q227L) cloned into a modified pET15b vector	This study	N/A
Human ADCY2 (residues 871-1082) cloned into a modified pET15b vector	Hu et al., 2018	N/A
Mouse ADCY5(D628E/S645R) (residues 443-659) cloned into a pET29b vector	Hu et al., 2018	N/A
Human GNB1(WT) and GNG2(C68S) cloned into a modified pFastBac Dual vector	Hu et al., 2018	N/A
Avi-Gαs(WT) cloned into a modified pET15b vector	This study	N/A
Avi-Gαi1(WT) cloned into a modified pET15b vector	This study	N/A
Avi-Gαs(S275L) cloned into a modified pET15b vector	This study	N/A
pcDNA3 Gαs(WT)-HA	This study	N/A
pcDNA3 Gαs(S275L)-HA	This study	N/A
pcDNA3 Gαsi1(WT)-EE-tagged	G. Peng (UCSF)	N/A
SSF-β2AR	B. Barsi-Rhyne (UCSF)	N/A
pCEH-Sero-SNAP-hM2R	R. Mackinnon (The Rockefeller University)	N/A
Gβ1-C Venus	R. Mackinnon (The Rockefeller University)	N/A
Gγ2-N Venus	R. Mackinnon (The Rockefeller University)	N/A
GIRK4-NLuc	R. Mackinnon (The Rockefeller University)	N/A
pcDNA3.1-Beta1	Olsen et al., 2020	Addgene plasmid # 140987
pcDNA3.1-GGamma1-GFP2	Olsen et al., 2020	Addgene plasmid # 140989
pcDNA3.1-GGamma2-GFP2	This paper	N/A
pcDNA5/FRT/TO-GAlphai1-RLuc8	Olsen et al., 2020	Addgene plasmid # 140973
pcDNA5/FRT/TO-GAlphasS-RLuc8	Olsen et al., 2020	Addgene plasmid # 140980
Software and algorithms		
Powerpoint	Microsoft	www.microsoft.com

REAGENT or RESOURCE	SOURCE	IDENTIFIER
GraphPad Prism	GraphPad Software	https://www.graphpad.com/ scientific-software/prism/
CCP4	Winn et al., 2011	http://www.ccp4.ac.uk/
Phenix	Adams et al., 2010	https://www.phenix-online.org/
Coot	Emsley et al., 2010	https://www2.mrc-lmb.cam.ac.uk/personal/pemsley/coot/
Excel	Microsoft	https://www.microsoft.com/en-us/
Word	Microsoft	https://www.microsoft.com/en-us/
Illustrator 2022	Adobe	https://www.adobe.com/products/illustrator.html
Pymol	The PyMOL Molecular Graphics System, Version 1.8 Schro¨dinger, LLC.	https://pymol.org/2/
UCSF Chimera	Pettersen et al., 2004	https://www.cgl.ucsf.edu/chimera
Other		
TALON Metal Affinity Resin	Clontech Laboratories	Cat# 635503
SOURCE 15Q, 200 ml	GE Healthcare	Cat# 17-0947-05
Superdex 200 Increase 10/300 GL	GE Healthcare	Cat# 28-9909-44
Sephadex G-25	GE Healthcare	Cat# 17003201
Dynabeads M280 streptavidin magnetic beads	Thermo Fisher Scientific	Cat# 11206D
Transit 2020	Fisher Scientific	Cat# MIR5404
Lipofectamine 2000 Transfection Reagent	Thermo Fisher Scientific	Cat# 11668019
Opti-MEM™ I Reduced Serum Medium	Fisher Scientific	Cat# 31-985-062
Mixed cellulose membrane	EMD Millipore	Cat# GSWP02500
Streptavidin biosensors	Molecular Devices	Cat# 18-5019
Sf-900 III SFM	Thermo Fisher Scientific	Cat# 12658027
OptiPlate-384, White Opaque 384-well Microplate	PerkinElmer	Cat# 6007290
Greiner 384well, black, flat bottom polypropylene plates	Millipore Sigma	Cat# M1937-32EA
96-well Flat Clear Bottom Black Polystyrene Microplates	Corning	Cat# 3340
poly-D-lysine-coated white, clear-bottom 96-well assay plates	Greiner Bio-One	Cat# 655944
White Adhesive Bottom Seal	Perkin Elmer	Cat# 6005199
Dounce tissue grinder set	Millipore Sigma	Cat# D8938-1SET
Spark 20 M plate reader	TECAN	N/A
Synergy H4 Hybrid Microplate Reader	BioTek	N/A
Octet RED384	ForteBio	N/A
LS 6500 Multi-Purpose Scintillation Counter	Beckman Coulter	N/A
Axopatch 200B amplifier	Molecular Devices	N/A
Digidata 1550B digitizer	Molecular Devices	N/A
Sutter P-97 puller	Sutter Instrument Company	N/A
Syro Wave automated peptide synthesizer	Biotage	N/A

Table 2.2 | Data collection and refinement statistics for the Gαs/GppNHp/GN13 complex.

[a] Values in parentheses are for highest-resolution shell.

	Gαs/GppNHp/GN13 complex
Data collection	
Space group	P 21 21 21
Cell dimensions	
a, *b*, *c* (Å)	68.905, 78.332, 80.043
α, *β*, *γ* (°)	90, 90, 90
Resolution (Å)	50.00-1.57 (1.60-1.57)[a]
R_{merge}, R_{meas}, and R_{pim}	0.074 (1.040), 0.086 (0.972), 0.023 (0.405)
$I/\sigma(I)$	27.3 (1.32)
$CC_{1/2}$	0.997 (0.783)
Completeness (%)	96.9 (71.2)
Total reflections	58703
Unique reflections	57627
Redundancy	12.4 (4.0)
Refinement	
Resolution (Å)	43.45-1.574
No. reflections	51161
R_{work}	0.1970
R_{free}	0.2291
No. atoms	
Protein	3079
Ligand/ion (specify/describe)	44
Water	132
B factors	
Protein	21.98
Ligand/ion	13.41
Water	22.43
R.m.s. deviations	
Bond lengths (Å)	0.014
Bond angles (°)	1.39
Ramachandran analysis	
Favored (%)	98.91
Allowed (%)	0.82
Outliers (%)	0.27
Rotamer outliers (%)	0.60
Clashscore	3.57

Table 2.3 | Data collection and refinement statistics for the Gαs/GDP/GD20 complex.

[a] Values in parentheses are for highest-resolution shell.

	Gαs/GDP/GD20 complex
Data collection	
Space group	P1
Cell dimensions	
a, *b*, *c* (Å)	58.105, 81.771, 76.912
α, *β*, *γ* (°)	81.266, 83.844, 90.698
Resolution (Å)	50.00-1.95 (1.98-1.95)[a]
R_{merge}, R_{meas}, and R_{pim}	0.081 (1.202), 0.113 (1.260), 0.059 (0.762)
$I/\sigma(I)$	11.40 (0.815)
$CC_{1/2}$	0.991 (0.422)
Completeness (%)	97.0 (87.7)
Total reflections	99153
Unique reflections	95974
Redundancy	3.4 (2.0)
Refinement	
Resolution (Å)	48.54-1.95
No. reflections	82224
R_{work}	0.2178
R_{free}	0.2580
No. atoms	
Protein	11279
Ligand/ion	132
Water	329
B factors	
Protein	29.36
Ligand/ion	18.22
Water	21.27
R.m.s. deviations	
Bond lengths (Å)	0.004
Bond angles (°)	0.70
Ramachandran analysis	
Favored (%)	97.45
Allowed (%)	2.25
Outliers (%)	0.30
Rotamer outliers (%)	0.98
Clashscore	3.86

Table 2.4 | Kinetics analysis of cyclic peptides-Gαs interaction by BLI.

	K_D (nM)	K_{on} ($M^{-1}s^{-1}$)	K_{off} (s^{-1})
GN13/GppNHp/Gαs	190 ± 16	$2.71 \times 10^5 \pm 2.13 \times 10^4$	$5.13 \times 10^{-2} \pm 1.31 \times 10^{-3}$
GD20/GDP/Gαs	31.4 ± 0.7	$1.09 \times 10^5 \pm 1.28 \times 10^3$	$3.43 \times 10^{-3} \pm 6.97 \times 10^{-5}$
cpGD20/GDP/Gαs	14.5 ± 0.4	$2.47 \times 10^5 \pm 3.71 \times 10^3$	$3.58 \times 10^{-3} \pm 8.50 \times 10^{-5}$

Table 2.5 | Chemical stability of Gαs binding cyclic peptides in DMEM with 10% FBS.

[a] Values represent 95% confidence intervals
The data were analyzed from two independent replicates.

	Half-life (hour) [a]
GN13	>76
GD20	>142
cpGD20	37.37 - 50.32

Table 2.6 | Plasma stability of Gαs binding cyclic peptides.

[a] Values represent 95% confidence intervals
The data were analyzed from two independent replicates.

	Half-life (hour) [a]
GN13	>82
GD20	16.37 - 27.13
cpGD20	7.16 - 12.74

References

Adams, P.D., Afonine, P. v., Bunkóczi, G., Chen, V.B., Davis, I.W., Echols, N., Headd, J.J., Hung, L.W., Kapral, G.J., Grosse-Kunstleve, R.W., et al. (2010). PHENIX: A comprehensive Python-based system for macromolecular structure solution. Acta Crystallogr. D Biol. Crystallogr. 66, 213–221.

Alessi, D.R., and Sammler, E. (2018). LRRK2 kinase in Parkinson's disease. Science 360, 36–37.

Austin, R.J., Ja, W.W., and Roberts, R.W. (2008). Evolution of Class-Specific Peptides Targeting a Hot Spot of the Gαs Subunit. J. Mol. Biol. 377, 1406–1418.

Bechara, C., & Sagan, S. (2013). Cell-penetrating peptides: 20 years later, where do we stand?. FEBS Lett., 587, 1693-1702.

Bonacci, T.M., Mathews, J.L., Yuan, C., Lehmann, D.M., Malik, S., Wu, D., Font, J.L., Bidlack, J.M. and Smrcka, A.V., 2006. Differential targeting of Gβγ-subunit signaling with small molecules. Science 312, 443-446.

Canon, J., Rex, K., Saiki, A.Y., Mohr, C., Cooke, K., Bagal, D., Gaida, K., Holt, T., Knutson, C.G., Koppada, N., et al. (2019). The clinical KRAS(G12C) inhibitor AMG 510 drives anti-tumour immunity. Nature 575, 217–223.

Chang, F. H., & Bourne, H. R. (1989). Cholera toxin induces cAMP-independent degradation of Gs. J. Biol. Chem., 264, 5352-5357.

Chen, Z., Singer, W.D., Sternweis, P.C., and Sprang, S.R. (2005). Structure of the p115RhoGEF rgRGS domain-Gα13/i1 chimera complex suggests convergent evolution of a GTPase activator. Nat. Struct. Mol. Biol. 12, 191–197.

Chen, Z., Singer, W. D., Danesh, S. M., Sternweis, P. C., & Sprang, S. R. (2008). Recognition of the activated states of Gα13 by the rgRGS domain of PDZRhoGEF. Structure, 16, 1532-1543.

Dougherty, P.G., Sahni, A., and Pei, D. (2019). Understanding Cell Penetration of Cyclic Peptides. Chem. Rev. 119, 10241–10287.

Dror, R.O., Mildorf, T.J., Hilger, D., Manglik, A., Borhani, D.W., Arlow, D.H., Philippsen, A., Villanueva, N., Yang, Z., Lerch, M.T., et al. (2015). Structural basis for nucleotide exchange in heterotrimeric G proteins. Science 348, 1361–1365.

Emsley, P., Lohkamp, B., Scott, W.G., and Cowtan, K. (2010). Features and development of Coot. Acta Crystallogr. D Biol. Crystallogr. 66, 486–501.

Evans, P. (2006). Scaling and assessment of data quality. In Acta Crystallogr. D Biol. Crystallogr., pp. 72–82.

Ghosh, P., Rangamani, P., and Kufareva, I. (2017). The GAPs, GEFs, GDIs and…now, GEMs: New kids on the heterotrimeric G protein signaling block. Cell Cycle 16, 607–612.

Goto, Y., Katoh, T., and Suga, H. (2011). Flexizymes for genetic code reprogramming. Nat Protoc. 6, 779–790.

Gulati, S., Jin, H., Masuho, I., Orban, T., Cai, Y., Pardon, E., Martemyanov, K.A., Kiser, P.D., Stewart, P.L., Ford, C.P. and Steyaert, J., (2018). Targeting G protein-coupled receptor signaling at the G protein level with a selective nanobody inhibitor. Nat. Commun. 9, 1-15.

Hallin, J., Engstrom, L.D., Hargi, L., Calinisan, A., Aranda, R., Briere, D.M., Sudhakar, N., Bowcut, V., Baer, B.R., Ballard, J.A., et al. (2020). The KRASG12C inhibitor MRTX849

provides insight toward therapeutic susceptibility of KRAS-mutant cancers in mouse models and patients. Cancer Discov. 10, 54–71.

Hu, Q., and Shokat, K.M. (2018). Disease-Causing Mutations in the G Protein Gαs Subvert the Roles of GDP and GTP. Cell 173, 1254-1264.e11.

Ja, W.W., and Roberts, R.W. (2004). In vitro selection of state-specific peptide modulators of G protein signaling using mRNA display. Biochemistry 43, 9265–9275.

Ja, W.W., Wiser, O., Austin, R.J., Jan, L.Y., and Roberts, R.W. (2006). Turning G proteins on and off using peptide ligands. ACS Chem. Biol. 1, 570–574.

Johnston, C.A., Willard, F.S., Jezyk, M.R., Fredericks, Z., Bodor, E.T., Jones, M.B., Blaesius, R., Watts, V.J., Harden, T.K., Sondek, J., et al. (2005). Structure of Gαi1 bound to a GDP-selective peptide provides insight into guanine nucleotide exchange. Structure 13, 1069–1080.

Johnston, C.A., Ramer, J.K., Blaesius, R., Fredericks, Z., Watts, V.J., and Siderovski, D.P. (2005). A bifunctional Gαi /Gαs modulatory peptide that attenuates adenylyl cyclase activity. FEBS Letters. 579, 5746–5750

Johnston, C.A., Lobanova, E.S., Shavkunov, A.S., Low, J., Ramer, J.K., Blaesius, R., Fredericks, Z., Willard, F.S., Kuhlman, B., Arshavsky, V.Y. and Siderovski, D.P., (2006). Minimal Determinants for Binding Activated Gα from the Structure of a Gαi1− Peptide Dimer. Biochemistry 45, 11390-11400.

Kaur, H., Harris, P.W.R., Little, P.J., and Brimble, M.A. (2015). Total synthesis of the cyclic depsipeptide YM-280193, a platelet aggregation inhibitor. Org. Lett. 17, 492–495.

Kreutz, B., Yau, D. M., Nance, M. R., Tanabe, S., Tesmer, J. J., & Kozasa, T. (2006). A new approach to producing functional Gα subunits yields the activated and deactivated structures of Gα12/13 proteins. Biochemistry, 45, 167-174.

Lambright, D.G., Noel, J.P., Hammt Be, H.E., and Sigler, P.B. (1994). Structural determinants for activation of the alpha-subunit of a heterotrimeric G protein. Nature 369, 621–628.

Liu, X., Xu, X., Hilger, D., Aschauer, P., Tiemann, J.K., Du, Y., Liu, H., Hirata, K., Sun, X., Guixà-González, R., Mathiesen, J.M., et al. (2019). Structural insights into the process of GPCR-G protein complex formation. Cell 177, 1243-1251.

Manglik, A., Kobilka, B. K., & Steyaert, J. (2017). Nanobodies to study G protein-coupled receptor structure and function. Annu. Rev. Pharmacol. Toxicol, 57, 19.

Maziarz, M., Park, J.C., Leyme, A., Marivin, A., Garcia-Lopez, A., Patel, P.P., and Garcia-Marcos, M. (2020). Revealing the Activity of Trimeric G-proteins in Live Cells with a Versatile Biosensor Design. Cell 182, 770-785.e16.

McCoy, A.J., Grosse-Kunstleve, R.W., Adams, P.D., Winn, M.D., Storoni, L.C., and Read, R.J. (2007). Phaser crystallographic software. J Appl Crystallogr. 40, 658–674.

Morimoto, J., Hayashi, Y., and Suga, H. (2012). Discovery of macrocyclic peptides armed with a mechanism-based warhead: Isoform-selective inhibition of human deacetylase SIRT2. Angew Chem Int Ed Engl. 51, 3423–3427.

Murakami, H., Saito, H., and Suga, H. (2003). A Versatile tRNA Aminoacylation Catalyst Based on RNA. Chem Biol. 10, 655–662.

Murakami, H., Ohta, A., Ashigai, H., and Suga, H. (2006). A highly flexible tRNA acylation method for non-natural polypeptide synthesis. Nat Methods. 3, 357–359.

Neklesa, T.K., Tae, H.S., Schneekloth, A.R., Stulberg, M.J., Corson, T.W., Sundberg, T.B., Raina, K., Holley, S.A., and Crews, C.M. (2011). Small-molecule hydrophobic tagging-induced degradation of HaloTag fusion proteins. Nat. Chem. Biol. 7, 538–543.

Nishimura, A., Kitano, K., Takasaki, J., Taniguchi, M., Mizuno, N., Tago, K., Hakoshima, T., Itoh, H., and Gilman, A.G. (2010). Structural basis for the specific inhibition of heterotrimeric Gq protein by a small molecule. Proc. Natl. Acad. Sci. U.S.A. 107, 13666–13671.

O'Hayre, M., Vázquez-Prado, J., Kufareva, I., Stawiski, E.W., Handel, T.M., Seshagiri, S., and Gutkind, J.S. (2013). The emerging mutational landscape of G proteins and G-protein-coupled receptors in cancer. Nat. Rev. Cancer. 13, 412–424.

Olsen, R.H.J., DiBerto, J.F., English, J.G., Glaudin, A.M., Krumm, B.E., Slocum, S.T., Che, T., Gavin, A.C., McCorvy, J.D., Roth, B.L., et al. (2020). TRUPATH, an open-source biosensor platform for interrogating the GPCR transducerome. Nat. Chem. Biol. 16, 841–849.

Otwinowski, Z., and Minor, W. (1997). [20] Processing of X-ray diffraction data collected in oscillation mode. In Methods in enzymology (Vol. 276, pp. 307-326). Academic press.

Passioura, T., and Suga, H. (2017). A RaPID way to discover nonstandard macrocyclic peptide modulators of drug targets. Chem. Commun. (Camb.). 53, 1931–1940.

Peraro, L., Deprey, K.L., Moser, M.K., Zou, Z., Ball, H.L., Levine, B., and Kritzer, J.A. (2018). Cell Penetration Profiling Using the Chloroalkane Penetration Assay. J. Am. Chem. Soc. 140, 11360–11369.

Prior, I.A., Lewis, P.D., and Mattos, C. (2012). A comprehensive survey of ras mutations in cancer. Cancer Res. 72, 2457–2467.

Ramaswamy, K., Saito, H., Murakami, H., Shiba, K., and Suga, H. (2004). Designer ribozymes: Programming the tRNA specificity into flexizyme. J Am Chem Soc. 126, 11454–11455.

Rasmussen, S.G., DeVree, B.T., Zou, Y., Kruse, A.C., Chung, K.Y., Kobilka, T.S., Thian, F.S., Chae, P.S., Pardon, E., Calinski, D. et al. 2011. Crystal structure of the β2 adrenergic receptor–Gs protein complex. Nature, 477, 549-555.

Seifert, R., Wenzel-Seifert, K., Lee, T. W., Gether, U., Sanders-Bush, E., & Kobilka, B. K. (1998). Different effects of Gaa splice variants on b2-adrenoreceptor-mediated The b2-adrenoreceptor coupled to the long splice variant of Gaa has properties of a constitutively active receptor. J. Biol. Chem., 273, 5109-5116.

Slep, K.C., Kercher, M.A., Hek, W., Cowan, C.W., Wenselk, T.G., and Sigler, P.B. (2001). Structural determinants for regulation of phosphodiesterase by a G protein at 2.0 Å. Nature 409, 1071–1077. Sohrabi, C., Foster, A., and Tavassoli, A. (2020). Methods for generating and screening libraries of genetically encoded cyclic peptides in drug discovery. Nat. Rev. Chem. 4, 90–101.

Stallaert, W., van der Westhuizen, E.T., Schönegge, A.M., Plouffe, B., Hogue, M., Lukashova, V., Inoue, A., Ishida, S., Aoki, J., le Gouill, C., et al. (2017). Purinergic receptor transactivation by the β2-adrenergic receptor increases intracellular Ca2+ in nonexcitable cells. Mol. Pharmacol. 91, 533–544.

Sunahara, R.K., Tesmer, J.J., Gilman, A.G. and Sprang, S.R., (1997). Crystal structure of the adenylyl cyclase activator Gsα. Science 278, 1943-1947. Syrovatkina, V., Alegre, K. O., Dey, R., and Huang, X. Y. (2016). Regulation, signaling, and physiological functions of G-proteins. J. Mol. Biol., 428, 3850-3868.

Takasaki, J., Saito, T., Taniguchi, M., Kawasaki, T., Moritani, Y., Hayashi, K., and Kobori, M. (2004). A novel Gαq/11-selective inhibitor. J. Biol. Chem. 279, 47438–47445.

Taylor, V. G., Bommarito, P. A., & Tesmer, J. J. (2016). Structure of the regulator of G protein signaling 8 (RGS8)-Gαq complex: molecular basis for Gα selectivity. J. Biol. Chem., 291, 5138-5145.

Tesmer, J.J.G., Sunahara, R.K., Gilman, A.G., and Sprang, S.R. (1997). Crystal Structure of the Catalytic Domains of Adenylyl Cyclase in a Complex with Gsα GTPγS. Science 278, 1907–1916

Tesmer, V.M., Kawano, T., Shankaranarayanan, A., Kozasa, T. and Tesmer, J.J., (2005). Snapshot of activated G proteins at the membrane: the Gαq-GRK2-Gßγ complex. Science 310, 1686-1690.

Touhara, K.K. and MacKinnon, R., (2018). Molecular basis of signaling specificity between GIRK channels and GPCRs. Elife 7, e42908.

Wall, M.A., Coleman, D.E., Lee, E., IAiguez-Lluhi, J.A., Posner, B.A., Gilman, A.G., and Ft Sprang, S. (1995). The Structure of the G Protein Heterotrimer Giα1β1γ2. Cell 83, 1047-1058

Weis, W.I., and Kobilka, B.K. (2018). The Molecular Basis of G Protein-Coupled Receptor Activation. Annu. Rev. Biochem. 87, 897–919.

Wilson, G.R., Sim, J.C.H., McLean, C., Giannandrea, M., Galea, C.A., Riseley, J.R., Stephenson, S.E.M., Fitzpatrick, E., Haas, S.A., Pope, K., et al. (2014). Mutations in RAB39B cause X-linked intellectual disability and early-onset parkinson disease with α-synuclein pathology. Am. J. Hum. Genet. 95, 729–735.

Winn, M.D., Ballard, C.C., Cowtan, K.D., Dodson, E.J., Emsley, P., Evans, P.R., Keegan, R.M., Krissinel, E.B., Leslie, A.G.W., McCoy, A., et al. (2011). Overview of the CCP4 suite and current developments. Acta Crystallogr. D Biol. Crystallogr. 67, 235–242.

Xiao, H., Murakami, H., Suga, H., and Ferré-D'Amaré, A.R. (2008). Structural basis of specific tRNA aminoacylation by a small in vitro selected ribozyme. Nature 454, 358–361.

Xiong, X.F., Zhang, H., Underwood, C.R., Harpsøe, K., Gardella, T.J., Wöldike, M.F., Mannstadt, M., Gloriam, D.E., Bräuner-Osborne, H., and Strømgaard, K. (2016). Total synthesis and structure-activity relationship studies of a series of selective G protein inhibitors. Nat Chem. 8, 1035–1041.

Yamagishi, Y., Shoji, I., Miyagawa, S., Kawakami, T., Katoh, T., Goto, Y., and Suga, H. (2011). Natural product-like macrocyclic N-methyl-peptide inhibitors against a ubiquitin ligase uncovered from a ribosome-expressed de novo library. Chem Biol. 18, 1562–1570.

Zachary, I., Masters, S.B. and Bourne, H.R., (1990). Increased mitogenic responsiveness of Swiss 3T3 cells expressing constitutively active Gsα. Biochem. Biophys. Res. Commun. 168, 1184-1193.

Zhang, H., Xiong, X.F., Boesgaard, M.W., Underwood, C.R., Bräuner-Osborne, H., and Strømgaard, K. (2017). Structure–Activity Relationship Studies of the Cyclic Depsipeptide Natural Product YM-254890, Targeting the Gq Protein. ChemMedChem 12, 830–834.

Publishing Agreement

It is the policy of the University to encourage open access and broad distribution of all theses, dissertations, and manuscripts. The Graduate Division will facilitate the distribution of UCSF theses, dissertations, and manuscripts to the UCSF Library for open access and distribution. UCSF will make such theses, dissertations, and manuscripts accessible to the public and will take reasonable steps to preserve these works in perpetuity.

I hereby grant the non-exclusive, perpetual right to The Regents of the University of California to reproduce, publicly display, distribute, preserve, and publish copies of my thesis, dissertation, or manuscript in any form or media, now existing or later derived, including access online for teaching, research, and public service purposes.

DocuSigned by:
Shizhong Dai
E802D6498AA64A3...
Author Signature

8/29/2022
Date